NATIONAL & INTERNATIONAL SCIENTIFIC EVENTS

14th International Conference on Molecular Epidemiology and Evolutionary Genetics of Infectious Diseases

Venue: Hotel Melia
Location: Sitges, Spain

Begins: Nov 6, 2018
Ends: Nov 9, 2018

International Conference on Hydraulics and Pneumatics
HERVEX – 24th edition

Venue: Hotel Palace, Baile Govora
Location: Valcea County, Romania

Begins: Nov 7, 2018
Ends: Nov 9, 2018

The 23rd Asian Technology Conference in Mathematics

Venue: Yogyakarta State University (YSU)
Location: Yogyakarta State University, Indonesia

Begins: Nov 20, 2018
Ends: Nov 24, 2018

International Conference on Drug Discovery and Translational Medicine 2018 (ICDDTM '18)

Venue:THE EVERLY HOTEL
Location: Putrajaya, Malaysia

Begins: Dec 3, 2018
Ends: Dec 5, 2018

21st International Conference on Discrete Geometry for Computer Imagery

Venue: ESIEE Paris, Université Paris-Est
Location: Paris, France

Begins: March 25, 2019
Ends: March 29, 2019

6th International Conference on Food Digestion (Granada 2019)

Venue: Granada Exhibition & Conference Centre
Location: Granada, Spain

Begins: April 2, 2019
Ends: April 4, 2019

4th International Congress on 3D Printing (Additive Manufacturing) Technologies and Digital Industry 2019

Venue: Porto Bello Hotel Resort & Spa
Location: Antalya, Turkey

Begins: April 11, 2019
Ends: April 14, 2019

8th International Conference on Nanotechnology & Materials Science

Venue: Hotel Casa Amsterdam
Location: Amsterdam, The Netherlands

Begins: April 24, 2019
Ends: April 26, 2019

17th International Conference on Chemistry and the Environment

Venue: Aristotle University KEDEA Building
Location: Aristotle University KEDEA Building, Thessaloniki, Greece

Begins: June 18, 2019
Ends: June 20, 2019

22nd International Conference on General Relativity and Gravitation

Venue: Valencia Conference Centre
Location: Valencia, Spain

Begins: July 7, 2019
Ends: July 12, 2019

10th International Conference on Nanotechnology: Fundamentals and Applications (ICNFA'19)

Venue: Will be announced.
Location: Lisbon, Portugal

Begins: August 18, 2019
Ends: August 20, 2019

6th Drug Discovery & Therapy World Congress 2019

Venue: Sheraton Boston Hotel, Boston, MA
Location: Boston, USA

Begins: September 3, 2019
Ends: September 5 2019

Abstracted & Indexed in:

TR Dizin Mühendislik ve Temel Bilimler Veri Tabanı | CrossRef | Google Scholar | MIP Database | StuartxChange | ResearchBib | Scientific Indexing Services (SIS)

HITTITE

HJSE Official Journal of Hitit University Volume 5, Issue 3, 2018 www.hjse.hitit.edu.tr

ISSN 2148-4171

HİTİT

JOURNAL OF SCIENCE & ENGINEERING

HITTITE

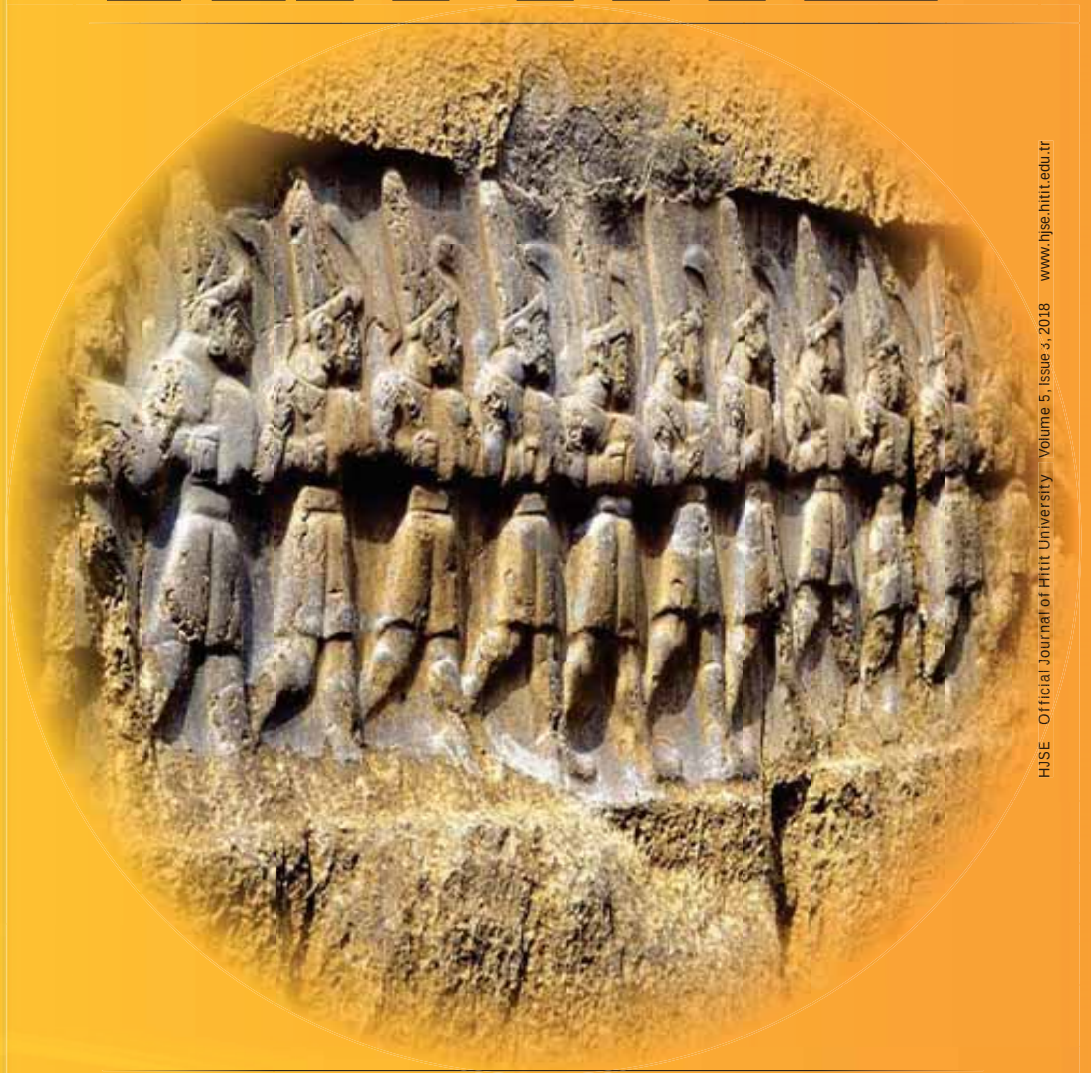

HJSE Official Journal of Hitit University Volume 5, Issue 3, 2018 www.hjse.hitit.edu.tr

Volume 5, Issue 3, 2018

www.hjse.hitit.edu.tr

CONTENT

JOURNAL OF SCIENCE & ENGINEERING
HITTITE

On Determination of the Source Term of a Modified KdV Equation

175-178

Müjdat Kaya

In this study, the existence and uniqueness of the solution of the inverse problem to determine the part of the source term of a modified KdV equation were shown.

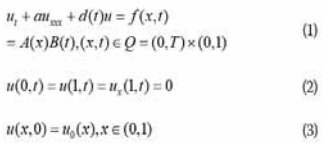

Exact Solutions of (n+1)-Dimensional Space-Time Fractional Zakharov-Kuznetsov Equation

179-183

Muhammad Nasir Ali, Syed Muhammad Husnine, Sana Noor and Adnan Tuna

In this article, the (n+1)-dimensional space time fractional Zakharov-Kuznetsov equation for calculating the exact solutions was studied. For this purpose fractional derivative is used in the form of modified Riemann-Liouville derivatives.

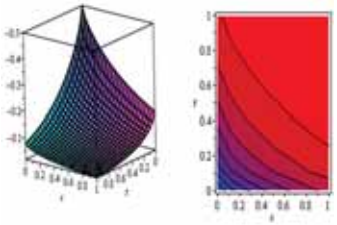

Radon Gas Variations in Soil Gas on Ilgın Active Fault Zone, Konya, Turkey

185-189

Fikret Tüfekçioğlu, Mehmet Erdoğan, Ceren Yağcı and Veysel Zedef

The aim of this study is to investigate a relation between soil gas radon concentration and active fault zone of Ilgın, Konya province, Turkey.

The Unoccupied Surface States of the Cu(110) Substrate

191-194

Orhan Zeybek

The aim of this study is to clarify the unoccupied surface states and to compare available data. It is therefore worthwhile to study electronic states at the Cu(110) clean metal surface.

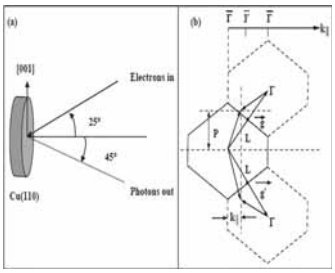

Review: Probing of the Unoccupied Electronic States in Solids by Inverse Photoemission Spectroscopy

195-201

Orhan Zeybek

This paper reviews the probability of probing the unoccupied electronic states in solids by inverse photoemission spectroscopy (IPES). IPES is a surface science technique to analysis the unoccupied electronic states above the Fermi level.

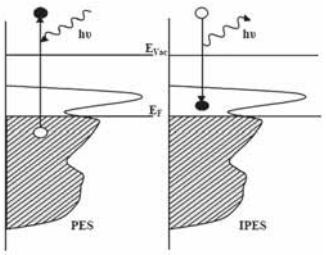

Microstructural and Mechanical Characterization of 9Cr-1Mo-1W Weld Metal

203-208

Emin Salur, Mustafa Acarer, Fikret Kabakci, Selçuk Keskinkilic, Filiz Kumdalı Acar and Bünyamin Cicek

This paper presents microstructural and mechanical characterization of E911 weld metal.

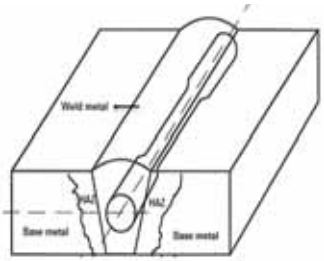

JOURNAL OF SCIENCE & ENGINEERING
HITTITE

CONTENT

The Investigation of Strength and Water Absorption of Self-compacting Concrete by Inclusion of Metakaolin and Calcined Kaolin 209-213

Nihat Atmaca, Adem Atmaca, and Gözde Şafak Sezer

In this study, commercially available high reactivity Czech metakaolin and calcined impure local kaolin were used for production Self Compacting Concrete (SCC) samples and some hardened properties of these concretes have been investigated.

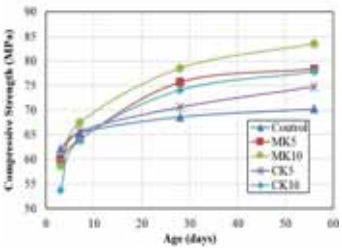

Characterization of Flocs in Dewatering of Coal Plant Tailings 215-218

Can Gungoren, Yasin Baktarhan, Ilgin Kursun, Safak G. Ozkan, and Orhan Ozdemir

In this study, the fine coal tailings were dewatered with an anionic flocculant (SNF-923) at various dosages, and the floc size of the coal tailings was characterized using a laser diffraction particle size analyzer with respect to time.

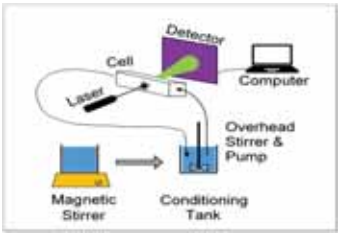

Microstructure, Corrosion and Wear Properties of FeCrNiMo Based Coating Produced on AISI 1040 Steel by Using Laser Coating Technique 219-223

Serkan Islak and Cihan Ozorak

The aim of this study is to investigate microstructure, hardness, corrosion and wear properties of FeCrNiMo-based coating produced on AISI 1040 steel by using laser welding method.

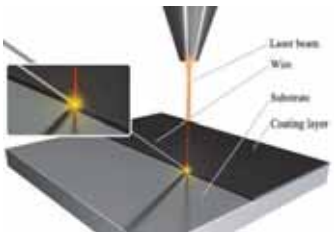

Preparation of Molecular Sentinel Based SERS Sensor for Hepatitis C Virus 225-230

Adem Zengin

In the present study, a novel MS based SERS sensor was designed for detection of HCV DNA. For this purpose, magnetic gold nanoparticles were synthesized and then, functionalized with stem loop structure HCV DNA.

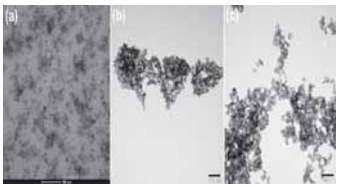

Mechanical Properties of Trip Aided Bainitic Ferrite (TBF) Steels in Production and Service Conditions 231-237

Eren Billur, Semih Karabulut, İmren Öztürk Yılmaz, Samet Erzincanoğlu, Hafize Çelik,

Evren Altınok, and Tanya Başer

This paper deals with a TBF steel's mechanical properties in detail and also discusses the `in-service` properties after work and bake hardening effects.

Drilling of Horizontal Wells in Carbonate Reservoirs of Middle East for Petroleum Production – Investigation of Hydraulics for the Effect of Tool Joints 239-247

Tuna Eren

This study synopsises a brief literature review regarding effects of tool joints during drilling. A diligently planned horizontal well design for Middle East formations is given in this study.

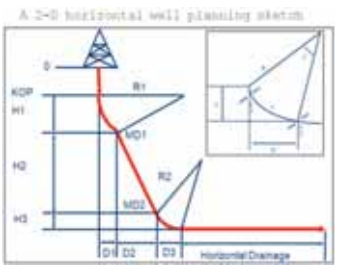

MANAGEMENT

Owner
Prof. Dr. Reha Metin ALKAN on behalf of Hitit University

Editor-in-chief
Prof. Dr. Ali KLIÇARSLAN

Associate Editors
Prof. Dr. D. Ali KÖSE
Assist. Prof. Dr. Öncü AKYILDIZ

Production
Assoc. Prof. Dr. Kazım KÖSE
Dr. Hülya ÇAKMAK
Mustafa Reşit Haboğlu Erhan ÇETİN
Harun Emre KIRAN
Ömer Faruk TOZLU

P**roofreading**
Dr. Hülya ÇAKMAK

Editor's Office
Tel: +90 364 227 45 33 / 12 36
Fax: +90 364 227 45 35
Email: alikilicarslan@hitit.edu.tr

Subscription Service:
Tel: +90 364 227 45 33 / 12 82
Fax: +90 364 227 45 35
Email: hjse@hitit.edu.tr

EDITORIAL BOARD

MASTHEAD

Journal Name	: HITTITE JOURNAL OF SCIENCE AND ENGINEERING
Year	: 2018
Managing Editor	: Prof. Dr. Ali KILIÇARSLAN
Managing Office	: Hitit University Faculty of Engineering
Managing Office Tel	: +90 364 227 45 33 / 12 36
Publication Language	: English
Publication Type	: Peer Reviewed, Open Access, International Journal
Delivery Format Print	: 4 times a year (quarterly)
ISSN Publisher Publisher	: 2149-2123
Address	: Hitit Üniversitesi Kuzey Kampüsü Çevre Yolu Bulvarı 19030 Çorum / TÜRKİYE
Publisher Tel	: +90 364 227 45 33 / 12 36

EDITORIAL

This new issue of Hittite Journal of Science and Engineering contains twelve manuscripts from the disciplines of physics, chemistry, mathematics, civil engineering, mining engineering, materials science and engineering, mechanical engineering and petrolium engineering. These manuscripts was first screened by Section Editors using plagiarism prevention software and then reviewed and corrected according to the reviewer's comments. I would like to express my gratitude to all our authors and contributing reviewers of this issue.

I would like to thank to the President of Hitit University, Dr. Reha Metin Alkan, for his constant interest in HJSE and also to the Associate Editors of HJSE, namely Dr. Dursun Ali Kose and Dr. Oncu Akyildiz, as well as our Production Editors Dr. Kazim Kose, Dr. Hülya Çakmak, Mustafa Reşit Haboğlu, Erhan Çetin, Harun Emre Kıran and Ömer Faruk Tozlu for their invaluable efforts in making of the journal.

It's my pleasure to invite the researchers and scientists from all branches of science and engineering to join us by sending their best papers for publication in Hittite Journal of Science and Engineering.

Dr. Ali Kilicarslan

Editor-in-Chief

Hittite Journal of Science and Engineering, 2018, 5 (3) 175-178
ISSN NUMBER: 2148-4171
DOI: 10.17350/HJSE19030000083

On Determination of the Source Term of a Modified KdV Equation

Müjdat KAYA
Başkent University, Department of Mechanical Engineering, 06790, Ankara, TURKEY

ABSTRACT

We study an inverse problem to identify the source term depending on x of a modified KdV equation. In order to recover source term, we define an inverse problem subject to an overdetermination condition. We converted this inverse problem to an operator equation. The existence and uniqueness of this operator equation is investigated.

Article History:
Received: 2017/06/29
Accepted: 2017/09/25
Online: 2018/03/22

Correspondence to: Müjdat Kaya, Başkent University, Department of Mechanical Engineering, Ankara, TURKEY
E-Mail: mkaya@baskent.edu.tr
Phone: +90 312 246 66 66/1321

Keywords:
Inverse Problem; KdV Equation; Source Term Identification; Overdetermination Condition; Operator Equation

INTRODUCTION

In this article, we investigate the inverse problem associated with the problem

$$u_t + au_{xxx} + d(t)u = f(x,t) = A(x)B(t), (x,t) \in Q = (0,T)\times(0,1) \quad (1)$$

$$u(0,t) = u(1,t) = u_x(1,t) = 0 \quad (2)$$

$$u(x,0) = u_0(x), x \in (0,1) \quad (3)$$

to determine $\{u, A\}$ where a is positive constant, d is continuous function defined in $[0,\infty)$.

The dynamics of small, finite perturbation in an inhomogeneous media are given by equation (1) [3]. Korteweg-de Vries (KdV) equation has great interest and there are many studies on it [1]-[4].

The inverse problem theory for differential equations is being developed to solve problems of mathematical physics. In the study of direct problems, the solution of the equation is derived by means of supplementary conditions.

In the case of inverse problems, the form of the equation is known but the equation is not known exactly. To determine the corresponding equation and its solution, some additional conditions (final overdetermination conditions) must be imposed.

Inverse problems for partial differential equations are extensively investigated. Inverse problems are classified according to the partial differential equations where they arise. The study of Prilepko and Orlovsky [5] is important for the systematic representation for elliptic, hyperbolic and parabolic inverse problems.

We are particularly interested in the inverse problems for determination of the source terms. Such problems have great interest [5, 6 ,7, 8, 9, 10, 11].

In the present study, we show the existence and uniqueness of the solution of the inverse problem to determine the part of the source term of a modified KdV equation. We call the determination of $u(x,t)$ when f is given in (1)-(3) as the direct problem. The determination of $\{u, A\}$, in (1)-(3) with the final overdetermination

$$u(x,t_0) = \alpha(x), t_0 \in (0,T), x \in (0,1) \quad (4)$$

and B is known, is called the inverse problem for recovering the source term A depending on x.

The corresponding direct problem (1)-(3), when $b \equiv 0$, a real constant, is a particular case of the problem, studied by Larkin [1] .

The paper is organized as follows: In section 2, we give some notations, definitions and results about the direct problem. The third section is devoted to derive an equivalent fixed point system for our inverse problem. In the last section, the existence and uniqueness of the fixed point of the system is proved.

PRELIMINARIES

In this section, we summarize the definition and results given in [1]. The usual notations of Sobolev spaces are used for the notations see [12]. For the properties of the solution of the problem (1)-(3), we refer the readers to [1].

Let us denote

$$d_+(t)=\max(0,d(t)),d_-(t)=d_+(t)-d(t)$$

$$(u,v)=\int_0^1 u(x,t)v(x,t)dx,\|u(t)\|^2=(u,u).$$

The following theorem is proved in [1].

Theorem 1. If $a,b,d\in C[0,\infty);a(t)\geq a_0>0,\forall t\geq 0;$ $\sup_{t\geq 0}(|b(t)|+a(t))<\infty,d_-\in L^1(0,\infty),u_0\in L^2(0,1),$ $f\in L^1(0,\infty;L^2(0,1)),u_0\in H^3(0,1)\cap H_0^2(0,1),U_{0x}(1)=0,$ $f\in L^1(0,\infty;L^2(0,1))\cap L^2(0,\infty;H^2(0,1)\cap H_0^1(0,1)),\ f_x(1,t)=0$ for a. e. $t\geq 0$ then (1)-(3) has a unique solution $u=u(x,t)$ such that $u\in C(0,T;H^3(0,1)\cap H_0^1(0,1))\cap L^2(0,T;H^4(0,1)),$ $u_t\in L^\infty(0,T;H_0^1(0,1)),u_x(1,t)=0$ for all finite T.

DERIVATION OF A FIXED POINT SYSTEM

In this section, first we define our solution concept for the inverse problem (1)-(4) and construct an operator equation for the inverse problem. The equivalence of the operator equation and the inverse problem is proved.

Definition 1. We call the pair of functions $(u(x,t),A(x))$ as a solution of the inverse problem (1)-(4), if $u\in C(0,T;H^3(0,1)\cap H_0^1(0,1))\cap L^2(0,T;H^4(0,1)),u_t\in L^\infty(0,T;H_0^1(0,1)),u_x(1,t)=0$ for all finite T and $A\in L^2(0,1)$.

In order to find $A(x)$, first we replace t by t_0 in equation (1) to get

$$u_t(x,t_0)+au_{xxx}(x,t_0)+d(t_0)u(x,t_0)=f(x,t_0)=A(x)B(t_0). \quad (5)$$

If we use equation (4) in (5), it turns to

$$u_t(x,t_0)+a\alpha'''(x)+d(t_0)\alpha(x)=A(x)B(t_0) \quad (6)$$

By solving the equation (6) for $A(x)$, we find

$$A(x)=\frac{u_t(x,t_0)}{B(t_0)}+\frac{a\alpha'''(x)+d(t_0)\alpha(x)}{B(t_0)}. \quad (7)$$

If we define

$$(LA)(x):\frac{u_t(x,t_0)}{B(t_0)},\Phi(x)=\frac{a\alpha'''(x)+d(t_0)\alpha(x)}{B(t_0)}.$$

The relation between A and u may be specified via

$$L:L^2(0,1)\to L^2(0,1)$$

with

$$A(x)=(LA)(x)+\Phi(x). \quad (8)$$

Theorem 2. If the problem (1)-(4) has a solution if and only if the operator equation (8) has a solution.

Proof. Assume that the problem (1)-(4) has a solution. Then, if we follow the steps given above, we derive the operator equation (8).

If the operator equation has a solution $A(x)$, we insert it in the equation (1). Since the problem (1)-(3) has a solution and it is unique by Theorem 1, we have to check whether this $u(x,t)$ satisfies equation (4).

To this end, we assume that

$$u(x,t_0)=\beta(x)$$

then we have

$$u_t(x,t_0)+a\beta'''(x)+d(t_0)\beta(x)=A(x)B(t_0). \quad (9)$$

If we subtract equation (6) from equation (9), we get

$$a(\beta'''-\alpha''')+d(t_0)(\beta-\alpha)=0. \quad (10)$$

By denoting, $\beta-\alpha=y$, $d(t_0)=d$, equation (10) takes the form

$$ay'''+dy=0. \quad (11)$$

The characteristic polynomial $p(r)$ of the differential equation (11) is

$$p(r)=ar^3+d.$$

So, the general solution of the equation (11) is written in the following form

$$y(x)=ke^{(-d/a)^{(1/3)}x}+lxe^{(-d/a)^{(1/3)}x}+mx^2e^{(-d/a)^{(1/3)}x}. \quad (12)$$

Now, we use the conditions given in (3).

When $x=0$, then $y(0)=0$, it gives us that $k=0$. So, $y(x)$ is of the form

$$y(x) = lxe^{(-d/a)^{(1/3)}x} + mx^2e^{(-d/a)^{(1/3)}x}. \quad (13)$$

Since $u(1,t)=0$, then $y(1)=0$. If we use it in equation (13), we get $l=-m$. The new form of the general solution is

$$y(x) = lxe^{(-d/a)^{(1/3)}x} - lx^2e^{(-d/a)^{(1/3)}x}. \quad (14)$$

Taking into account that the value of $u_x(1,t)=0=y'(1)=0$, we can find the value of l as zero. Consequently, the problem (11) has only the solution $y\equiv 0$. It means $y(x)=\beta(x)-\alpha(x)\equiv 0$, hence $\beta(x)=\alpha(x), \forall x$. It proves that $u(x,t_0)$ satisfies (4).

EXISTENCE OF THE SOLUTION OF THE OPERATOR EQUATION

In this section, we study the existence and uniqueness of the fixed point of the derived operator equation (8).

Theorem 3. If

$$B(t)\in C^1(0,T), B(t_0)\neq 0, \frac{(|B'(t)|+e^{\gamma t}-e^{\gamma\xi}+ce^{\gamma\xi})^{1/2}}{B(t_0)}<1,$$

$b(t)\equiv 0, a\in R,$ then (8) has a unique fixed point.

Proof. For the proof, we estimate the norm of L. To this end, first we differentiate (1) with respect to t to find

$$\begin{aligned} &u_{tt}+au_{xxxt}+d'(t)u(x,t)+d(t)u_t(x,t)\\ &=A(x)B'(t) \end{aligned}. \quad (15)$$

If we multiply (15) with u_t and integrate with respect to x from 0 to 1, we get

$$\begin{aligned} &\int_0^1 u_{tt}u_t dx + a\int_0^1 u_{xxxt}u_t dx + d'(t)\int_0^1 uu_t dx\\ &+d(t)\int_0^1 u_t u_t dx = B'(t)\int_0^1 A(x)u_t dx. \end{aligned} \quad (16)$$

First integral in (16) is

$$\int_0^1 u_{tt}u_t dx = \frac{1}{2}\int_0^1 \frac{d}{dt}(u_t)^2 dx = \frac{1}{2}\frac{d}{dt}\|u_t\|^2. \quad (17)$$

If we use integration by parts for the second term in (16);

$$\begin{aligned} &\int_0^1 u_{xxxt}u_t dx = u_{xxt}(1,t)u_t(1,t)\\ &-u_{xxt}(0,t)u_t(0,t)-\int_0^1 u_{xxt}u_{xt}dx. \end{aligned} \quad (18)$$

If we use (3) in (18), it becomes

$$\int_0^1 u_{xxxt}u_t dt = -\int_0^1 u_{xxt}u_{xt}dx. \quad (19)$$

Since $u_{xxt}u_{xt}=\frac{1}{2}\frac{d}{dx}(u_{xt})^2$, then (19) can be written as

$$\int_0^1 u_{xxxt}u_t dt = -\int_0^1 u_{xxt}u_{xt}dx = \frac{1}{2}(u_{xt}(0,t))^2. \quad (20)$$

The third term in (16) is

$$\int_0^1 uu_t dx = \frac{1}{2}\int_0^1 \frac{d}{dt}(u)^2 dx = \frac{1}{2}\frac{d}{dt}\|u\|^2. \quad (21)$$

By the definition of the norm, the forth term of (16) is

$$\int_0^1 u_t u_t dx = \|u_t\|^2. \quad (22)$$

By Cauchy's Inequality, the last term of (16) is estimated to be

$$\int_0^1 A(x)u_t dx \le \frac{\|A\|^2}{2}+\frac{\|u_t\|^2}{2}. \quad (23)$$

With (17), (20), (21), (22) and (23), the equation (16) becomes

$$\begin{aligned} &\frac{1}{2}\frac{d}{dt}\|u_t\|^2+\frac{1}{2}\frac{d'(t)d}{dt}\|u\|^2\\ &+d(t)\|u_t\|^2 \le |B'(t)|\left(\frac{\|A\|^2}{2}+\frac{\|u_t\|^2}{2}\right). \end{aligned} \quad (24)$$

Rearranging (24), it takes the form

$$\frac{d}{dt}\|u_t\|^2+(d(t)-|B'(t)|)\|u_t\|^2 \le |B'(t)|\|A\| \quad (25)$$

Substituting $y := \|u_t\|^2, (d(t) - |B'(t)|) = \gamma$, then (25) becomes

$$y'(t) + \gamma y(t) \le D\|A\|^2, \text{where } D = \max_{t\in[0,T]} |B'(t)|. \quad (26)$$

Solving the inequality (26), we get

$$y(t) \le |B'(t)|\|A\|^2 (e^{\gamma t} - e^{\gamma\xi}) + y(\xi)e^{\gamma\xi}. \quad (27)$$

If we employ proposition 4 in [1], we get the inequality

$$y(t) \le |B'(t)|\|A\|^2 (e^{\gamma t} - e^{\gamma\xi}) + c\|A\|^2 e^{\gamma\xi}. \quad (28)$$

(28) shows that

$$\|u_t(t)\|^2 \le (|B'(t)| + e^{\gamma t} - e^{\gamma\xi} + ce^{\gamma\xi})\|A\|^2. \quad (29)$$

The norm of the operator can be estimated by using (29) as

$$\|LA\| = \left\|\frac{u_t(x,t_0)}{B(t_0)}\right\| \le \frac{(|B'(t)| + e^{\gamma t} - e^{\gamma\xi} + ce^{\gamma\xi})^{1/2}}{B(t_0)}\|A\|. \quad (30)$$

If we impose the condition

$$\frac{(|B'(t)| + e^{\gamma t} - e^{\gamma\xi} + ce^{\gamma\xi})^{1/2}}{B(t_0)} < 1 \quad (31)$$

the operator L is contraction, so it has a unique fixed point [13].

References

1. N. A. Larkin, Modified KdV equation with a source term in a bounded domain,Mathematical Methods In The Applied Science 29 (2006) 751-765.
2. N. A. Larkin, Korteweg-de Vries and Kuramoto-Sivashinsky equation in bounded domains, Journal of Mathematical Analysis and Applications 297 (2004) 169-185.
3. M. Tsutsumi, On global solutions of the modified KdV equation in inhomogeneous media, Funkcialaj Ekvacioj 15 (1972) 161-172.
4. 4. H. Cai, Dispersive smoothing efects for KdV type equations,Journal of Differential Equations 136 (1997) 191-221.
5. A. I. Prilepko, D. G. Orlovsky, I. A. Vasin,Methods for solving inverse problems in mathematical physics, Monographs and Textbooks in Pure and Applied Mathematics, 231, Marcel Dekker Inc., Newyork, 2000, xiv+709 pp.
6. M. Kaya, Determination of the unknown source term in a parabolic problem from the measured data at the final time, Applications of Mathematics 59 (2014) 715-728.
7. M. Kaya, Determination of the unknown Cauchy data in a linear parabolic problem from the measured data at the final time, Mediterranean Journal of Mathematics 10 (2013) 227-239.
8. V. Isakov, Inverse Source Problems, Mathematical Surveys and Monographs, Vol. 34, American Mathematical Society, Providence, RI, 1990.
9. I. B. Bereznits'ka, Inverse problems of determination of the source term in a general parabolic equation, Mat. Stud. 18 (2) (2002) 169-176.
10. O. V. Drozhzhina, The inverse problem for numerical determination of the nonlinear right-hand side in a parabolic equation, Computational Mathematics and Modeling, 14 (4) (2003) 350-359.
11. A. I. Kozhanov, On the solvability of an inverse problem with unknown coefficient and right-hand side for a parabolic equation, Journal of Inverse Ill-Posed Problems, 10(6) (2002), 611-629.
12. S. Kesevan, Topics in Functional Analysis and Applications, John Wiley and Sons, Newyork, Chichester, Brisbane, Toronto, Singapore, 1989.
13. E. Zeidler, Nonlinear Functional Analysis and its Applications, Springer-Verlag, Newyork, Berlin, Heidelberg, Tokyo, 1986.

Hittite Journal of Science and Engineering, 2018, 5 (3) 179-183
ISSN NUMBER: 2148-4171
DOI: 10.17350/HJSE19030000088

Exact Solutions of (n+1)-Dimensional Space-Time Fractional Zakharov-Kuznetsov Equation

Muhammad Nasir Ali[1], Syed Muhammad Husnine[1], Sana Noor[2], Adnan Tuna[3]
[1]Department of Sciences and Humanities, National University of Computer and Emerging Sciences, Lahore, Pakistan.
[2]Department of Geography, Lahore Collage for Women University, Lahore, Pakistan.
[3]Department of Mathematics, Nigde Omer Halisdemir University, 51245, Nigde, Turkey.

ABSTRACT

In this article, we study the (n+1)-dimensional space time fractional Zakharov-Kuznetsov equation for calculating the exact solutions. For this purpose fractional derivative is used in the form of modified Riemann-Liouville derivatives. Complex fractional transformation is applied for transforming the nonlinear partial differential equation into another nonlinear ordinary differential equation. Exact solutions are obtained by using modified simple equation method and (1/G')-expansion method. Obtained solutions are new and may be of significant importance in the field of plasma physics to investigate the waves in the magnetized plasma and in the dust plasma.

Article History:
Received: 2017/07/26
Accepted: 2017/12/10
Online: 2018/04/27

Correspondence to: Department of Sciences and Humanities, National University of Computer and Emerging Sciences, Lahore, Pakistan.
E-mail: taj467@gmail.com,
Phone: (+9242) 111 128 128,
Fax: (+9242)516 5232.

Keywords:
Modified Riemann-Liouville derivatives; Complex fractional transformation; Modified simple equation method; (1/G')-expansion method; Zakharov-Kuznetsov equation.

INTRODUCTION

Nonlinear partial differential equations (NPDEs) are very useful to model many real world problems in science and engineering. Finding the exact solution of such equations is an important area of research. Fractional differential equations (FDE's) are also getting the attention of the researchers in the recent years. Many real world problems are modelled via FDE's in fluid dynamics. Exact solutions of such models play an important role in the mathematical sciences [1-6].

Exact solutions for a variety of FDE's are computed by researchers with different techniques including (G'/G)-expansion method [7], lie group analysis method [8], new extended trial equation method [9], first integral method [5], exp-function method [10], generalized Kudryashov method [2] and many others are suggested for obtaining the exact solutions of FDE's.

In mathematical physics, Zakharov-Kuznetsov (ZK) equation is used to describe the nonlinear development of ion-acoustic waves in magnetized plasma [11]. It is comprised of cold ions and hot isothermal electrons in the presence of a uniform magnetic field. It is also known as the generalizations of the well-known classical KdV equation. In this article, we are interested to calculate the exact solutions of (1+n)-dimensional fractional ZK equation of the following form

$$D_t^{\alpha}u + auD_{(x_1)}^{\alpha}u + D_{(x_1x_1)}^{2\alpha}u + D_{(x_2x_2)}^{2\alpha}u + D_{(x_3x_3)}^{2\alpha}u + \ldots + D_{(x_nx_n)}^{2\alpha} = 0 \quad (1)$$

where $0<\alpha\leq 1$ and a is any arbitrary constant.

The article is arranged as follows. Modified Riemann-Liouville derivative of order α is defined in section 2 together with it properties. In section 3, complex fractional transformation is applied to convert the nonlinear PDE into an ODE and then exact solutions are obtained with MSE method and (1/G')-expansion method. Results are provided in section 4. References are given in the end of the article.

MODIFIED RIEMANN-LIOUVILLE DERIVATIVE AND ITS PROPERTIES

The modified Riemann-Liouville derivative of order α for a continuous function is defined as follows [3].

$$D^{\alpha}_{(x_1)}h(x_1) = \begin{cases} \frac{1}{\Gamma(1-\alpha)}\frac{d}{dx_1}\int_0^{x_1}(x_1-\tau)^{-\alpha}\big(h(\tau)-h(0)\big)d\tau, & 0<\alpha<1 \\ \big(h^n(x_1)\big)^{\alpha-n}, & n\le\alpha<n+1, \quad n\ge 1 \end{cases} \quad (2)$$

where $h: R \to R$, $x_1 = h(x_1)$ denotes a continuous function not necessarily first order differential. Here we have mentioned only following important properties for literature.

If $h: R \to R$, is a continuous function, then its fractional derivative in the form of integral with respect to $(dx_1)^{\alpha}$

$$D^{\alpha}_{(x_1)}h(x_1) = \left\{\frac{1}{\Gamma(\alpha)}\frac{d}{dx_1}\int_0^{x_1}(x_1-\tau)^{\alpha-1}h(\tau)d\tau\right.$$

$$= \frac{1}{\Gamma(1+\alpha)}\frac{d}{dx_1}\int_0^{x_1}h(\tau)(d\tau)^{\alpha}, \quad 0<\alpha<1$$

For any constant k, the fractional derivative is:

$$D^{\alpha}_{(x_1)}(k) = 0$$

For the functions $g(x_1)$ and $h(x_1)$ and the constants a and b, fractional derivative for their linear combination is:

$$D^{\alpha}_{(x_1)}(ag(x_1)+b(h(x_1))) = aD^{\alpha}_{(x_1)}(g(x_1)) + bD^{\alpha}_{(x_1)}(h(x_1))$$

For $h(x_1)=(x_1)^p$ the fractional derivative will be

$$D^{\alpha}_{(x_1)}((x_1)^p) = \frac{\Gamma(1+p)}{\Gamma(1+p-\alpha)}(x_1)^{(p-\alpha)}$$

EXACT SOLUTIONS

To find the exact solution of Eq. (1), we transform the FZK equation in to another nonlinear ODE by applying the following complex fractional transformation

$$\xi = \frac{(x_1)^{\alpha}}{\Gamma(1+\alpha)} + \frac{(x_2)^{\alpha}}{\Gamma(1+\alpha)} + \frac{(x_3)^{\alpha}}{\Gamma(1+\alpha)} + \ldots + \frac{(x_n)^{\alpha}}{\Gamma(1+\alpha)} - \frac{w(t)^{\alpha}}{\Gamma(1+\alpha)} \quad (3)$$

This results in the following ODE

$$-wU' + aUU' + nU'' = 0, \quad (4)$$

where $U = u(\xi)$ and $U' = \frac{du}{d\xi}$. Integrating Eq. (4) with respect to ξ taking constant of integration zero, it results

$$-wU + 1/2aU^2 + nU' = 0. \quad (5)$$

Exact Solutions With Modified Simple Equation Method

Here we utilized the MSE method [4] to find the exact solutions. Applying the equation balance method to achieve the value *m=1*. Therefore the solution will take the form as

$$U(\xi) = k_0 + k_1\left(\frac{\varphi'}{\varphi}\right), \quad (6)$$

where k_0, k_1 are the constant to be determined such that $k_1 \neq 0$. Now we are in need to find the values of U^2 and U' from Eq. (6). i.e

$$\left.\begin{aligned} U' &= k_1\left(\frac{\varphi''}{\varphi} - \left(\frac{\varphi'}{\varphi}\right)^2\right) \\ U^2 &= k_0^2 + 2k_0k_1\left(\frac{\varphi'}{\varphi}\right) + k_1^2\left(\frac{\varphi'}{\varphi}\right)^2 \end{aligned}\right\} \quad (7)$$

Putting the above values in Eq. (5) and compare the different powers of φ equal to zero, we have the following system of equations

$$-wk_0 + \frac{1}{2}ak_0^2 = 0, \quad (8)$$

$$nk_1\varphi'' + k_1(ak_0 - w)\varphi' = 0, \quad (9)$$

$$\left(\frac{1}{2}ak_1^2 - nk_1\right)\varphi'^2 = 0. \quad (10)$$

Using Eq. (8), it gives two values of the constant k_0 as below:

$$k_0 = 0, \quad \frac{2w}{a}. \quad (11)$$

As $k_1 \neq 0$, so Eq. (10) yields the following value of k_1:

$$k_1 = \frac{2n}{a}. \quad (12)$$

Now we have to find the value of φ. For this we have the following two cases.

Case 1: When $k_0 = 0$, Eq. (9) gives the following result

$$(n\varphi'' - w\varphi')k_1 = 0,$$
$$\frac{\varphi''}{\varphi'} = \frac{w}{n}. \quad (13)$$

Integrating w.r.t. ξ , we have

$$\ln(\varphi') + \ln(c) = \frac{w}{n}\xi, \qquad \varphi' = c_1 e^{\frac{w}{n}\xi}. \tag{14}$$

where c_1 is the constant of integration. Integrating again in Eq. (14), it results,

$$\varphi = \frac{nc_1}{w} e^{\frac{w}{n}\xi} + c_2, \tag{15}$$

where c_1 and c_2 are constants of integration $c_1 = \frac{1}{c}$. Hence the exact solution given in Eq. (6) will takes the form as

$$U(\xi) = k_0 + k_1 \left(\frac{c_1 e^{\frac{w}{n}\xi}}{\frac{nc_1}{w} e^{\frac{w}{n}\xi} + c_2} \right), \tag{16}$$

After substituting the values of k_0, k_1 in Eq. (16) and simplifying, we obtain

$$U_1(\xi) = \frac{2nw}{a} \left(\frac{c_1 \left(\cosh\left(\frac{w}{2n}\xi\right) + \sinh\left(\frac{w}{2n}\xi\right) \right)}{(nc_1 + wc_2)\cosh\left(\frac{w}{2n}\xi\right) + (nc_1 - wc_2)\sinh\left(\frac{w}{2n}\xi\right)} \right). \tag{17}$$

Case 1 (a): If we put $c_1 = \frac{wc_2}{n}$, solution given in Eq. (17) will take the form as

$$U_2(\xi) = \frac{w}{a}\left(1 + \tanh\left(\frac{w}{2n}\xi\right)\right). \tag{18}$$

Case 1 (b): Similarly, when $c_1 = -\frac{wc_2}{n}$, solution will take the form as

$$U_3(\xi) = \frac{w}{a}\left(1 + \coth\left(\frac{w}{2n}\xi\right)\right). \tag{19}$$

Case 2: When $k_0 = \frac{2w}{a}$, Eq. (6) yields

$$U(\xi) = k_0 + k_1 \left(\frac{c_1 e^{-\frac{w}{n}\xi}}{\frac{nc_1}{w} e^{-\frac{w}{n}\xi} + c_2} \right), \tag{20}$$

Substituting the values of k_0, k_1 in Eq. (20) and simplifying, we have

$$U_4(\xi) = \frac{2w}{a} + \frac{2nw}{a} \left(\frac{c_1 \left(\cosh\left(\frac{w}{2n}\xi\right) - \sinh\left(\frac{w}{2n}\xi\right) \right)}{(nc_1 + wc_2)\cosh\left(\frac{w}{2n}\xi\right) + (-nc_1 + wc_2)\sinh\left(\frac{w}{2n}\xi\right)} \right) \tag{21}$$

Case 2 (a): If we put $c_1 = \frac{wc_2}{n}$, Eq. (21) will take the following form

$$U_5(\xi) = \frac{2w}{a} + \frac{w}{a}\left(1 - \tanh\left(\frac{w}{2n}\xi\right)\right). \tag{22}$$

Case 2 (b): Similarly, if we put $c_1 = -\frac{wc_2}{n}$, Eq. (21) will be

$$U_6(\xi) = \frac{2w}{a}\frac{w}{a}\left(\coth\left(\frac{w}{2n}\xi\right) - 1\right), \tag{23}$$

where ξ is given in Eq. (3).

Exact Solution With (1/G')-Expansion Method

Here we use the (1/G')-expansion method [12] for calculating the exact solutions. Balancing the terms U' and U^2 in Eq. (3.3), it yields M=1. Hence the solution will take the form as

$$U = a_0 + a_1\left(\frac{1}{G'}\right), \tag{24}$$

where $G(\xi)$ satisfy the ordinary linear differential equation

$$G''(\xi) + \lambda G'(\xi) + \mu = 0, \tag{25}$$

with a_0, a_1, λ and μ as constants to be determined. This equation contains the solution

$$G(\xi) = c_1 e^{-\lambda\xi} - \frac{\mu}{\lambda}\xi + c_2, \tag{26}$$

where ξ is defined in Eq. (3) and

$$\left(\frac{1}{G'}\right) = \frac{\lambda}{-\mu + \lambda c_1\left(\cosh(\lambda\xi) - \sinh(\lambda\xi)\right)}, \tag{27}$$

Using Eq. (24) in Eq. (5) and then comparing coefficients of different powers of $\frac{1}{G'}$, we obtain system of equations

$$\left(\frac{1}{G'}\right)^0: \quad -wa_0+\frac{a}{2}a_0^2=0 \quad ,$$

$$\left(\frac{1}{G'}\right)^1: \quad -wa_1+aa_0a_1+na_1\lambda=0 \quad , \tag{28}$$

$$\left(\frac{1}{G'}\right)^2: \quad \frac{1}{2}aa_1^2+\mu na_1=0 \quad .$$

Solving the system (3.26), we arrive at the following solutions:

Set 1: $\lambda=\frac{w}{n}, \quad a_1=-\frac{2n\mu}{a}, \quad a_0=0.$ (29)

Putting values from Eq. (27) and Eq. (29) in Eq. (24), we have

$$U_7(\xi)=\frac{-2nw\mu}{a\left(wc_1-n\mu\right)\left(\cosh\left(\frac{w}{n}\xi\right)-\sinh\left(\frac{w}{n}\xi\right)\right)}. \tag{30}$$

Set 2: $\lambda=-\frac{w}{n}, \quad a_1=-\frac{2n\mu}{a}, \quad a_0=0.$ (31)

substituting values from Eq. (27) and Eq. (31) in Eq. (24), it yields

$$U_8(\xi)=\frac{2w}{a}-\frac{2nw\mu}{a\left(wc_1+n\mu\right)\left(\cosh\left(\frac{w}{n}\xi\right)+\sinh\left(\frac{w}{n}\xi\right)\right)} \tag{32}$$

where ξ is given in Eq. (3).

CONCLUSION

In this article, we achieved some exact solutions of (1+n)-dimensional fractional Zakharov-Kuznetsov equation. We apply the complex fractional wave transformation which converts the original nonlinear PDE into another nonlinear ODE. Then, (1/G')-expansion and modified simple equation methods are used to find the exact solutions. Obtained solutions are new and of significant importance to study the waves in the magnetized and dust plasmas. For different values of the parameters, graphical representations of the solutions are provided below with the help of computer software Maple 13. We have considered the case for n=1 for graphical representation (i.e. $u(x,t)$). In Fig. 1, for $w=-1.5$, $\alpha=0.7$, $a=3$, plots for the solution U_2 plots for the solution U_2 and its contour plot are given. In Fig.2, For $w=2$, $\alpha=0.7$, $a=-3$, plots for the solution U_3 and its contour plot are provided. In Fig.3, For $w=1.75$, $\alpha=0.3$, $a=0.4$, $c_1=5$, $\mu=5$, plots for the solution U_8 and its contour plot are presented. We have presented few of the solutions in graphical format. One can easily obtain the plots of others solutions easily.

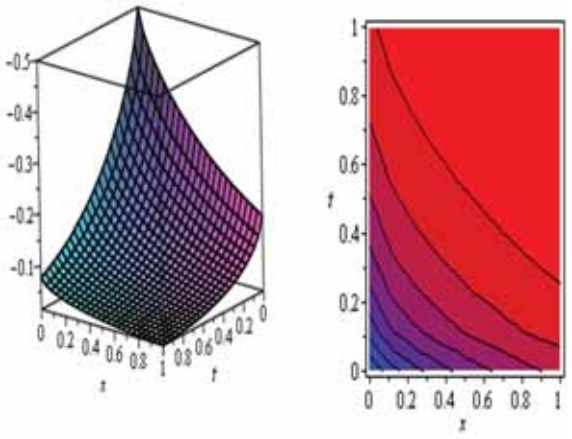

Figure 1. U_2 and its contour plot

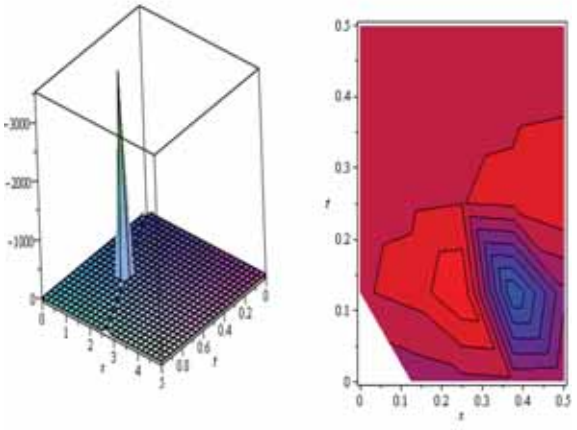

Figure 2. U_2 and its contour plot

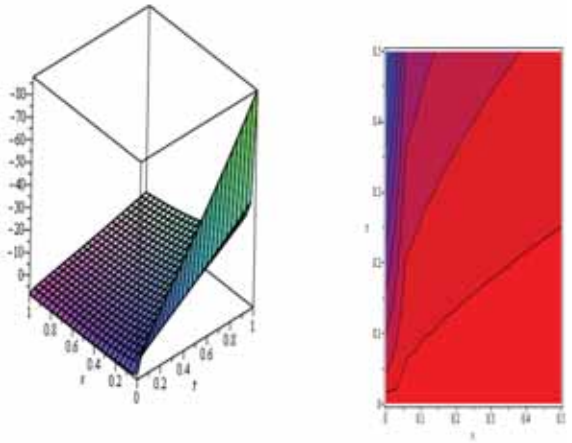

Figure 3. U_3 and its contour plot

References

1. Gepreel KA, Omran S. Exact solutions of nonlinear fractional partial differential equation. Chinese Physics B 21(11) (2017) 110204.
2. Guner O, Aksoy E, Bekir A, Cevikel AC. Different methods for (3+1)−dimensional space−time fractional modified KdV−Zakharov−Kuznetsov equation. Computers & Mathematics with Applications 71(6) (2016) 1259−1269.
3. Jumarie G. Table of some basic fractional calculus formulae derived from a modified Riemann−Liouville derivative for non−differentiable functions. Applied Mathematics Letters 22(3) (2009) 378−385.
4. Khan K, Akbar MA. Exact solutions of the (2+1)−dimensional cubic Klein-Gordon equation and the (3+1)−dimensional Zakharov−Kuznetsov equation using the modified simple equation method. Journal of Association of Arab Universities for Basic and Applied Sciences 15 (2014) 74-81.
5. Lu B. The first integral method for some time fractional differential equation. Journal of Mathematical Analysis and Applications 395(2) (2012) 684−693.
6. Miller KS, Ross B. An Introduction to Fractional Calculus and Fractional Differential Equations, John Wiley, New York, 1993.
7. Bekir A, Guner O. Exact solutions of nonlinear fractional differential equations by (G^'/G)−expansion method. Chinese Physics B 22(11) (2013) 110202.
8. Chen C, Jiang Y−L. Lie group analysis for two classes of fractional differential equations. Communications in Nonlinear Science and Numerical Simulation 26(1−3) (2015) 24−35.
9. Pandir Y, Gurefe Y. New exact solutions of the generalized fractional Zakharov−Kuznetsov equations. Life Science Journal 10(2) (2013) 2701−2705.
10. Zheng B. Exp−function method for solving fractional partial differential equations. The Scientific World Journal 2013 (2013) 465723.
11. Zakharov VE, Kuznetsov EA. On three−dimensional solitons. Soviet Physics 39 (1974) 285−288.
12. Daghan D, Donmez O. Exact solutions of Gardner equation and their application to the different physical plasma. Brazilian Journal of Physics 46(3) (2016) 321−333.

Hittite Journal of Science and Engineering, 2018, 5 (3) 185-189
ISSN NUMBER: 2148-4171
DOI: 10.17350/HJSE19030000092

Radon Gas Variations in Soil Gas on Ilgın Active Fault Zone, Konya, Turkey

Veysel ZEDEF[1], Fikret TÜFEKÇİOĞLU[2], Mehmet ERDOĞAN[3], Ceren YAĞCI[4]
[1]Selcuk University, Department of Mining Engineering, Campus, 42003, Konya, TURKEY
[2]Selcuk University, Institute of Natural Sciences, Campus, 42003, Konya, TURKEY
[3]Selcuk University, Department of Physics, Campus, 42003, Konya, TURKEY
[4]Selcuk University, Department of Geomatics, Campus, 42003, Konya, TURKEY

ABSTRACT

Soil gas radon concentrations have been studied in an active fault zone of Ilgın, Konya, Turkey. At this seismically active fault zone (20 km long, 3-5 km width in the study area) there are two faults and a graben in between them. The maximum radon and thoron concentrations are 32601(Bq/m^3) and 17628 (Bq/m^3), while the minimum values are 170 (Bq/m^3) and 103 (Bq/m^3) respectively. At 15 sampling points for radon the obtained values are higher than the average values. There has been a clear visibility of both ^{222}Rn (radon) and ^{220}Rn (thoron) anomalies in the area. The ^{222}Rn and ^{220}Rn have no positive or negative correlation at sampling points in the field.

Article History:
Received: 2017/09/15
Accepted: 2017/11/12
Online: 2018/05/29

Correspondence to: Veysel Zedef, Selcuk University, Department of Mining Engineering, Campus, 42003, Konya, TURKEY
E-Mail: vzedef@selcuk.edu.tr
Phone: +90 332 223 20 46
Fax: +90 332 241 06 35

Keywords:
Radon gas; Geological conditions; Active fault zone; Ilgın; Turkey

INTRODUCTION

A strong relation between soil gas radon concentration and underlying geological features has been known for many years. The content of radon in soil, beside atmospheric conditions such as temperature, moisture and pressure [1], is more strongly controlled by porosity-permeability, fractures, nature of rocks, active-inactive faults, magmatic and volcanic activity of a region. In addition to these, many other factors such as soil type and sediment thickness [2], soil particle size [3] and radium bearing mineral content of formations [4]. To minimize the effect of atmospheric conditions, the soil gas radon measurements have been undertaken at depths of a meter or more.

The radon level in soil gas can easily be increased by a fault since a fault could be a pathway for radon emanated from deep formations [5, 6, 7, 8, 9, 10, 11, 12, 13, 14, 15]. A similar relation between radon content of well-spring water and faulty zones was pointed out [16, 17]. However, the anomalies is not restricted for only radon gas, but HCO_3^{-1} [18], helium [19], hydrogen [20] and carbon dioxide [21] anomalies were also noted on fault zones.

The aim of this paper is to investigate a relation (if any) between soil gas radon concentration and active fault zone of Ilgın, Konya province, Turkey.

GEOLOGICAL AND SEISMOLOGICAL SETTING

The study area is geographically located on SW of Central Turkey (Fig. 1). Turkey is geologically divided into four tectonic units by Ketin [22]. These are Taurids in the south, Anatolids in the center, Pontids in the north and Border Folds in the southeast. The investigation area is found within the Anatolids which subsequently divided into several units by Ozgul [23]. The Ilgın area is a part of Bolkardagı units of Ozgul [23]'s division. On the other hand, the area is included in Kutahya-Bolkardagı Belt by Ozcan et al. [24]. Çavuşcu Göl (Göl means lake) is located at the central part of the south of study area (see Fig. 1). The lake is formed on a graben where two normal faults are roughly found at west (Ilgın fault) and east (Tekeler fault). The two horsts are occurred at both side of this graben, the Karakaya Tepe horst in the west and the Gavurdagı horst in the east. The area is not focused for only these active faults, grabens and horsts but it is also important for economical lignite seams [25, 26, 27].

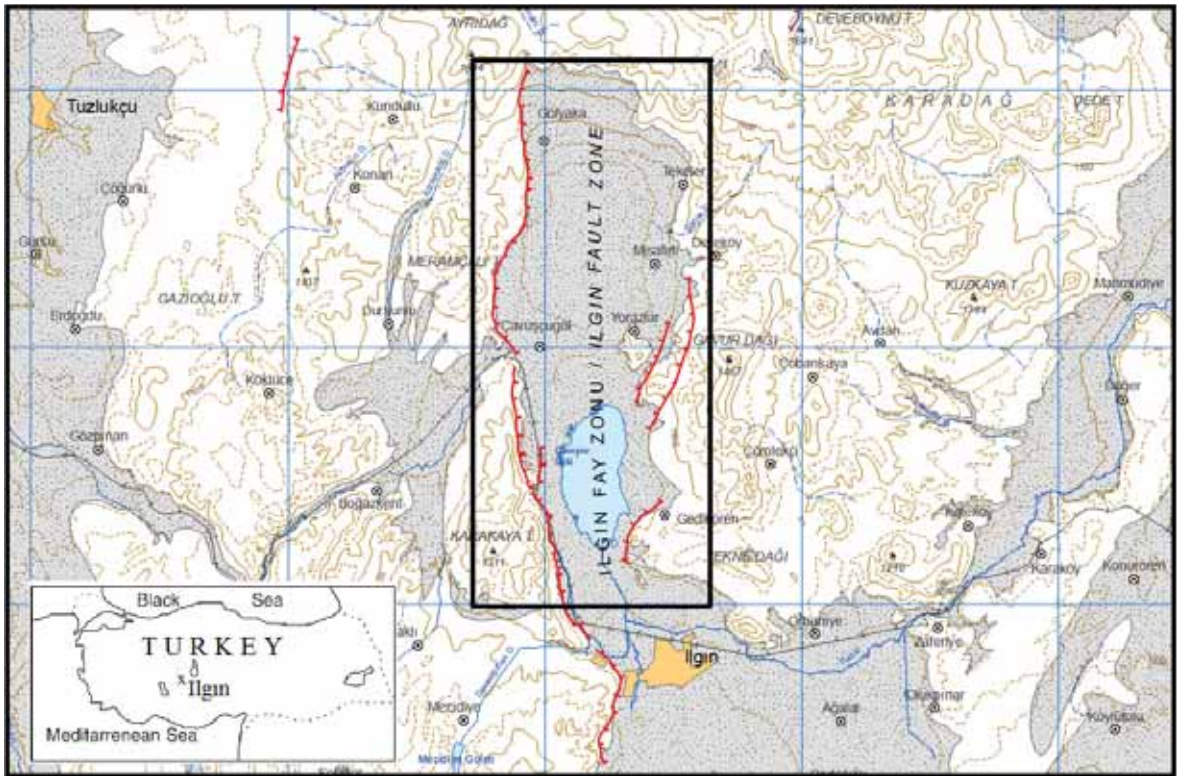

Figure 1. Location map of study area, the map for active fault is from MTA (Mineral Research and Exploration of Turkey) web-page.

Perhaps (or to our knowledge), the most detailed geological (including structural and stratigraphic) study in the area was undertaken by Huseyinca and Eren [28]. According to these authors, the oldest units in the area is Silurian-Early Carboniferous aged marbles of limestone and dolostone which are unconformably overlain by Mesozoic aged metamorphites. Huseyinca and Eren [28] stated that the Tertiary aged lignite seams with claystone, mudstone and siltstone are found over these metamorphic basements. All the rocks forming basement are strongly effected by Cimmerian and subsequent Alpine orogenesis which gave rise many faulting, fracturing and folding [28]. The recent tectonic movements (usually called as Neo-tectonic movements) were responsible for developments of today's active faults, horsts and grabens in the region. A sketch of general geological cross section of the area is performed in Fig. 2.

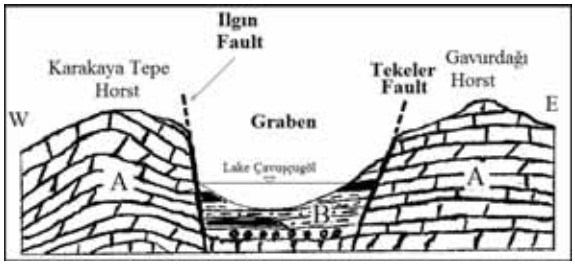

Figure 2. A sketch of geological cross section from west to east in the study area (no to scale). Note: A represents metamorphic basement of generally Paleozoic and Mesozoic aged rock units; B represents younger sediments of Cenozoic, mostly Pleistocene and Holocene aged detrital rocks with lignite seams (black painted).

From the neo-tectonic point of view, the area is tectonically situated between Gavurdağı and Karakaya Tepe horsts. The graben is found in between these horsts (Fig. 2). The graben can be traced almost 20 km from south to north while its width is about 3-5 km at east-west direction. The seismically active Ilgın fault is found at the west side of this graben, and the Tekeler fault restricted the eastern side. Seismologically, these two faults are presently producing earthquakes. An officially published recent earthquake data is present on Table 1. The most devastating earthquake (Magnitude 5.5) in the area was taken place in February, 21,

Table 1. The latest earthquakes in the study area, Ilgın, Konya.

Date	*Time*	*M*
20:29:52	*70.25*	*72.25*
22:44:32	*69.00*	*66.25*
00:36:16	*69.25*	*68.50*
23:03:12	*77.25*	*68.00*
20:29:52	*70.25*	*72.25*
22:44:32	*69.00*	*66.25*
00:36:16	*69.25*	*68.50*
23:03:12	*77.25*	*68.00*
20:29:52	*70.25*	*72.25*
22:44:32	*69.00*	*66.25*
00:36:16	*69.25*	*68.50*
23:03:12	*77.25*	*68.00*

1946. At this earthquake, 55 people were died and 3349 injured. A recent, relatively strong (Magnitude 5) earthquake has taken place in July, 27, 2011. No casualty reported (Note that all the data about the earthquakes taken from the Kandilli Rasathanesi web-page).

In the area, the trace of Ilgın fault can easily be observed while the Tekeler fault script is mostly buried by the Quaternary sediments, mostly exposed over Paleozoic and Mesozoic aged metamorphic rock units in the eastern part of the graben between the towns of Ilgın and Çavuşcugöl. As a seismically active area, the towns of Ilgın, Çavuşcugöl, Gölyaka, Yorazlar, Misafirli, Tekeler and Dereköy often hit (average three times each monts) by earthquake with magnitude > 2. The focuses of the quakes are mostly 4 to 15 km depth (www.depremler.org/konya-depremleri-1)

FIELD SURVEY AND METHODOLOGY

A total of 32 sampling location were chosen and settled in the Pleistocene-Holocene aged strata in the light of earlier geological surveys. The sampling locations were homogenously scattered to represent all graben and faulty area (except the lake itself). The survey for soil gas was performed in a period with stable meteorological condition from August to September. The used radon monitor in this study is made up three main parts: (1) Alphaquard PQ2000 Pro brand radon monitor, (2) Soil gas probe and (3) Pump. For measurement, a hole 1 m deep was drilled and available soil gas was pumped out into the ionization chamber of the monitor. Then, both radon isotopes of ^{222}Rn and ^{220}Rn were measured. For ^{222}Rn reading, the ionization chamber has to be kept closed for about 10 minutes to allow ^{220}Rn (thoron) to decay. The total staying time of drilled pipe into the soil is 30 to 40 minutes. To do this, the soil gas can diffuse out the pipe. The obtained measurements in this study represent 30-40 minutes degassing of soil gas for each sampling point.

RESULTS AND DISCUSSION

All the results for ^{222}Rn (radon) and ^{220}Rn (sometimes called as thoron) are shown in Table 2. During the measurement time temperature, air pressure and humidity

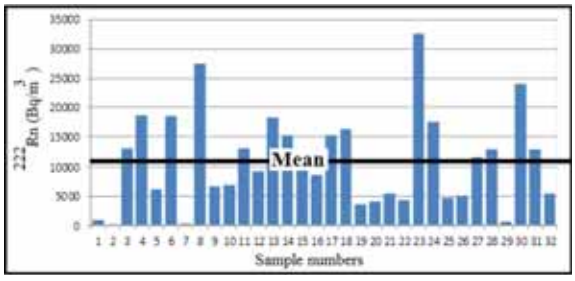

Figure 3. The distribution of ^{222}Rn (radon) in soil gas in the study area.

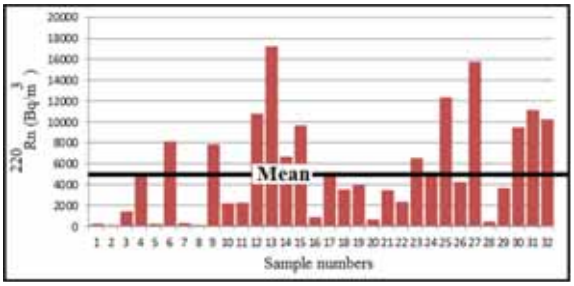

Figure 4. The distribution of ^{220}Rn (radon) in soil gas in the study area.

of the atmosphere is also measured. The altitude and coordinates of each sampling locations were also included in Table 1. The average ^{222}Rn and ^{220}Rn concentrations of the samples are 10930 (Bq/m^3) and 5338 (Bq/m^3) respectively. The maximum radon and thoron concentrations are 32601(Bq/m^3) and 17628 (Bq/m^3), while the minimum values are 170 (Bq/m^3) and 103 (Bq/m^3) respectively. At 15 sampling points for radon the obtained values are higher than the average values (Fig. 3). On the other hand, 12 sampling locations exceed average thoron concentrations (Fig. 4). All these indicate there has been a radon and thoron anomalies in the area of active Ilgın fault zone and related graben area. One point has to be pointed out that there has been no positive correlation between radon and thoron concentrations on the investigation area (Fig. 5). The radon and thoron values are seems to be no any relation with temperature, air pressure and humidity of the atmosphere. No positive and negative correlation has been observed between radon-thoron concentrations and altitude of measurement points. Unlike most other works seen on the literature at hand, we could not see any radon-thoron anomalies just over faults.

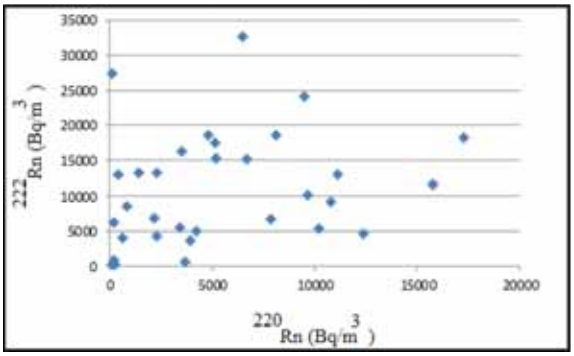

Figure 5. A claster of ^{222}Rn (radon) v ^{220}Rn (thoron) indicating the absence of positive or negative correlation in soil gas in the study area.

CONCLUSION

The Ilgın fault zone is a seismically active area and the recent seismicity gave rise tectonically occurring graben and horst formation in the study area. The measured ^{222}Rn (radon) and ^{220}Rn (thoron) concentrations indicate that there has been a visible anomalies on fault zones. A similar judgment cannot be undertaken for individual

Table 2. Results of a soil gas ^{222}Rn and ^{220}Rn concentration (Bq/m^3) measurement around Ilgın Fault Zone (Temperature, air pressure, humidity, altitude and coordinates of each mesurement are included).

Sampling No	*^{222}Rn(Bq/m^3)*	*^{220}Rn(Bq/m^3)*	*Temperature(°C)*	*Air Pressure (mbar)*	*Humidity (%)*	*Altitude(m)*	*Coordinate*
1	*865*	*224*	*27,3*	*901.1*	*15,7*	*1059*	*38018'05"N 31051'52"E*
2	*170*	*122*	*24,5*	*899,5*	*16,7*	*1037*	*38018'12"N 31052'23"E*
3	*13169*	*1436*	*23,7*	*899,8*	*18,3*	*1036*	*38018'32"N 31054'28"E*
4	*18647*	*4828*	*20,2*	*899,7*	*22,3*	*1030*	*38018'25"N 31053'50"E*
5	*6185*	*196*	*13,8*	*899,2*	*26,3*	*1034*	*38019'06"N 31053'28"E*
6	*18539*	*8136*	*14,8*	*899,1*	*34,7*	*1042*	*38019'13"N 31053'59"E*
7	*258*	*264*	*17,8*	*902*	*46*	*1053*	*38018'38"N 31051'50"E*
8	*27420*	*103*	*19,4*	*900.6*	*39,4*	*1040*	*38018'41"N 31052'02"E*
9	*6686*	*7858*	*19,5*	*900,8*	*37,8*	*1053*	*38020'26"N 31050'59"E*
10	*6868*	*2191*	*22,2*	*900,4*	*39,3*	*1035*	*38020'30"N 31051'12"E*
11	*13193*	*2282*	*21,6*	*900.3*	*38,1*	*1058*	*38020'52"N 31054'09"E*
12	*9163*	*10773*	*19,3*	*900,1*	*36,2*	*1042*	*38020'52"N 31053'49"E*
13	*18238*	*17268*	*15,8*	*900,7*	*41,5*	*1060*	*38023'02"N 31053'58"E*
14	*15211*	*6690*	*14*	*900,7*	*59,6*	*1031*	*38023'00"N 31053'40"E*
15	*10133*	*9681*	*12,7*	*900,9*	*52,5*	*1030*	*38022'20"N 31051'00"E*
16	*8556*	*826*	*16,4*	*899,5*	*38*	*1047*	*38022'18"N 31050'42"E*
17	*15277*	*5182*	*15,5*	*898,2*	*39,3*	*1045*	*38023'05"N 31050'36"E*
18	*16277*	*3505*	*15,4*	*896,4*	*42,7*	*1023*	*38023'07"N 31050'55"E*
19	*3595*	*3931*	*15,7*	*898.4*	*39,6*	*1014*	*38026'21"N 31054'17"E*
20	*4052*	*623*	*16,8*	*898,7*	*37,2*	*1030*	*38026'09"N 31054'35"E*
21	*5470*	*3423*	*13,5*	*900,3*	*50,2*	*1042*	*38026'57"N 31054'55"E*
22	*4281*	*2311*	*15,1*	*899,8*	*44,5*	*1030*	*38026'52"N 31054'38"E*
23	*32631*	*6499*	*17,1*	*899,2*	*40,2*	*1024*	*38023'45"N 31050'31"E*
24	*17542*	*5165*	*13,8*	*897,9*	*42,3*	*1027*	*38023'43"N 31050'12"E*
25	*4647*	*12364*	*8,2*	*897,4*	*54,6*	*1038*	*38025'22"N 31054'20"E*
26	*4993*	*4245*	*14,8*	*899,7*	*40,4*	*1028*	*38023'42"N 31050'52"E*
27	*11611*	*15781*	*19,5*	*893.9*	*29,9*	*1041*	*38023'14"N 31049'50"E*
28	*12968*	*407*	*21,4*	*888.7*	*32,3*	*1058*	*38020'22"N 31047'01"E*
29	*587*	*3669*	*21,0*	*890,9*	*34,7*	*1089*	*38018'03"N 31048'21"E*
30	*24073*	*9501*	*20,4*	*888.6*	*33,9*	*1166*	*38027'11"N 31055'29"E*
31	*12975*	*11127*	*20,4*	*891.5*	*37,5*	*1067*	*38024'06"N 31055'08"E*
32	*5411*	*10211*	*16,3*	*895,8*	*34,6*	*1155*	*38019'45"N 31055'58"E*

fault scraps themselves in the field. There is no positive or negative correlation between ^{222}Rn and ^{220}Rn for same measurement points in the field.

ACKNOWLEDGEMENT

This study is financially supported by Selcuk University Council of Scientific Research Project (BAP-project number:12201003, part of Fikret Tufekcioglu's PhD thesis). The author thanks to the unanimous referees of the journal for the constructive corrections and interpretations.

References

1. Winkler, R., Ruckerbauer, F. and Bunzi, K., 2001, Radon concentration in soil gas: a comparison of the variability resulting from different methods, spatial heterogeneity and seasonal fluctuations: Science of the Total Environment, 272, 273-282.
2. Lehmann, B. E., Lehmann, M., Neftel, A. and Tarkanov, S. V., 2000, Radon-222 monitoring of soil diffusivity: Geophysical Research Letters, 27 (23), 3917-3920.
3. Choubey, V. M., Bist, K. S., Saini, N. K. and Ramola, R. C., 1999, Relation between soil gas radon variation and different lithotectonic units, Garhwaal Himalaya, India: Applied Radiation and Isotopes, 51, 587-592.
4. Papp, B., Deak, F., Horwath, A., Kiss, A., Rajnai, G. and Szabo, C., 2008, A new method for the determination of geophysical parameters by radon concentration measurements in bore-hole: Journal of Environmental Radioactivity, 99, 1731-1735.
5. Wang, X., Li, Y., Du, J. and Zhou, X., 2014, Correlations between radon in soil gas and the activity of seismogenic faults in the Thangshan area, North China: Radiation Measurements, 60, 8-14.
6. Warky, N. R. and Flowers, A. G., 1992, Radon and its correlation with some geological features of the south-west of England: Radiation Protection Dosimetry, 45, 245-248.
7. Israel, H. and Bjornsson, S., 1967, Radon and thoron in soil air over faults: Geophysics, 33, 48-64.
8. Koray, A., Akkaya, G., Kahraman, A.and Kaynak, G., 2013, Measurements of radon concentrations in waters and soil gas of Zonguldak, Turkey: Radiation Protection Dosimetry, 1-7.
9. Swakon, J., Kozak, K., Paszkowski, M., Gradzinski, R., Loskiewicz, J., Mazur, J., Janik, M., Bogacz, J., Horwacik, T. and Olko, P., 2005, Radon concentration in soil gas around local disjunctive tectonic zones in the Krakow area: Journal of Environmental Radioactivity, 78, 137-149.
10. Kemski, J., Klingel, R., Schneiders, H., Siehl, A. and Wiegand, J., 1992, Geological structure and geochemistry controlling radon in soil gas: Radiation Protection Dosimetry, 45, 235-239.
11. Etiope, G. and Lombardi, S., 1995, Evidence for radon transport by carrier gas through faulted clays in Italy: Journal of Radioanalytical and Nuclear Chemistry, 193, 291-300.
12. Al-Batania, B. A., Al-Taj, M. M. and Atallah, M. Y., 2005, Relations between radon concentrations and morphotectonics of the Dead Sea transform in Wadi Araba, Jordan: Radiation Mesurements, 40, 539-543.
13. Font, L. I., Baixeras, C., Moreno, V. and Bach, J., 2008, Soil radon levels across the Amer Fault: Radiation Measurements, 43, 319-323.
14. Seminsky, K. Z. and Demberel, S., 2013, The first estimation of soil-radon activity near faults in Central Mongolia: Radiation Measurements, 49, 19-34.
15. King, C., King, B., Ewans, W. C. and Zhang, W., 1996, Spatial radon anomalies on active faults in California: Applied Geochemistry, 11, 497-510.
16. Yalım, H. A., Sandıkcıoglu, A., Unal, R. and Orhun, O., 2007, Measurements of radon concentrations in well waters near the Aksehir fault zone in Afyonkarahisar, Turkey: Radiation Measurements, 42, 505-508.
17. Baykara, O. and Dogru, M., 2006, Measurements of radon and uranium concentration in water and soil samples from East Anatolian active fault systems (Turkey): Radiation Measurement, 41, 362-367.
18. Irwin W. P. and Barnes I., 1980, Tectonic relations of carbon dioxide discharges and arthquakes: Journal of Geophyscal Research, 85, 3115-3121.
19. Yanitskiy I. N., Borobeynik V. M. and Sozinova T. V., 1975, Expression of crustal faults in helium field: Geotectonics, 9, 378-384.
20. Wakita, H., Nakamura., Y., Notsu, K., Naguchi, M. and Asada, M., 1980, A possible precursor of the 1978 Izu-Oshima-Kinkai earthquake: Science, 207, 882-883.
21. Perrier, F., Richon, P., Byrdina, S., France-Lanord, C., Rajaure, S., Koirela, B. P., Shrestha, P. L., Gautam, U. P., Tiwori, D., R., Revil, A., Bollinger, R., Contraires, S., Bureau, S. and Sapkota, S. N., 2009, A direct evidence for carbon-dioxide and radon-222 discharge in Central Nepal: Earth and Planetary Science Letters, 278, 198-207.
22. Ketin, I. , 1966, Anadolu'nun tektonik birlikleri. M.T.A Dergisi, 66 , 20-34.
23. Ozgul, N. , 1976, Torosların bazı temel jeolojik ozellikleri, Turkiye Jeoloji Kurumu Bulteni,19, 65-78.
24. Ozcan, A., Goncuoglu, M.C., Turan, N., Uysal, S., Sentürk, K. and Isık, A., 1988, Late Paleozoic evolution of the Kutahya-Bolkardag Belt: METU (Middle East Technical University) Journal of Pure and Applied Sciences, 21, 1/3, 211-220.
25. Karayigit, A.I., Akgun, F., Gayer, R.A. and Temel, A., 1999, Quality, palynology and paleoenvironmental interpretion of the Ilgın lignite, Turkey. International Journal of Coal Geology, 38, 219-236.
26. Pehlivan, E. and Arslan, G., 2006, Comparison of adsorption capacity of young brown coals and humic acids prepared from different coal mines in Anatolia: Journal of Hazardous Materials, 138 (2), 401-408.
27. Ediger, V. S., Berk, I. and Kosebalaban, A., 2014, Lignite resources of Turkey: Geology, reserves and exploration history: International Journal of Coal Geology, 132 (1), 13-22.
28. Huseyinca, Y. and Eren, Y., 2007, Ilgın (Konya) kuzeyinin stratigrafisi ve tektonik evrimi: Selcuk University, Journal of Faculty of Engineering and Architecture (in Turkish, with English abstract), (23 (1-2), 83-97.
29. Kandilli Rasathanesi web-page (Oct. 2014).
30. www.depremler.org/konya-depremleri-1 (26.10.2017)
31. MTA (Mineral Research and Exploration of Turkey, web-page-Oct,2114)

Hittite Journal of Science and Engineering, 2017, 5 (3) 191-194
ISSN NUMBER: 2148-4171
DOI: 10.17350/HJSE19030000093

The Unoccupied Surface States of the Cu(110) Substrate

Orhan Zeybek
Balikesir University, Department of Physics, Balikesir, TURKEY

ABSTRACT

Inverse photoemission spectroscopy is one of the advanced surface science technique for measuring unoccupied surface states with sufficient accuracy. The unoccupied surface states of the Cu(110) substrate has been investigated using an inverse photoemission spectroscopy with energy resolution of 0.5 eV. In this study, it has been introduced new unoccupied surface states. These unoccupied states are obtained from bulk bands and placed mainly in the outermost atomic layer. These states have been compared and contrasted with experimental and theoretical results. It has been also shown that at the $\overline{Y}$ point of the surface Brillouin zone, reflectance anisotropy spectra of the Cu(110) substrate possesses an unoccupied and occupied surface states.

Article History:
Received: 2017/10/07
Accepted: 2017/10/18
Online: 2018/09/30

Correspondence to: Orhan Zeybek, Balikesir University, Department of Physics, Balikesir, Turkey
Tel: +90 (537) 524-1298
Fax: +90 (266) 612-1215
E-Mail: ozeybek@balikesir.edu.tr

Keywords:
Inverse photoemission spectroscopy; Cu(110) substrate; Unoccupied surface states; Reflectance anisotropy spectra; Surface Brillouin zone.

INTRODUCTION

Studying the surface electronic structure of the solid are received great attention experimentally and theoretically. An electronic state, which localized to a solid surface, is named a surface state. Surface states of metals are known as an important candidate for the investigation of electronics properties. In the surface states, the electron–electron interactions have been studied [1,2]. The bulk of the solid obtained from *s*- and *p*-states possess a almost parabolic form. These new states are called "bulk states" at the surface. The wave functions of these states are localized near the solid surfaces and which decrease exponentially on both into the bulk and the vacuum of the material. Surface state is an electronic state established at the surface of the crystal.

The low index faces of metal surfaces, i.e. Cu, Ag and Au, contain two surface states, i.e. occupied and unoccupied. Electrons of surface states can scatter from defects and step edges at the surfaces. For the transition metal of Cu(110), the *s,p*-state bands are well identified. The bulk band of Cu(110) substrate that is on the Fermi level (E_F), holds an unoccupied surface state, which is lying about 2 eV above the E_F [3–5], and the other surface state crosses the E_F [4]. The bulk states are all *s,p* derived.

As is well known since more than two decades, surface states have been investigated with a combination of ultraviolet photoelectron spectroscopy (UPS) [7-9], inverse photoemission spectroscopy (IPES) [3,10-14] and theoretical work [10,11,15-17]. UPS offers a great technique for the occupied electronic states at metal surfaces. IPES provides results concerning to empty surface state bands on solid surfaces. In case of UPS and IPES, these techniques have their weaknesses and strengths in presenting surface states at metal surfaces.

IPES promises to be an important surface science technique in this research area because of its ability to probe unoccupied electronic structures [18,19]. In IPES basically three types of unoccupied surface states are observed: Shockley surface states [20] which are *sp*-like, Tamm states [21] which are *d*-like surface states (often associated with surface reconstruction) and image potential states. Shockley and Tamm states are also seen in angle resolved photoemission spectrum (ARPES) but image states are not.

Reflection anisotropy spectroscopy (RAS), UPS, IPES and X-Ray Photoelectron Spectroscopy (XPS), have been used in this study. It is therefore very fascinating now to have an experimental technique at hand to compare available data. The aim of this study is to clarify the unoccupied surface states and to compare available data. It is therefore worthwhile to study electronic states at the Cu(110) clean metal surface. In this paper, it is reported new surface states in the unoccupied region.

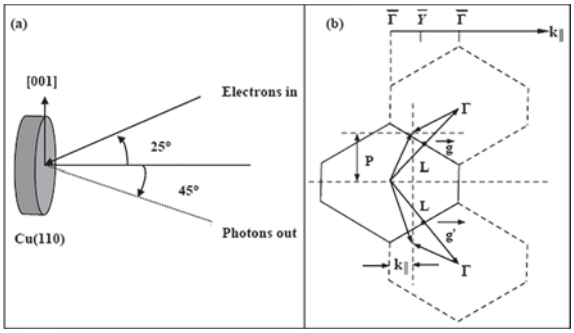

Figure 1. (a) For the IPES experimevvnts, the Cu(110) adjusted at the right angle. **(b)** SBZ diagram of the Cu(110) surface. The bulk reciprocal lattices are shown g and g′, p is the perpendicular wave vector.

EXPERIMENTAL

In this study, experiments were performed in an ultrahigh vacuum (UHV). This UHV contains Low Energy Electron Diffraction (LEED), Mass Spectrometer, UPS, IPES and XPS apparatus. The Cu(110) substrate was cleaned in UHV, the daily preparation involved Ar ion bombardment at 500 V for 30 minutes. After this procedure, the substrate annealed up to 600 K for 20 minutes. Cleanliness, surface order and surface orientation were verified by LEED and XPS. LEED presented a sharp (1′1) spots at room temperature (RT).

The IPES studies were completed in the base pressure of 1×10^{-10} Torr. The IPES produces an emission current of 40 μA. The photons radiated from the sample are reflected on Micro-Channels Plates (MCP) detector by a holographic circular diffraction grating which has a diameter of 92 mm, 3600 lines per mm, a concave radius of curvature of 300 mm, and a focal ratio of 3.3. The electron gun was adjusted at 25° and along the [110] direction. The geometry shown in Fig. 1 corresponded to the $\bar{Y}$ point of the surface Brillouin zone (SBZ) in reciprocal space. In case of keeping the angle of 45° between emitted photons and the sample surface normal position constant. The experiments were carried out at the $\bar{Y}$ point i.e. the relevant angles in the experiment were adjusted so as to keep $k_{\parallel}$ constant.

The ion gauges had to be shut off during the IPES measurements because light from the ion gauge produced a background signal in the MCPs. All of the chamber windows were also covered during IPES scans to avoid any source of photons in the chamber. Finally, IPES spectra were recorded.

RESULTS AND DISCUSSION

The IPES experiments were determined at 9.1 eV electron energy and fixed photon energy [3,10,11]. There are two important points to note that the first is that IPES experiment has been employed the fixed electron energy and different photon energy ranges. In other words, the unoccupied surface states were monitored by IPES technique at the fluorescent mode. The second is that IPES has been carried out at the $\bar{Y}$ point in the SBZ of the clean Cu(110), with fixed kinetic energy of 19 eV. The geometric procedure is set up for electrons at 25° and for emitted photons is set up at 45° at RT can be seen in Fig. 1. Fig. 2 shows IPES experimental results for the Cu(110). For At the $\bar{Y}$ point, a surface transition was supposed to be 2.2 eV for the Cu(110), an occupied surface state was seen at 0.4 eV below the E_F [8], an unoccupied surface state was found 1.8 eV above E_F [5].

Table 1 shows the peak positions along with the experimental and theoretical references. The unoccupied bulk and surface states were resolved with an IPES energy resolution of 0.5 eV.

The experimental binding energies of the unoccupied states of Cu(110) are reported at 2.5 eV [3], 2.0 eV [10], and 1.8 eV [5]. The calculated values are reported at 2.5 eV, 4.85 eV, 6.4 eV, 6.9 eV and 7.3 eV [22] and 5.63 eV [23]. There are no reports on the unoccupied states at 2.3, 8.0 eV, 8.8 eV and 9.4 eV as observed in this study. All the thirteen peaks are real because they were reproducible and the uncertainty of each peak, $\pm\sqrt{N}$, is less than count N. It is important to note that without any contamination of the substrate should be taken into account to confirm these unoccupied states.

The peak 2.5 eV from a surface state [3] was associated with a number of principles: First of all, the surface states should exit bulk structure of the clean Cu(110). Then, it should separate electron's momentum. Lastly, a surface state should be sensitivity to surface contamination. For the unoccupied surface state band on Cu(110) substrate with 2.0 eV at the SBZ, it has been established. The calculated value was reported at 5.63 eV according to the density of states

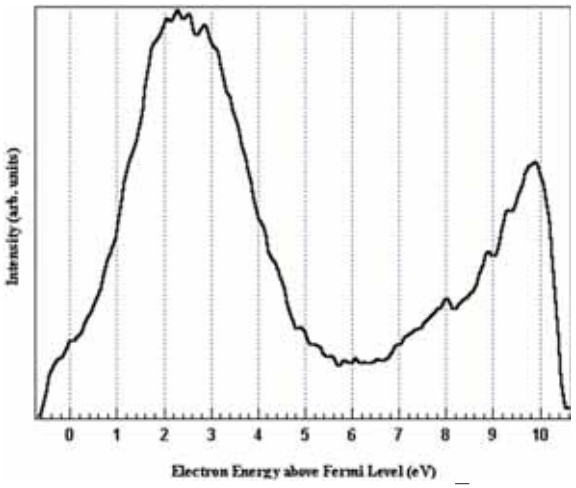

Figure 2. IPES spectrum of the Cu(110) obtained at the $\bar{Y}$ point in the SBZ, at RT and at off-normal electron incidence.

Table 1. Peak energies in eV of the unoccupied surface states for the Cu(110).

Peak Energies in (eV)		Other Experimental Results	Reference	Other Theoretical Results	Reference
1.7		1.8	[5]	1.7	[29]
2.0		2.0	[10]	-	-
2.3	New Peak	-	-	-	-
2.45		2.5	[3]	2.5	[22]
2.8	New Peak	-	-	-	-
4.8		-	-	4.85	[22]
5.2		5.5	[22]	-	-
5.8		-	-	5.63	[23]
6.2		-	-	6.4	[22]
6.8		-	-	6.9	[22]
8.0		-	-	7.3	[22]
8.8	New Peak				
9.4	New Peak				

calculations [23]. Using an angle resolved photoemission spectroscopy, the energy of the lowest (n= -1) state at Cu(110) $\overline{Y}$ point is identified to be E_F-0.39eV [6]. The following lowest surface state is provided 2.0 eV [8], 2.5 eV [1] and 1.8 eV [5]. The surface state of the Cu(110) was found at 5.5 eV (22) above E_F. The unoccupied surface state for the substrate is presented in Fig. 3. At the $\overline{Y}$ point of the SBZ, an energy of 2.1 eV is obtained using RAS. In this study, this state has been probed using IPES. A number of different groups [3–5,13,24–31] have been analyzed this state by theoretically.

As seen in Fig. 3, the peak at 2.1 eV is associated with shifts between *p*-type occupied surface state and *s*-type unoccupied surface state at the $\overline{Y}$ point of the SBZ. The other peak at 4.2 eV in Fig. 3 is correlated with a shift at the $\overline{X}$ of the SBZ between the bulk *d*-bands of the occupied state and *p*-type surface state of the unoccupied state. At $\overline{Y}$ point, the occupied surface state possesses p_y character. The transition between states of the occupied and unoccupied is only permitted for light which polarized along [001] direction.

For the Cu(110), surface states are established in bulk band gaps. These bulk band gaps are positioned near the $\overline{Y}$

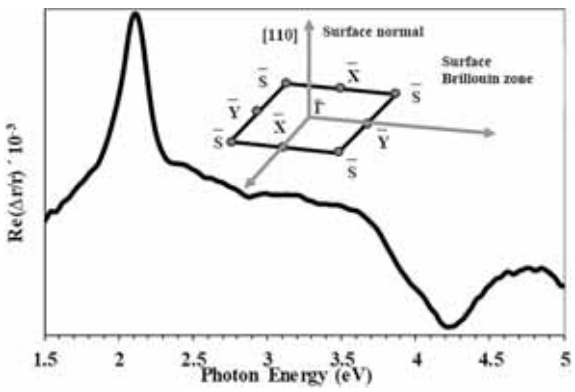

Figure 3. RAS spectra for the clean Cu(110) substrate.

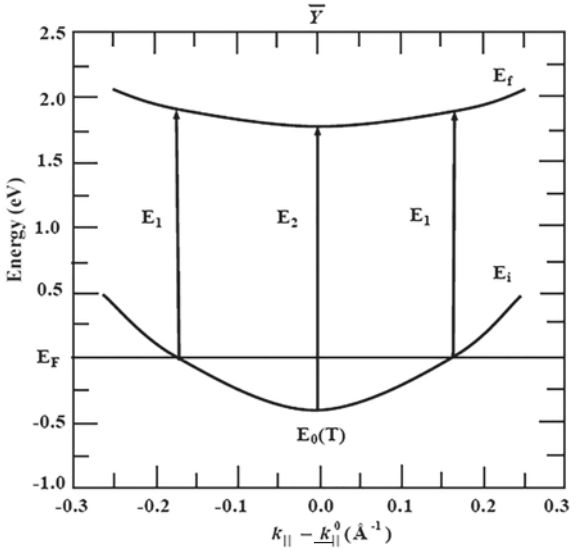

Figure 4. Energy illustrations nearby $\overline{Y}$ point.

point. The Cu(110) surface possesses one partly occupied and one unoccupied surface states as displayed in figure 4. For Cu(110) substrate, the Shockley state around $\overline{Y}$ point is shown anisotropic behavior. There is an evidence for this finding by using scanning tunneling microscopy [32].

At metal surfaces, such as Cu, electrons of the surface state spread from step edges and defects. These cause an increase quantum interference patterns.

CONCLUSION

In this study, the new unoccupied surface states of the Cu(110) at the $\overline{Y}$ point have been obtained using IPES surface science technique. The new unoccupied surface states are obtained from bulk bands and placed mainly in the outermost atomic layer. The findings have been compared and contrasted with available experimental and theoretical data. It has been also shown that reflection anisotropy spectra of the clean Cu(110)

substrate possesses surface states at the $\overline{Y}$ point.

ACKNOWLEDGEMENTS

The author acknowledges Balikesir University for the support. The author also sincerely thanks to Dr. S.D. Barrett and A. M. Davarpanah at University of Liverpool Surface Science Research Centre, for their technical assistance.

REFERENCES

1. Petek H, Ogawa S. Femtosecond time–resolved two–photon photoemission studies of electron dynamics in metals. Prog Surf Sci 56(4) (1997) 239–310.
2. Osma J, Sarria I, Chulkov EV, Pitarke JM, Echenique PM. Role of the intrinsic surface state in the decay of image states at a metal surface. Phys Rev B 59(16) (1999) 10591–10598.
3. Bartynski RA, Gustafsson T, Soven P. Observation of an unoccupied surface state on Cu(110) by inverse photoemission. Phys Rev B 31 (1985) 4745.
4. Goldmann A, Dose V, Borstel G. Empty electronic states at the (100), (110), and (111) surfaces of nickel, copper, and silver. Phys Rev B 32 (1985) 1971.
5. Jacob W, Dose V, Kolac U, Fauster T, Goldmann A. Bulk, surface and thermal effects in inverse photoemission spectra from Cu(100), Cu(110) and Cu(111). Z Phys B Condens Matter 63 (1986) 459–470.
6. Petersen L, Schaefer B, Lægsgaard E, Stensgaard I, Besenbacher F. Imaging the surface Fermi contour on Cu (110) with scanning tunneling microscopy. Surf Sci 457 (2000) 319–325.
7. Straube P, Pforte F, Michalke T, Berge K, Gerlach A, Goldmann A. Photoemission study of the surface state at $\overline{Y}$ on Cu(110): Band structure, electron dynamics, and surface optical properties. Phys Rev B 61 (2000) 14072.
8. Kevan S. High–resolution angle–resolved photoemission study of the Cu(011) surface state. Phys Rev B 28 (1983) 4822.
9. Matzdorf R, Gerlach A, Hennig R, Lauff G, Goldmann A. A spectrometer arrangement for high–resolution angle–resolved UV–photo–emission using linear–polarized laboratory photon sources. J Elec Spec and Rel Phen 94 (1998) 279.
10. Reihl B, Frank KH. Unoccupied electronic surface states on Cu(110). Phys Rev B 31 (1985) 8282.
11. Smith NV, Woodruff DP. Inverse photoemission from metal surfaces. Prog in Surf Sci 21 (1986) 295–370.
12. Dose V. Study of empty electronic states by inverse ultraviolet photoemission. J Phys Chem 88 (1984) 1681–1690.
13. Smith NV. Inverse photoemission. Rep Prog Phys 51 (1988) 1227.
14. Himpsel F. Inverse photoemission from semiconductors. Surf Sci Rep 12 (1990) 3–48.
15. Woll J, Meister G, Barjenbruch U, Goldmann A. Harmonic generation and photoemission. Appl Phys A: Mater Sci Process 60 (1995) 173.
16. Schneider R, Dürr H, Fauster Th, Dose V. Temperature dependence of the inverse photoemission from copper surfaces. Phys Rev B 42 (1990) 1638.
17. Martin DS, Weightman P. Reflection anisotropy spectroscopy: a new probe of metal surfaces. Surf Interface Anal 31 (2001) 915–926.
18. Dose V. Ultraviolet Bremsstrahlung spectroscopy. Prog Surf Sci 13 (1983) 225.
19. Smith NV. Inverse photoemission and related techniques. Vacuum 33 (1983) 803–811.
20. Shockley W. On the Surface States Associated with a Periodic Potential. Phys Rev 56 (1939) 317.
21. Tamn I. Exchange forces between neutrons and protons and fermi theory. Z Phys 76 (1932) 848.
22. Chen CT, Smith NV. Energy dispersion of image states and surface states near the surface–Brillouin–zone boundary. Phys Rev B 35 (1987) 5407.
23. Speier W, Zeller R, Fuggle JC. Studies of total density of states of metals up to 70 eV above E_F. Phys Rev B 32 (1985) 3597.
24. Tang D, Su C. Heskett D. The unoccupied electronic structure of Na/Cu(110). Surf Sci 295 (1993) 427–432.
25. Su C, Tang D, Heskett D. Two–dimensional unoccupied electronic band structure of clean Cu(110) and (1 ✣ 2) Na/Cu(110). Surf Sci 310 (1994) 45–51.
26. Memmel N. Monitoring and modifying properties of metal surfaces by electronic surface states. Surf Sci Rep 32 (1998) 91–163.
27. Bartynski RA, Gustafsson T. Experimental study of surface states on the (110) faces of the noble metals. Phys Rev B 33 (1986) 6588.
28. Smith NV. Phase analysis of image states and surface states associated with nearly–free–electron band gaps. Phys Rev B 32 (1985) 3549.
29. Redinger J, Weinberger P, Erschbaumer H, Podloucky R, Fu CL, Freeman AJ. Inverse–photoemission spectra and electronic structure of the Cu(110) surface. Phys Rev B 44 (1991) 8288.
30. Smith NV. Chen CT. Spectroscopic constraints on the potential barrier at metal surfaces. Surf Sci 247 (1991) 133–142.
31. Goldmann A, Donath M, Waltmann W, Dose V. Momentum–resolved inverse photoemission study of nickel surfaces. Phys Rev B 32 (1985) 837.
32. Petersen L, Schaefer B, Lægsgaard E, Stensgard I, Besenbacher F. Imaging the surface Fermi contour on Cu(110) with scanning tunneling microscopy. Surf Sci 457 (2000) 319.

Hittite Journal of Science and Engineering, 2018, 5 (3) 195-201
ISSN NUMBER: 2148-4171
DOI: 10.17350/HJSE19030000094

Probing of the Unoccupied Electronic States in Solids by Inverse Photoemission Spectroscopy

Orhan Zeybek
Balikesir University, Faculty of Science and Arts, Department of Physics, Cagis Campus, Balikesir, Turkey.

ABSTRACT

This paper reviews the probability of probing the unoccupied electronic states in solids by inverse photoemission spectroscopy (IPES). IPES is a surface science technique to analysis the unoccupied electronic states above the Fermi level. IPES is a complementary technique to photoemission. In the IPES technique, the incoming particles are electrons and the outgoing particles are emitted photons that are consequently created by them therefore this technique is named as Bremsstrahlung Isochromate Spectroscopy. This is a common measuring mode because the photons of particular energy are identified. IPES has established one of the most powerful techniques in the study of the unoccupied electronic states in solids.

Article History:
Received: 2017/10/07
Accepted: 2017/10/11
Online: 2018/09/30

Correspondence to: Orhan Zeybek
Balikesir University, Faculty of Science and Arts, Department of Physics, Cagis Campus, Balikesir, Turkey
Tel: +90 (537) 524-12 98 /
Fax: +90 (266) 612-12 15
E-Mail: ozeybek@balikesir.edu.tr

Keywords:
Inverse photoemission spectroscopy; Photoemission spectroscopy; Unoccupied electronic states; Fermi level; Free–electron–like transitions.

INTRODUCTION

In order to probe the electronic structure of a solid, it is useful to know the nature of both the occupied and unoccupied states around the Fermi level (E_F). Inverse photoemission spectroscopy (IPES) is probed the unoccupied electronic states of solids above the E_F [1]. IPES is a complementary surface science technique to the photoemission spectroscopy (PES) which analyses occupied states below the E_F.

In the PES, a photon incident on a sample excites an electron in an occupied state of the sample into an unoccupied state above the E_F, the electron in this final state being the detected particle. In IPES an electron incident on a sample couples into an unoccupied state and makes a radiative transition to another lower lying unoccupied state above the E_F, in this case the emitted photon is detected. The two processes (PES and IPES) for the occupied and unoccupied electronic states are shown in Fig. 1.

In PES a photon promotes an electron in an occupied state below E_F into an unoccupied state above vacuum level (E_{Vac}). In IPES an electron that has coupled to an unfilled state above E_{Vac} makes a transition into an unoccupied state between E_{Vac} and E_F with a emission of photon. In the IPES technique, the incoming particles are electrons and the outgoing particles are emitted photons, which come from transitions from the free–electron–like incoming electron state into unoccupied states above the E_F of the investigated sample.

More than two decade of work on IPES has considerably advanced the field of study and several reviews at the respective level of maturity were published [2-5]. In early days the development was oriented along known results from PES, which were simply reproduced for the case of unoccupied levels. Problems were tackled which had no precedent in ordinary PES [6]. The unoccupied states can be examined by two-photon photoemission (2PPE) or IPES [2-4]. Because of the low photon energy, 2PPE indicates high energetic resolution.

Theory of Inverse Photoemission Spectroscopy

As it is known in PES process, the sample is bombarded with photons from a UV source. As ultraviolet (UV) photons have lower photon energy than X rays and thus interact only with the electrons in the valence shells or conduction band, the PES can therefore provide information about the electronic band structure of semiconductors and metals. The kinetic energy of the emitted electrons can be calculated by using Equation 1:

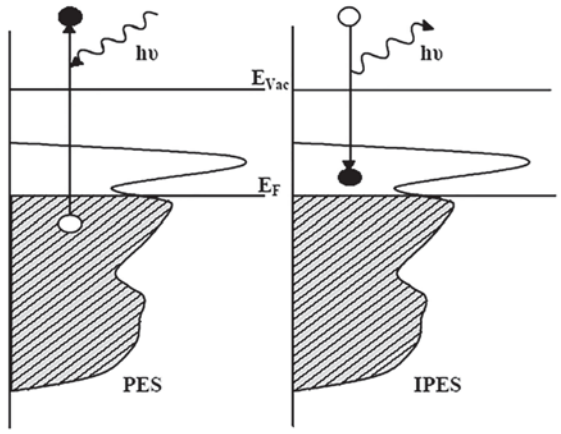

Figure 1. Energy level diagram comparing the PES and IPES processes.

$$KE = h\upsilon - BE - e\Phi \quad (1)$$

The UV source is a gas discharge lamp. Three source gases were used in these studies, Helium (He), Neon (Ne) and Argon (Ar). The emission lines for He(I) is 21.2 eV, for Ne(I) is 16.8 eV and for Ar(I) is 11.8 eV.

The IPES theory was established by Pendry [7,8]. Pendry exposed that IPES can be defined as PES with the exception of some geometric and phase space coefficients. For the occupied bands [9], *k*-resolved IPES allows that the energy dispersion E(*k*) of unoccupied electronic bands can be explained by angle-resolved photoelectron spectroscopy (ARPES).

Pendry [7,8] and Fauster *et al.* [10] declared that the IPES procedure is theoretically the time reversal of PES and two techniques have a Golden Rule, Equation (2) type appearance for the cross section, σ, and the same type of dipole matrix element. Smith *et al.* [11] assumed from molecules that IPES is not the time reversed version of the PES method. IPES contains a transition from the n to n+1 electron system. The difference is principally essential near threshold. It should be noted that the primary state in IPES is the final state in PES, and the other way around. As expressed by Himpsel [12], the cross section can be specified as:

$$\sigma \propto (1/\ j_i)\sum_f \left| < \Psi_f \left| H_I \right| \Psi_i > \right|^2 \quad (2)$$

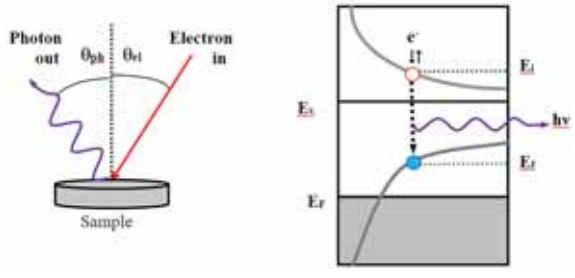

Figure 2. Schematic of the IPES process

where Ψ_i is the initial state with no photons and Ψ_f is the final state contains a band electron plus a photon in IP initial and final states lie above the E_F as shown in Fig. 2. H_I is the interaction Hamiltonian. The dipole matrix element is given by:

$$< \Psi_f \mid H_I \mid \Psi_i > \propto \int \vec{A} \cdot \vec{J}_{fi} d^3 r \quad (3)$$

where $\vec{A}$ is the electromagnetic vector potential. The non-relativistic current takes the form:

$$\vec{J}_{fi} \propto (1/2) e(\Psi_f{}^* \vec{\nabla} \Psi_i - \Psi_i{}^* \vec{\nabla} \Psi_f \quad (4)$$

The experimental development of IPES has been slow compared to PES this is principally as a result of the low cross section for emission of photons in IPES. The ratio of the cross sections [11,13] is specified by:

$$r = \frac{\sigma_{IPES}}{\sigma_{PES}} \approx \left(\frac{\lambda_{el}}{\lambda_{ph}} \right)^2 \equiv \frac{E^2{}_{ph}}{2 m_{el} c^2 E_{el}} \equiv \alpha^2 \frac{(E_{ph}/R)^2}{4(E_{el}/R)} \quad (5)$$

where λ_{el} and λ_{ph} present the wavelengths of the electron and photon respectively. E_{ph} is the photon energy, E_{el} is the kinetic energy of the electron, m_{el} is the electron mass, R is the Rydberg constant, and α is the fine structure constant which is $e^2/\hbar c \sim 1/137$. This ratio originates from the different amounts of phase space. The cross section ratio is basically specified by the square of the fine structure constant α^2 μ 5 ´10^{-5}. This constant provides increase to the low quantum yield of IPES (~10^{-8} photons/electron) relative to PES (~10^{-3} electrons/photon, discounting inelastic secondary electrons) [11,13]. Therefore the base signal degrees in IPES are about five times weaker than in PES.

EXPERIMENTAL METHODS IN IPES

IPE experiments can be carried out in two different modes requiring different detection systems. In figure 3, an illustration of the two different IPES modes is shown. Fig. 3(a) represents the isochromat mode, Fig. 3(b) the fluorescence mode. They are developed to make best use of the solid angle of photon collection and the efficiency of photon detection.

Isochromat mode

As shown in Fig. 3(a), the isochromat mode involves scanning the incident electron energy whilst detecting photons emitted at a fixed energy. The isochromat mode is equivalent to the time reversed method of recording ARPES spectra where an electron spectrum is measured for fixed incident photon energy. Detectors for the isochromat mode include the Geiger Muller counter (14). This consists of a stainless steel tube closed at one end by a Calcium Flouride (CaF_2) entrance window and filled with Iodine gas (I_2). The combination of the transmission

cut-off of the CaF_2 window at high energy and the ionization threshold of the I_2 produce an overall energy window centred around 9.7eV with a bandwidth of 0.8eV. A central electrode floated to a positive potential, collects the electron cascade current generated by any incident photons with an energy lower than the transmission cut-off of the CaF_2 but higher than the ionization potential of the I_2.

Fluorescent mode

As shown in Fig. 3(b), the energy of the electrons in fluorescent mode are hold constant then the energy of the photon is determined with a large aperture grating. This mode allows the initial state constant and obtaining the transitions between the initial and the final state above the E_F. In this circumstance, this mode is easier than in isochromat mode [10].

Momentum (k) Resolved IPES

In an IPE experiment a collimated beam of electrons with a well defined kinetic energy E_{kin} and known incidence angle θ enter a sample. These electrons couple to bulk states of the sample above the E_{vac}. An initial state with energy E_i and wave vector k_i, the electrons possess radioactive decay transitions to the unoccupied final state between E_F and E_{vac} having energy E_f and wave vector k_f. The emitted photons with quantized energy hυ are detected at an emission angle α. Applying conservation of energy to the process gives

$$E_i = E_f + h\upsilon \tag{6}$$

using momentum conservation for the radiative transition yields:

$$k_i = k_f + G + q \tag{7}$$

where G indictes a reciprocal lattice vector and q presents the wave vector of the emitted photon. For low energy photons ~100eV or less the magnitude of q is small compared with the size of the Brillouin zone. It is then a reasonable approximation to neglect G and q in the conservation of momentum, Equation 7 then becomes $k_i = k_f$. Initially only the wave vector in the vacuum K of the incident electrons is known. When the electrons enter the sample they experience an attractive force of unknown magnitude due to the crystal potential. The component of the wave vector in the solid $k_\perp$ is then greater than $K_\perp$ in the vacuum therefore there is a problem in determining $k_\perp$ in the final state. The component of the wave vector parallel to the surface is protected because potential is periodic. This results in the condition:

$$k_{i\|} = k_{i\|} + G_\| \tag{8}$$

where $G_\|$ indicates surface reciprocal lattice vector. For sufficiently low initial state energies $G_\| = 0$ can be used. Then $K_{i\|}$ is given by:

$$K_{i\|} = (2m/\hbar^2(E_f + h\upsilon - \Phi_s))^{1/2}\sin\theta \tag{9}$$

where ϕ_s is the workfunction of the sample. It is then possible to determine the final state energy as a function of wave vector parallel to the surface $E_f(k_\|)$ from experimental data, which can be compared with the predicted band structure from theoretical calculations. Experiments are usually done in mirror planes. In mirror planes different bands may become degenerate; this can reduce the complexity of the measured spectra. Also as the wavefunctions of the incoming electrons have even parity they can only couple to initial states of even parity [7], this reduces the number of possible transitions providing a further simplification. The component of the wave vector perpendicular to the surface is not protected. However k may be determined by making an assumption about the initial electronic state. The simplest approximation is of a free electron like initial state with a constant inner potential V_0. At this stage, for normal electron incidence i.e. $k_\| = 0$ the wave vector normal to the surface is specified by:

$$k_\perp = \left[2m(E_i - V_0)\right]^{1/2}/\hbar \tag{10}$$

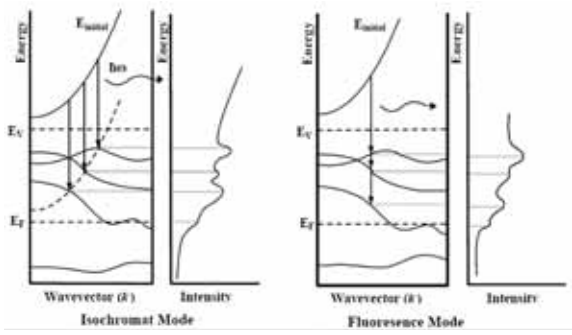

Figure 3. Energy level diagram showing isochromat and fluorescence modes for IPES.

Other Spectroscopies Used To Study Unoccupied Surface States

A number of other techniques are employed to investigate the unoccupied states above the E_F these include appearance potential spectroscopy (APS) [16], X-Ray absorption spectroscopy (XAS) [17], electron energy loss spectroscopy (EELS) [18], two photon spectroscopy (2PPE) [19], Scanning Tunnelling Spectroscopy (STS) and bremsstrahlung isochromat spectroscopy (BIS). IPES has advantages all above techniques that IPES measures energy E, momentum $\hbar k$, spin, energy-band dispersion $E(\boldsymbol{k})$, and point group symmetry of unoccupied electron state. The uncertainty principle orders that the spatial resolution cannot be of atomic dimensions if the momentum information is to be kept constant [12].

For the XAS, electrons are resonantly excited from an occupied valance-band state to an unoccupied valence-band state. Therefore XAS increases atomic resolution by giving up the momentum information [20] but band mapping as a function of *k*–parallel is not generally possible.

2PPE determines momentum information, as in IPES. This method is limited to long-lived electronic states [12]. Otherwise, the intermediate state cannot be populated enough without destroying the samples.

STS is a local probe and the problem is the same as XAS. This technique has a very good energy resolution. This method is not limited to vacuum environments but it is less direct than IPES.

In high energy IPE or BIS as it is known, a high energy beam of electrons (~1500 eV) is used. For such high energies the momentum of the emitted photon is non negligible and the process is not *k*-conserving. Therefore BIS reveals little about the wavevector of the unoccupied states, however it is one of the most direct methods for investigating the density of unoccupied states. The use of electrons with energies in the ultraviolet region below ~30eV allows the wave vector and the energy of the unoccupied states above the Fermi level to be probed. For energy of approximately 30 eV the elastic mean free path of electrons is approximately 10 to 20 Å. Therefore low energy IPE is a perfect method for the investigation of the surfaces and interfaces

Experimental Components of IPES

The experimental set up was designed to maximize angle and efficiency of photon because the problems associated with IPES such as: (i) weak signal, (ii) space charge influences that make an upper limit on the incident electron current. Fig. 4 shows the cross section of an advanced IPES spectrometer. It has the following feature: The Spherical Grating (SG), the Multi-Channel Plate (MCP) detector with digital read out and a movable electron gun.

Electron Source of IPES

The electron gun for the IPES experiments was designed to have good energy resolution and was capable of delivering high currents to overcome the low cross section for the production of photons. The thermionic electron emitter was a low work function type BaO source. In this type of electron source, BaO is heated to a temperature high enough (operating at 800 - 1200 °C) to give some electrons sufficient energy to escape the work function barrier at the surface into the vacuum [21,22].

Fig. 5 shows a digital photo of the IPES electron source and analyzer. The electron gun is mounted on a rotatable

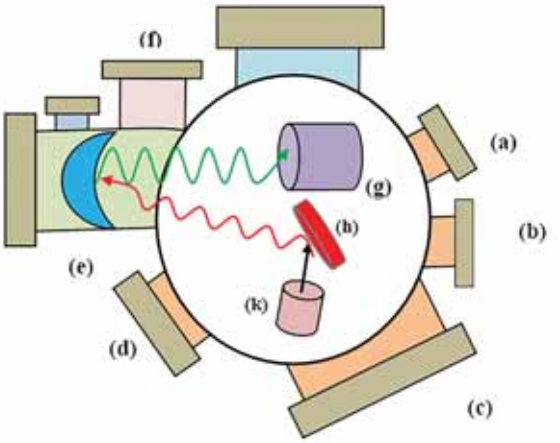

Figure 4. The cross section of the IPES spectrometer (a) X-ray Gun, (b) UV Lamp, (c) Rotatable Electron Gun and Analyser, (d) Window, (e) Spherical Grating, 3600 lines/mm, (f) Shutter and Access, (g) MCP and RAE, (h) Sample, (k) Electron Gun

platform allowing the angle of incidence to be adjusted without disturbing the angle of emission, permitting angle resolved studies. The movable electron gun allows the variation of photon yield with electron direction to be measured at a fixed photon azimuth angle. It is also make it possible to measure normal and off normal incidence spectra from clean and deposited surfaces with photon emission either near normal or near parallel to the surface which helps distinguish bulk states of different symmetry.

Fig. 6 shows schematic of a Stoffel–Johnson type electron gun [22] which has been used for IPES experiments in this thesis and was designed to give a divergence of $\Delta\theta \sim 5°$ for monoenergetic electrons in the range 5-50 eV.

As shown in figure 6, the electron gun has a circular emitting area of ~ 1 mm diameter, which also determines the diameter of the electron beam. The focal length of the electron gun is electronically adjustable. If the cathode focus distance is rised, the maximum focused current is decreased by radial space charge forces. It was found experimentally that at a typical emission current of 40 μA and electron energy of 19 eV, then ~ 80 % of the emission current reaches the sample.

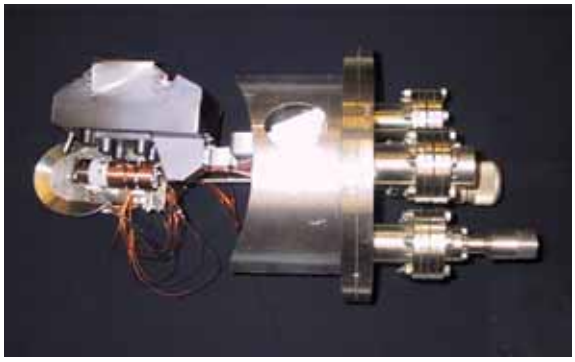

Figure 5. A digital photo of the IPES electron source and analyser

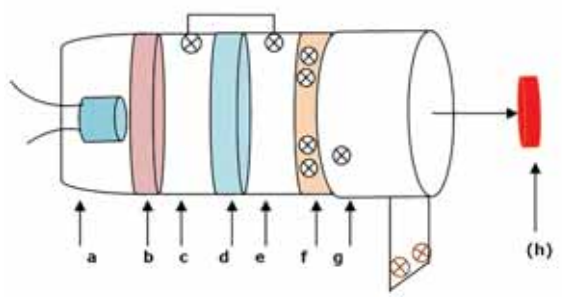

Figure 6. Schematic of the electron optical components of electron gun, (a) BaO cathode, (b) ceramic, (c) anode, (d) ceramic, (e) deflector electrode, (f) ceramic, (g) final lens, (h) sample

Detection system in IPES

The photon emitted from the sample are reflected on Micro-Channels Plates (MCP) detector by a holographic circular diffraction grating which has a diameter of 92 mm, 3600 lines per mm, a concave radius of curvature of 300 mm, and a focal ratio of 3.3. The output of electrons from the MCP can be seen either straight on a phosphor screen, or indirectly by the charge pulses incident on an anode, as shown in Fig. 7(a), behind the MCPs [23].

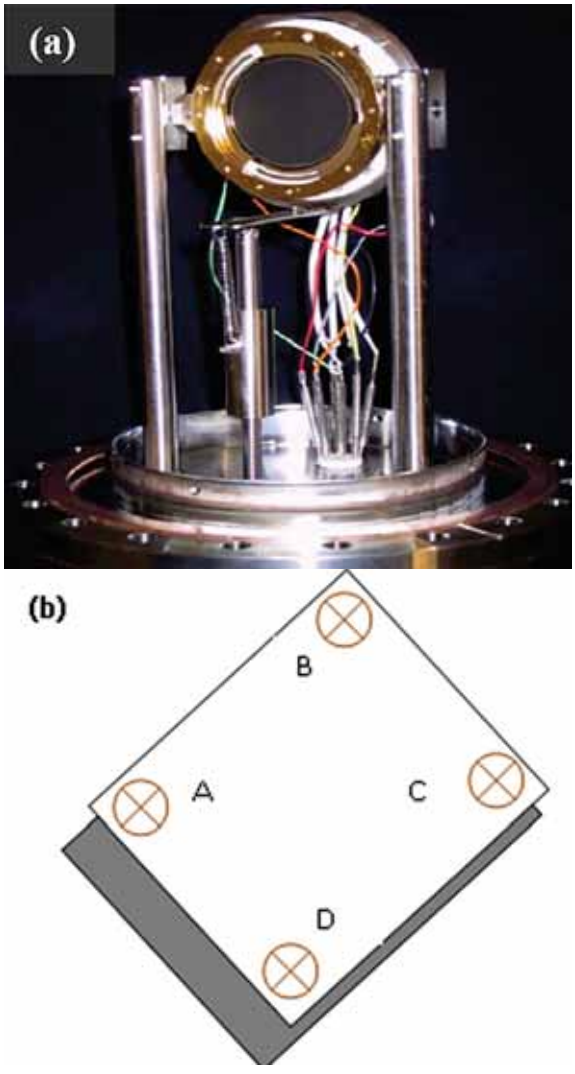

Figure 7. IPES detection system, (a) MCPs, (b) RAE

The MCP detector assembly, model 3394A supplied by Quantar Technology Inc. USA, has been used. It is made of lead glass with a coating of Nichrome on the surface acting as the electrode. Additionally the front plate is coated in KBr to increase the sensitivity to ultra violet (UV) photons. There are two circular plates of 0.46 mm thickness, back to back with 100 channels along the active diameter of 40 mm. A typical electron gain for the two plate stack is 5×10^6. It operates in an open face mode with a ratio of ~ 64%. The anodes are shaped resistive sheets.

The photon detection system also includes a position sensitive Resistive Anode Encoder (RAE) behind two MCPs electron multipliers. Each incident electron produces a detectable charge pulse on the resistive anode. The RAE produces charge division between four output electrodes at the corners A, B, C and D, see Fig. 7(b), proportional to the position of the centre of gravity of the charge pulse. The charge sensitive amplifiers convert the low level charge pulses into higher level shaped bipolar pulses suitable for input into the position analyser electronics. The position analyser electronics generates an analogue voltage output proportional to pulse position coordinates that may be calculated from the charges, Q_A, Q_B, Q_C, Q_D collected at the four electrodes:

$$Q_{Tot} = Q_A + Q_B + Q_C + Q_D \tag{11}$$

$$X = \frac{Q_B + Q_C}{Q_{Tot}} \tag{12}$$

$$Y = \frac{Q_A + Q_B}{Q_{Tot}} \tag{13}$$

The AD convectors are converted the peak amplitudes from analogue to digital. The coordinates can be calculated using the above formulations. The digital data are moved to a computer for this calculation. The coincidence count rate for the experiments in this thesis is ~ 200 – 300 counts per sec. Additional shielding of the resistive anode aperture was provided to make sure that only the reflected photons can reach the detector system.

The setup of the detectors is calculated by the aid of etched polycrystalline copper foil carrying a square grid pattern. An approximate point source ~ 1 mm of electrons is sent on the Cu foil. Photons were emitted toward the mirror and then were reflected onto the MCPs. The four anode channels are established for operation of the peak detection circuits. The images can be figured out by the X and Y coordinates.

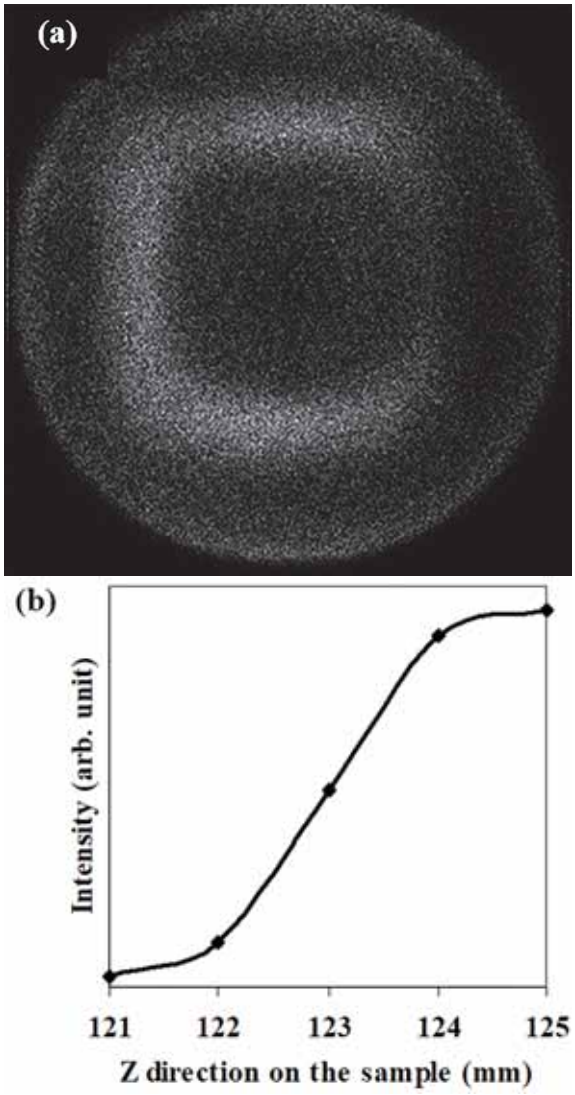

Figure 8. **(a)** UV illumination Image **(b)** Intensity vs Cu foil position using IPES.

Fig. 8(a) shows an image of the calibration from the Cu foil, using the latest version of Image SXM software [24]. The calculated {X, Y} coordinates are binned into a 256 ´ 256 pixels image and expose clearly the over the circular active area of the detector.

In order to get good focusing over the entire area, the detector sample and grating are mounted tangentially to the Rowland circle [25]. This gives a practical linear energy scale over the horizontal coordinate, X direction, of the channel plates. Since the image at the entrance slit does not cover the whole channel plate, it is possible to mask out a narrow band of the slit with aid of the control of the electronics unit.

Energy Resolution of IPES

There are two types of energy resolution, so the first one is the absolute resolution, ΔE, which is described as the Full Width at Half-Maximum (FWHM) height of a specific measured peak. The second is the relative resolution, R, that is expressed as the ratio of ΔE to the kinetic energy, E_0 of the peak position is given by:

$$R = \Delta E / E_0 \tag{14}$$

For high resolution analysis the measured peak width should be reduced to the lowest possible level. The resolution of the IPES system is controlled by several influences as mentioned below:

1. The thermal energy distribution of the electron beam is one of the influences. The low work function of BaO dispenser cathode used in the electron gun can be operated at temperatures as low as 800 °C. This is found during the degassing of BaO cathode tungsten filament using infrared thermometer. The thermal energy of electrons is given by 3/2(KT), where K is the Boltzman constant and T is the cathode temperature in Kelvin. For the cathode temperature of 800 °C, The thermal energy is ~0.14 eV.
2. The spot size of the electron beam at the sample is a minimum of ~ 1 mm due to space charge limitation. This is also found experimentally by mounting phosphor screen front of the electron gun.
3. One of procedures of photon collection and photon energy analysis is illustrated schematically in Fig. 9. This method employs a grating spectrograph. The aberration of the grating is the other factor effecting the resolution. Ray- tracing calculations [26,27] for the experimental geometry show that a point source of 19 eV radiation is focused onto the Rowland circle over an area of 90 μm wide and 3 mm high. This represents to an energy resolution of 0.02 eV, which is negligible in comparison to the electron energy spread.
4. The dispersion of the grating can be effected on the total energy resolution of the IPES system but it is negligible in comparison to the electron energy distribution.
5. The spatial resolution of the MCP detector is 0.4 mm. The resolution limit of the grating is small compared to the resolution limit set by the electron beam.
6. The distribution is detected a parabolic dispersion along a particular k-space direction in accordance with:

$$E(k_{\|}) = (\hbar^2 / 2m^*)(k_{\|} - k_{\|}^0)^2 + E_0 \tag{15}$$

where $m^* = (m_{el} \acute{} m_{eff.})$ and m_{el} is the free electron rest mass, $k_{\|}$ is the electron wave vector parallel to the surface, and E_0 provides the bottom of the parabola at $k_{\|}^0$. According to Equation 15, the momentum resolution of the instrument

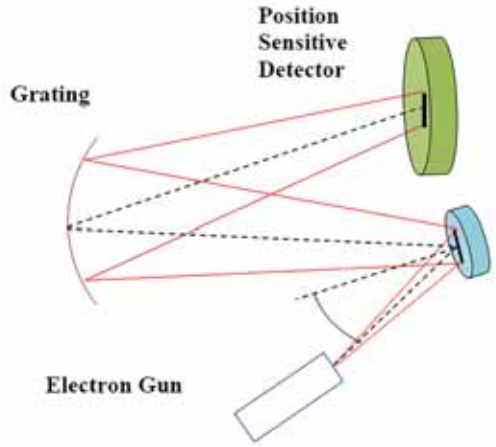

Figure 9. Grating spectrograph with parallel photon detection and analysis in IPES

can be determined by the angular distribution of the incident electron beam at the sample. The electron gun has been design to produce a full angular distribution of $\Delta\theta \sim 5°$ this gives a momentum resolution of $\Delta k = 0.1$ Å^{-1} at 5 eV. The momentum broadening is increased to ~0.2 Å^{-1} at a beam energy of 20 eV [22]. The total resolution of the IPES system has been determined to be ~ 0.5 eV experimentally.

CONCLUSION

One of the main surface science techniques for investigating the empty electronic states is IPES. In this study, IPES is briefly reviewed in the basic physical process for theoretically and experimentally. IPES method can be employed to investigate unoccupied surface states of solids.

ACKNOWLEDGEMENTS

The author acknowledges Balikesir University for the support. The author also sincerely thanks to Dr. S.D. Barrett and A. M. Davarpanah at University of Liverpool Surface Science Research Centre, for their technical assistance.

REFERENCES

1. Andrews PT, Collins IR, Inglesfeld JE. Inverse photoemission and how it is used, in: Fuggle JC, Inglesfield JE (Eds.). Topics in Applied Physics: Unoccupied Electronic States, Fundamentals for XANES, EELS, IPS and BIS. Pp. 243–276, (1992).
2. Dose V. Study of empty electronic states by inverse ultraviolet photoemission., J Phys Chem 88 (1984) 1681–1690.
3. Smith NV. Inverse photoemission. Rep Prog Phys 51 (1988) 1227.
4. Himpsel F. Inverse photoemission from semiconductors. Surf Sci Rep 12 (1990) 3–48.
5. Sanada N, Shimomura M, Fukuda Y. Inverse photoemission spectrometer using a BaF_2 window for a low-pass filter. Rev Sci Instrum 64 (1993) 3480.
6. Yokoyama K, Nishihara K, Mimura K, Hari Y, Taniguchi M, Ueda Y, Fujisawa M. Bandpass photon detector for inverse photoemission spectroscopy. Rev Sci Instrum 64 (1993) 87.
7. Pendry JB. New Probe for Unoccupied Bands at Surfaces. Phys Rev Lett 45 (1980) 1356.
8. Pendry JB. A Generalized Friedel Sum–Rule. Phys C Solid State Physics 14 (1981) 1137–1143.
9. Reihl B, Frank KH. Unoccupied electronic surface states on Cu(110). Phys Rev B 31 (1985) 8282.
10. Fauster Th, Himpsel FJ, Donelon JJ, Marx A. Spectrometer for momentum-resolved bremsstrahlung spectroscopy. Rev Sci Instrum 54 (1983) 68.
11. Smith NV, Woodruff DP. Inverse photoemission from metal surfaces. Prog in Surf Sci 21 (1986) 295–370.
12. Himpsel FJ. Inverse photoemission from semiconductors. Surf Sci Rep 12 (1990) 3–48.
13. Johnson PD, Davenport JW. Calculated inverse photoemission cross sections from adsorbed molecules. Phys Rev B 31 (1985) 7521.
14. Smith NV, Chen C, Tranquanda JM, Johnson PD. Unoccupied states on Pd(110) and the surface potential barrier. Phys Rev B 38 (1988) 12259.
15. Hermanson J. Final–state symmetry and polarization effects in angle–resolved photoemission spectroscopy. Solid State Commun 22 (1977) 9–11.
16. Park RL, Houston E. L–Shell Soft–X–Ray Appearance–Potential Spectra of the 3d Transition Metals. Phys Rev B 6 (1972) 1073.
17. Prinz R, Koninsberger K (Eds.). X–Ray Absorption: Principles, Applications and Techniques of EXAFS, SEXAFS and XANES, Wiley, New York, 1986.
18. Marton L, Lederer LB, Mendlowitz H. Characteristic energy losses of electrons in solids", Advances in Electronics and Electron Physics 7 (1955) 183–238.
19. Giesen K, Hage F, Himpsel FJ, Riess JH, Steinmann W. Two–photon photoemission via image–potential states. Phys Rev Lett 55 (1985) 300.
20. Borca CN, Komesu T, Dowben PA. Comparing inverse photoemission and X–ray absorption spectroscopies. J Electron Spectrosc Relat Phenom 122 (2002) 259–273.
21. Briggs D, Seah MP (Eds.). Practical Surface Analysis: Auger and X–Ray Photoelectron Spectroscopy, second ed. Wiley Interscience New York 1 (1990) 61.
22. Stoffel NG, Johnson PD. A low–energy high–brightness electron gun for inverse photoemission. Nuclear Instruments and Methods in Physics Research A 234 (1985) 230–234.
23. Downie P, Litchfield D, Parsons R, Reynolds DJ, Powis I. High–resolution position–sensing resistive anode microchannel plate detector systems suitable for megahertz count–rates. Meas Sci Technol 4: (1993) 1293.
24. Barrett SD, Image SXM software. http://www.liv.ac.uk/~sdb. Last updated 2017.
25. Hutley MC. Diffraction Gratings (Techniques of Physics), Academic Press, 1982.
26. Collins IR, Laine AD, Andrews PT, Durham PJ. The unoccupied states of tungsten(001) and tungsten(110): theory and experiment. J of Physics: Condensed Matter, 3 (1991) 5307–5321.
27. Noda H, Namioka T, Seya M. Geometric theory of the grating. J Opt Soc Am 64 (1974) 1031–1036.

Hittite Journal of Science and Engineering, 2018, 5 (3) 203-208
ISSN NUMBER: 2148-4171
DOI: 10.17350/HJSE19030000095

Microstructural and Mechanical Characterization of 9Cr-1Mo-1W Weld Metal

Emin Salur[1], Mustafa Acarer[1], Fikret Kabakci[2], Selçuk Keskinkilic[3], Filiz Kumdali Acar[3], Bünyamin Cicek[4]
[1]Selcuk University, Faculty of Technology, Konya/TURKEY esalur@selcuk.edu.tr, macarer@selcuk.edu.tr
[2]Bulent Ecevit University, Alapli Vocational School, Zonguldak/TURKEY fikret.kabakci@beun.edu.tr
[3]Gedik Welding Company, Istanbul/TURKEY, skeskinkilic@gedik.com.tr, facar@gedik.com.tr
[4]Hitit University, Alaca Avni Çelik Vocational School, Çorum/TURKEY, bunyamincicek@hitit.edu.tr

ABSTRACT

This paper presents microstructural and mechanical characterization of E911 weld metal. The types and transformations of the phases and microstructures of all-weld metal have been investigated through scanning electron microscopy, optical microscope, x-ray diffraction analysis. The elemental analysis and mechanical tests of the weld metal was determined by x-ray fluorescence, hardness measurements, and tensile tests respectively. This study will contribute the understanding of microstructural progression, microstructure characterization and mechanical properties of E911 steel after the post-weld heat treatment (PWHT).

Article History:
Received: 2017/08/15
Accepted: 2018/01/03
Online: 2018/04/10

Correspondence to: Bünyamin Çiçek, Hitit University, Alaca Avni Çelik Vocational High School, Çorum, TURKEY
e-mail: bunyamincicek@hitit.edu.tr

Keywords:
E911; Microstructure; Nechanical properties; Weld metal; Cr-Mo steel

INTRODUCTION

A number of studies have been conducted to reduce the use of fossil fuels and gas emissions in power generation industry (thermal and nuclear power plant) [1]. In recent years new material technology has emerged depending on this quest [2]. Cr-Mo steels are widely used at thermal power plant constructions as piping, combustion chamber, and tubing. They are known as heat resistant materials due to high creep strength, as well as their low thermal expansion and high thermal conductivity [3]. They have significantly reduced the thickness of structures thanks to its high strength; it has significantly reduced the thickness of the structures, which in turn reduces weight and the cost of production. However, the lifetimes of these steels are reduced owing to the excess oxidation that occurs when they are exposed to high temperatures for a long time [4]. Therefore, during the few decades, Cr-Mo steels have been developed by alloying with elements such as W, Ni, Nb, V, Ti as a result of extensive studies carried out in some countries with the participation of various project partners In Europe, E911 steel which includes 9% Cr, 1% Mo and 1-2% W was developed by European Creep Collaborative Committee (ECCC) [5]. E911 steel has martensitic microstructure under air cooling after normalizing. Therefore it is used as tempered condition following normalizing.

The work of Wang H. et al. examined microstructural changes and properties of 9Cr-1Mo metals treated at high temperature for long periods and after post-weld heat treatment [6]. Barnes A. and Abson D. investigate possible increase toughness in weld metals W-including. Consequently, they observed that toughness of W-including weld deposit superior to the W-free weld deposits [7]. In the literature, there are a lot of works on P91 and P92 steels and their weld metal [8-16]. However, there are limited studies on characterization of microstructure and mechanical properties of E911 steel and its weld metal [17-18]. Therefore, this paper aims to presents microstructural and mechanical characterization of E911 weld metal.

EXPERIMENTAL PROCEDURE

In this study, all weld metal was produced by stick electrodes (SMAW technic). Stick electrodes were fabricated in Gedik Welding Company in Turkey. The chemical composition of E911 weld metal was determined by Rigaku ZSX Primus-II XRD devi-

ce and it can be seen in Table 1. The base metal size is 20x170x300 mm and welding parameters are given in Table 2. The schematic view of welding producing E911 weld metal shown in Fig. 1. Low carbon steel was also used to support as a backing plate (made of steel) during all welding. Heat input during welding was calculated according to Equation1.

$$\text{Current} * \text{Volt} * 60 * \text{Factor} / \text{cm/min.} / 10.000 = \text{kJ/mm} \quad (1)$$

The all weld metal was heat treated at 760 °C for 4 hours for post weld heat treatment (PWHT) as illustrated in Fig. 2 to AWS 5.5. The metallographic specimen was ground to 2000 mesh and polished with 3 µm diamond paste to observe micro structure of E911 weld metal. Then specimen was etched using 2.5 gr picric acid, 2.5 ml HCl, 100 ml ethanol (Picral) [19]. Nikon MA 100 model optical and Zeiss Evo/LS10 model scanning electron microscopes (SEM) with EDX were used for microstructure analysis. SEM was also used for fracture surface analysis. Thermal analysis (DSC) was carried out to determine critical transformation temperatures (A_1, A_3, M_f, M_s, and T_{curie}).

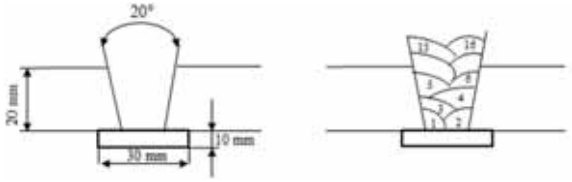

Figure 1. Schematic view of producing E911 weld metal

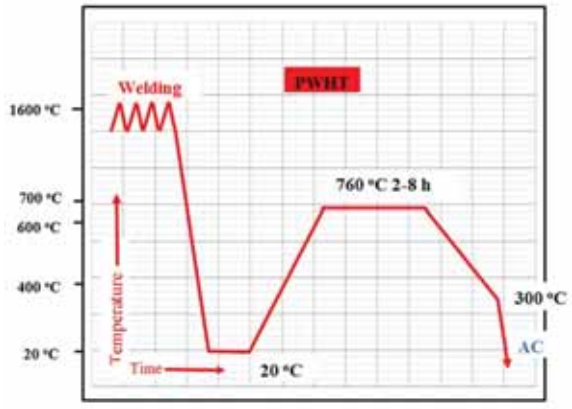

Figure 2. Schematic view of the post weld heat treatment (PWHT) process

Brinell and micro Vickers hardness tests were used to measure hardness of the weld metal by Bulut Digirock-Rbov and Microbul-1000 D models hardness tester devices respectively. Tensile test was performed at room temperature

Table 2. Welding parameters.

Diameter of covered electrode (mm)	*3.20*
Current (A)	*135*
Arc voltage (V)	*33.5*
Welding speed (mm/min)	*125*
Factor Value for SMAW (EN 1011-1)	*0.8*
Welding position (EN 6947)	*PA*
Heat input (kJ/mm)	*1.78*
Pass pieces	*25*
Preheat and inter pass temperature (°C)	*150 , 200*

by Instron 8801 model with 100 kN tester device. Tensile test samples were taken from weld metal to AWS 5.5 specification as showed in Fig. 3 and the samples were prepared according to the ASTM E8/8M-08 standard [20].

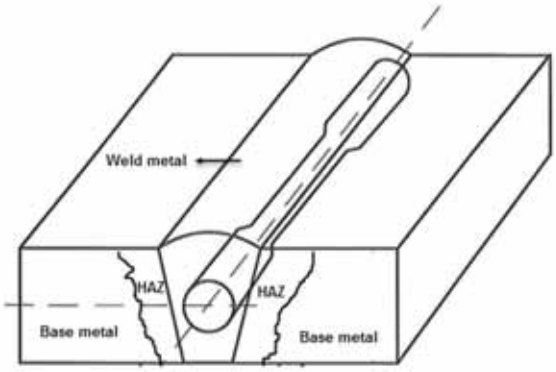

Figure 3. Schematic view of tensile test samples taken from all weld metal

RESULTS AND DISCUSSION

Microstructure Characterization

In this study it was observed that the microstructure of E-911 steel consisted of tempered martensitic with columnar structure. In the literature; it was reported that typical martensitic structure was observed in the form of columnar [21]. In SEM examinations, $Cr_{23}C$, Mo_2C, W_2C and VC were detected inside grain and grain boundary. L. Cipolla et. al. reported that E911 base and weld metal consist of similarity carbides [22].

In the microstructure examination, delta ferrite phase was observed as seen in Fig. 4. Higher amounts of ferrite-forming elements in the structure lead to an increase in chromium equivalent. This situation encourages the formation of delta ferrite in the microstructure.

Chemical composition of E911 weld metal was given

Table 1. Chemical composition of 9Cr-1Mo-1W steel (wt. (%)).

Element	*Si*	*Mn*	*Ni*	*Cr*	*S*	*Mo*	*Co*	*V*	*W*	*Fe*	*C*
	0.22	*0.53*	*0.43*	*8.74*	*0.005*	*0.96*	*0.01*	*0.20*	*0.98*	*Balanced*	*0.07*

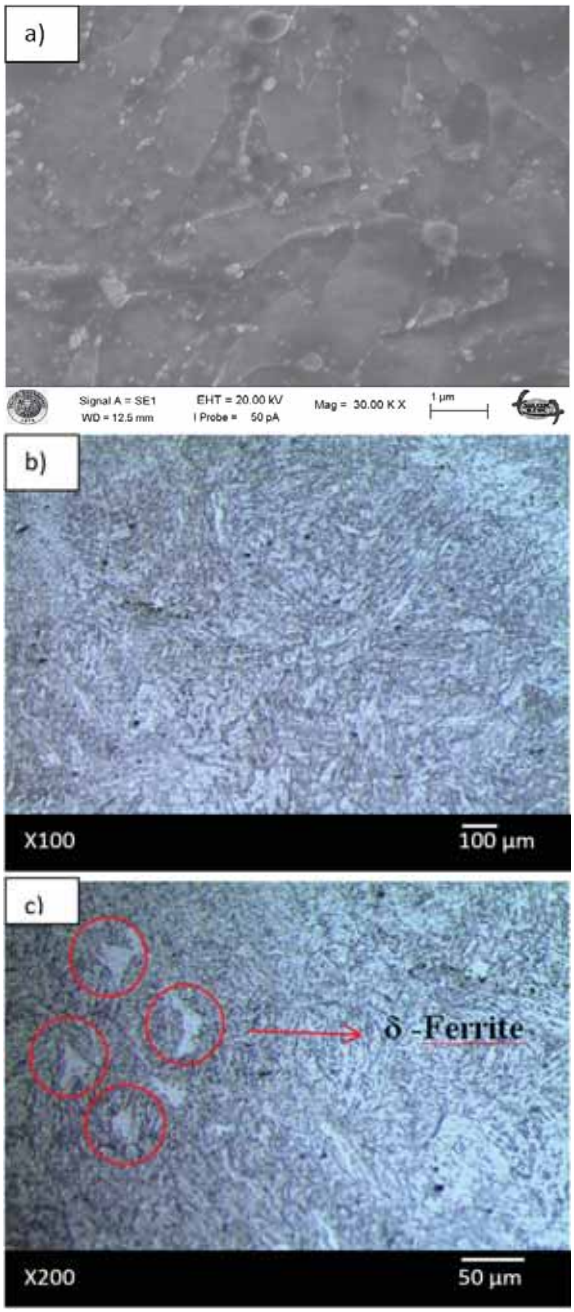

Figure 4. Microstructure of E911 weld metal (a) SEM analysis, low (b) and, high (c) magnification optical microscopy

Table 2 and Creq was calculated as 11.97 (wt %) to Equation 2. When Creq is higher than 9.0 (wt %) delta ferrite can form, which is detrimental effect for toughness and creep strength [23].

$$Creq = (\%Cr) + 6(\%Si) + 4(\%Mo) + 11(\%V) + 5(\%Nb) + 1.5(\%W) + 8(\%Ti) + 12(\%Al) - 4(\%Ni) - 2(\%Co) - 2(\%Mn) - (\%Cu) - 40(\%C) - 30(\%N) \quad (2)$$

Mapping analyses were shown in Fig. 5. Also, line analyze shown in Fig. 6 (b) can be seen as green arrow in Fig. 6 (a). As it can be seen the figures, $Cr_{23}C_6$, Mo_2C, W_2C and VC carbides precipitated along the tempered martensitic lath structure and inside of the grains. In the line analyze shown in Fig. 6 as green arrow, white precipitates can be identified as $M_{23}C_6$ carbides including Fe and Cr (Table 3).

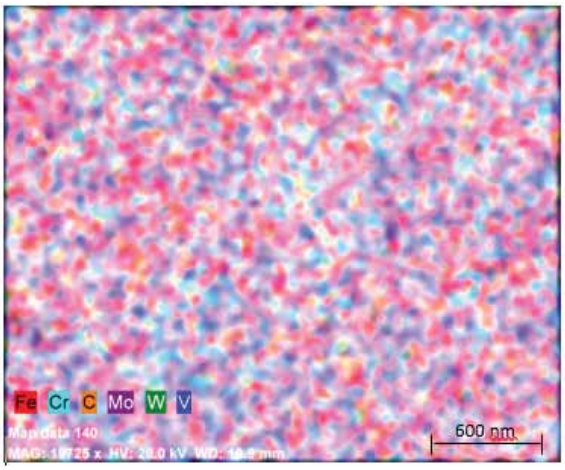

Figure 5. Mapping analyses of E911 weld metal

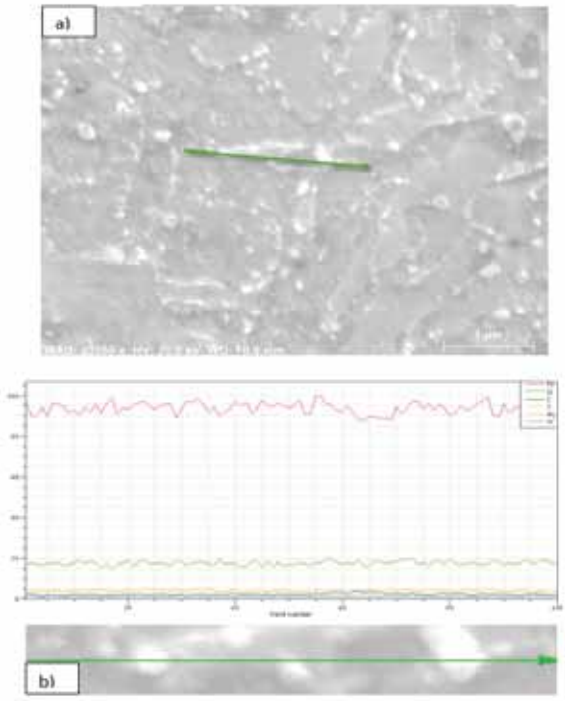

Figure 6. Line analyze from the weld metal (a) line direction (b) high magnification for line

Table 3. Element analysis of the line in Figure 5(b).

Element	*Norm. C (wt %)*
Carbon	*1.40*
Vanadium	*0.29*
Molybdenum	*0.42*
Tungsten	*2.91*
Chromium	*8.92*
Iron	*85.06*
Total	*100.00*

Thermal analyzing (DSC)

According to examined of thermal analysis, in the heating A_{c1}, A_{c3} and Tcurie temperatures are 830, 890, 750 °C respectively and in the cooling Mf temperature is 650 °C, Ms temperature is 690 °C. G. Cumino et. al. in their study evaluated the transformation temperatures A_{c1} and A_{c3} 841, 948 °C respectively [24]. Fig. 7 showed that transformation temperature.

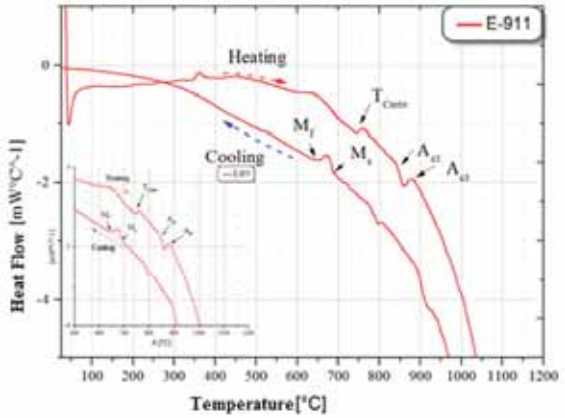

Figure 7. DSC curve of E911 weld metal (20 °C/min- 40mg)

When X-ray analysis was examined, carbides (Cr_7C_3, VC, and $Cr_{23}C_6$) were detected in the microstructure as shown in Fig. 8.

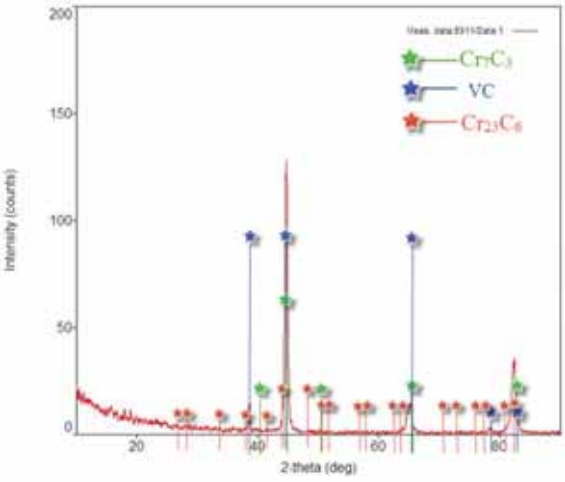

Figure 8. X-ray diffraction analysis of E911 weld metal

Mechanical Properties

The Brinell hardness test was carried out at room temperature and under a load of 187.5 kg. The average Brinell hardness is 230 HB. The micro hardness tests were applied for 20 seconds under 2 kg load. The average micro hardness of δ-ferrite zone in microstructure was determined as 165 HV (~ 164 HB).

Yield strength, tensile strength and elongation were determined as 550 MPa, 712 MPa, and % 18 respectively according to tensile test results at room temperature. Experimental values are reported in Table 4. The studies in the literature [22, 24] and ASTM standard [25] were examined; it was observed that similar mechanical properties were obtained.

Table 4. All-weld metal test results.

Test Temp. °C	*Heat Treatment Temp. °C*	*Yield Str. N/mm2*	*Tensile Str. N/mm2*	*Elongation %*
+20	*760 °C 4 h*	*550*	*712*	*18*

The fracture surfaces of E911 weld metal were given as low and high magnification. In the low magnification as shown in Fig. 9 (a), typical cup and cone fracture zone was observed. In the high magnification dimples can be seen in Fig. 9 (b). Both of the fracture surfaces show E911 weld metal produced in Gedik Welding Company, ductile fracture occurred during tensile test.

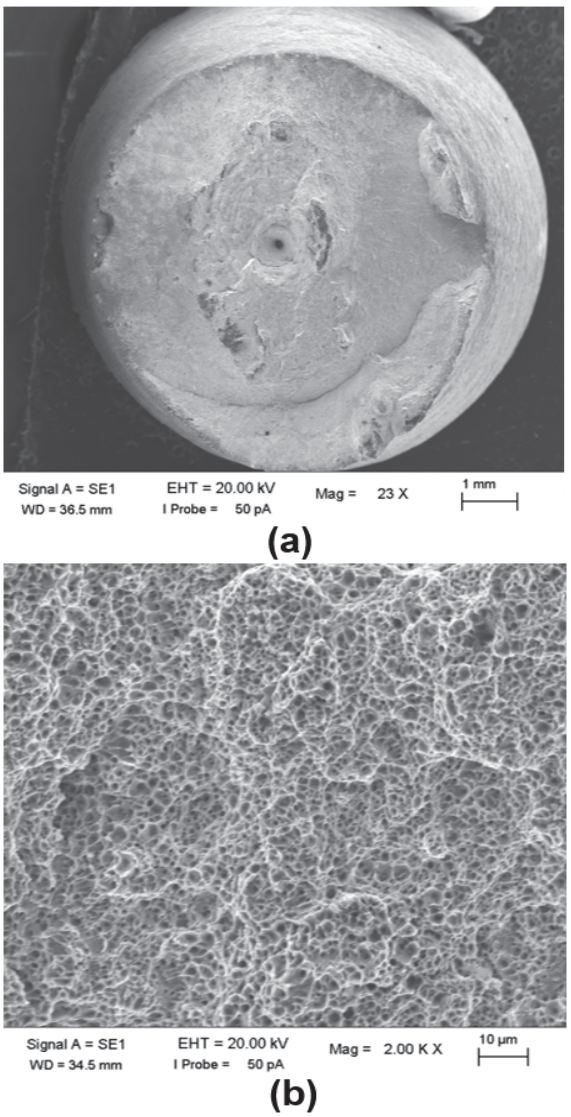

Figure 9. Low (a) - and high (b) magnification SEM fractography of fractured tensile specimens of E911 weld metal

CONCLUSION

In this study, E911 all weld metal was produced with stick electrodes (SMAW). The all weld metal was characterized as microstructure and mechanical properties. Conclusions extracted from the study are listed as below:

a- Microstructure: tempered martensitic was observed into lath boundaries, prior austenite grain boundaries, and delta ferrite phases were observed. Laves phases were not observed.

b- DSC analyses showed that A1 transition temperature is 830°C for the weld metal.

c- After PWHT, VC, $Cr_{23}C_6$ and Cr_7C_3 precipitates were detected by XRD analyse.

d- Mechanical properties of the weld metal are acceptable level according to specifications.

ACKNOWLEDGEMENTS

This work was supported by the Gedik Welding Company. Authors thanks to Gedik Welding Company.

References

1. Guguloth, K., Swaminathan, J., Roy, N., & Ghosh, R. N. Uniaxial creep and stress relaxation behavior of modified 9Cr–1Mo steel. Materials Science and Engineering: A 684,, (2017). 683–696.
2. Viswanathan, R., and W. Bakker. "Materials for ultra supercritical coal power plants–Boiler materials: Part 1." Journal of Materials Engineering and Performance, (2001), 81–95.
3. Chatterjee, A., Chakrabarti, D., Moitra, A., Mitra, R., & Bhaduri, A. K. "Effect of normalization temperatures on ductile-brittle transition temperature of a modified 9Cr-1Mo steel." Materials Science and Engineering: A, 618 (2014), 219–231.
4. Jeshvaghani, R. A., Emami, M., Shafiee, O., & Shahverdi, H. R. Study on formation and characterization of iron aluminide coatings on 9Cr-1Mo steel substrate. Surface and Coatings Technology, 240, (2014), 365–372.
5. Hahn, B., and W. Bendick. "Pipe steels for modern high–output power plants: Part 1 Metalluergical Principles, Long term properties" Vallourec, Boulogne–Billancourt, 2015.
6. Wang, H., Zhang, H., & Li, J. Microstructural evolution of 9Cr-1Mo deposited metal subjected to weld heating. journal of materials processing technology, 209(6), (2009), 2803–2811.
7. Barnes, A., Abson, D., The effect of composition on microstructural development and toughness of weld metals for advanced high temperature 9-13Cr steels. In: Proceedings of the 2nd International Conference on Integrity of High–Temperature Welds, November 10-12, 2003.
8. Nagode, Aleš, Ladislav Kosec, and Boris Ule. "Uni–axial and multi–axial creep behavior of P91–type steel under constant load." Engineering Failure Analysis18.1 61–67, 2011.
9. Ennis, P. J., and A. Czyrska–Filemonowicz. "Recent advances in creep–resistant steels for power plant applications." Sadhana 28.3 (2003): 709–730.
10. Narasimhachary, S. B., and A. Saxena. "Crack growth behavior of 9Cr‡ 1Mo (P91) steel under creep-fatigue conditions." International Journal of Fatigue 56 (2013): 106–113.
11. Panait, C. G., Zieli ska–Lipiec, A., Koziel, T., Czyrska–Filemonowicz, A., Gourgues–Lorenzon, A. F., & Bendick, W. Evolution of dislocation density, size of subgrains and MX–type precipitates in a P91 steel during creep and during thermal ageing at 600 C for more than 100,000 h. Materials Science and Engineering: A, 527(16), (2010), 4062–4069.
12. Fournier, B., Sauzay, M., Caes, C., Noblecourt, M., Mottot, M., Bougalt, A., ; & Pineau. "Creep-fatigue-oxidation interactions in a 9Cr-1Mo martensitic steel. Part III: Lifetime prediction." International Journal of Fatigue30.10 (2008): 1797–1812.
13. Panait, C. G., Bendick, W., Fuchsmann, A., Gourgues–Lorenzon, A. F., & Besson, J. Study of the microstructure of the Grade 91 steel after more than 100,000 h of creep exposure at 600 C. International journal of pressure vessels and piping, 87(6), (2010), 326–335.
14. El–Azim, ME Abd, O. H. Ibrahim, and O. E. El–Desoky. "Long term creep behavior of welded joints of P91 steel at 650 C." Materials Science and Engineering: A 560 (2013): 678–684.
15. Paddea, S., Francis, J.A., Paradowska, A.M., Bouchard, P.J., & Shibli, I.A. "Residual stress distributions in a P91 steel–pipe girth weld before and after post weld heat treatment." Materials Science and Engineering: A 534 (2012): 663–672.
16. Hyde, T. H., M. Saber, and W. Sun. "Testing and modeling of creep crack growth in compact tension specimens from a P91 weld at 650 C." Engineering Fracture Mechanics 77.15 (2010): 2946–2957.
17. Flat, L., Výrostková, A., Homolová, V., & Svoboda, M. "Creep deformation and failure of E911/E911 and P92/P92 similar weld–joints." Engineering Failure Analysis 16.7 (2009): 2114–2120.
18. Sket, F., Dzieciol, K., Borbély, A., Kaysser–Pyzalla, A. R., Maile, K., & Scheck, R. "Microtomographic investigation of damage in E911 steel after long term creep." Materials Science and Engineering: A 528.1 (2010): 103–111.
19. Onoro, J. "Martensite microstructure of 9-12% Cr steels weld metals." Journal of Materials Processing Technology 180.1 (2006): 137–142.
20. ASTM International, Designation: E8/8M–08, Standard practice for tensile testing of metallic materials, Annu. Book ASTM Stand. 64-88, 2009.
21. Výrostková, A., Homolova, V., Pecha, J., & Svoboda, M. "Phase evolution in P92 and E911 weld metals during aging." Materials Science and Engineering: A 480.1 (2008): 289–298.
22. Cipolla, L., Di Gianfrancesco, A., Cumino, G., & Caminada, S. "Long term creep behavior and microstructural evolution of E911 steel." Creep and Fracture in High–Temperature Components: Design and Life Assessment Issues (2005): 288.
23. Patriarca, P., Harkness, S. D., Duke, J. M., & Cooper, L. R. "US advanced materials development program for steam generators." Nuclear Technology 28.3 (1976): 516–536.

24. Cumino, G., Di Cuonzo, S., Di Gianfrancesco, A., & Tassa, O. "Advanced high chromium ferritic steels for boiler components operating at high temperature." Latin American applied research 32.3 (2002): 229–235.

25. Standard Specification for Seamless Ferritic and Austenitic Alloy–Steel Boiler, Superheater, and Heat–Exchanger, Tubes. ASTM Standards 2011, A213/A213 M – 11a.

Hittite Journal of Science and Engineering, 2018, 5 (3) 209-213
ISSN NUMBER: 2148-4171
DOI: 10.17350/HJSE19030000096

The Investigation of Strength and Water Absorption of Self-compacting Concrete by Inclusion of Metakaolin and Calcined Kaolin

Nihat Atmaca[1] **Adem Atmaca**[2] **Gözde Şafak Sezer**[1]
[1] Gaziantep University, Department of Civil Engineering, Gaziantep, Turkey
[2] Gaziantep University, Department of Energy Systems Engineering, Gaziantep, Turkey

ABSTRACT

In this study, commercially available high reactivity Czech metakaolin and calcined impure local kaolin were used for production Self Compacting Concrete (SCC) samples and some hardened properties of these concretes have been investigated. Four types of SCC mixtures were prepared with 0%, 5% and 10% replacement level of Metakaoline and calcined kaolin with including control mixture without any mineral admixtures. Only Portland Cement (PC) was used for production of the control mixture and this mixture was produced with the purpose of comparison. The highest compressive strength value was obtained as 83.5 MPa with 10% replacement level of Metakaolin. The lowest water penetration depth was also calculated as 3.5 mm with 10% replacement level of Metakaolin. The compressive strength and water penetration tests showed that the best strength and durability performance values obtained from mixtures with 10% replacement level of Metakaolin.

Article History:
Received: 2017/11/01
Accepted: 2018/03/02
Online: 2018/04/06

Correspondence to: Nihat Atmaca
Gaziantep University, Department of Civil Engineering, Gaziantep, Turkey
Tel: 0(342) 360 12 00
E-Mail:atmaca@gantep.edu.tr

Keywords:
Self compacting concrete; Czech metakaolin; Calcined kaolin.

INTRODUCTION

Self-Compacting Concrete (SCC) is a special type of high-performance concrete with high fluidity and workability properties due to its lower water to cement ratio which leads to rapid strength development and high durability performances. This special concrete fills the framework without any vibration process and it can be easily placed in the dense reinforcement [1, 2]. Additionally, SCC shows better performances in terms of segregation and bleeding. Nowadays it becomes one of the most popular construction materials [3, 4].

The researchers are focused on fresh and hardened properties of the SCC [5, 6]. Filling ability, passing ability, and segregation resistance are the main fresh properties of SCC. Slump flow test, V-funnel test, J-ring test and Orimet test are used for determination of filling abilities of SCC. For determination of the passing ability of SCC L-box test and J-ring tests are used and for determination of segregation resistance of SCC sieve stability test and penetration test are used [7]. Compressive strength, tensile strength, sorptivity, modulus of elasticity, creep, shrinkage, freeze-thaw resistance, permeability and water absorption are the main hardened properties of SCC. Scientists carried out many experimental studies for determination of these hardened properties [8, 9, 10, 11, 12].

An experimental analysis has been applied to calculate hardened properties of SCCs those contains high-reactive Czech Metakaolin (MK) and commercially available Turkish local Calcined Kaolin (CK) in the present study. The compressive strength and water absorption tests were used to define strength and durability properties of SCC mixtures. The development of strength and durability features of SCCs were observed.

MATERIALS USED IN THE EXPERIMENTS

In the experimental analysis, SCC with MK and CK were produced for determination of the hardened properties of SCC. In addition, the control mixture of SCC with Portland cement has been used to make a comparison.

Metakaolin (MK)

MK is a thermally activated cementitious material obtained by the calcination of kaolinitic clay [13, 14].

Kaolin is quite stable in normal atmospheric conditions. However, kaolin heats up to 650-900 C° during calcination process and it loses approximately 14% of its mass inbound hydroxyl ions and then MK is formed. MK utilized in the experimental analysis was obtained from the Czech Republic. It has a whiteness value (Dr. Lange) of 87 and a specific gravity of about 2.60. Its specific surface area (Nitrogen BET Surface Area) is 18000 cm^2/g. Chemical, physical and mineralogical properties of MK is shown in Table 1.

Calcined Kaolin (CK)

Calcined kaolin (CK) is an another widely used material after 1990's to improve the properties of concrete [15, 16]. CK is used as cement replacement material for improving properties of SCCs at different replacement levels. CK was obtained from a quarry located in Balıkesir province (Sındırgı district – Düvertepe village). This kaolin was subjected to 3 hours calcination process before being used in the experimental study. Chemical, physical and mineralogical properties of calcined impure kaolin (CK) is shown in Table 1.

Table 1. Chemical, physical and mineralogical properties of CK and MK

Type	Compound	CK	MK
Chemical Properties (%)	Cao	2.22	0.5
	SiO_2	69.78	53
	Al_2O_3	24.16	43
	Fe_2O_3	0.69	1.2
	MgO	0.89	0.4
	TiO_2	0.48	0.8
	LOI	0.73	0.4
Phisical Properties	Specific Gravity	2.6	2.6
	Fineness (cm^2/g)	7430*	18000*

*BET (Brunauer–Emmett–Teller) nitrogen adsorption method

Cement

PC 42.5R (CEM I 42.5R) type cement was used for the production of SCCs. It has a specific gravity of 3.13 and Blaine fineness of 3380 cm^2/g. The technical details and chemical composition of the cement are shown in Table 2 and Table 3.

Table 2. Technical details of CEM I 42.5R

Property	Unit	Normative Value	Average Value
Water Demand	%	N/A	28.4-30.0
Initial Setting Time	min	≥ 60	100-180
Compressive Strength (2 days)	MPa	≥ 20	27.5-33.5
Compressive Strength (28 days)	MPa	≥ 42.5, ≥ 62.5	54.0-59.0

Coarse and Fine Aggregate

Coarse and fine aggregates used in the experiments were obtained from a local limestone quarry. The gradation of aggregates is closed to Fuller's curve as shown in Fig. 1. The properties of the fine and coarse aggregates are presented in Table 4.

Table 3. Chemical composition of the CEM I 42.5R

Compound	%
CaO	63.6
SiO_2	19.49
Al_2O_3	4.54
Fe_2O_3	3.38
MgO	2.63
SO_3	2.43
K_2O	0.72
Na_2O	0.22
LOI	2.99

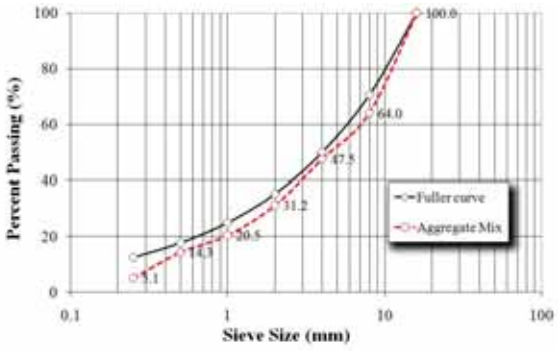

Figure 1. Aggregate grading curves

Table 4. The properties of the fine and coarse aggregates

Property	Fine Aggregate	Coarse Aggregate
Fineness Modulus	3.38	5.68
Specific Gravity	2.45	2.72
Water Absorption (%)	0.95	0.45

Superplasticizer

A high range water reducing admixture (HRWRA) with a specific gravity of 1.07 and pH value of 5.7 was used in the experimental study to get a consistent workability for SCC mixtures. HRWRA is used in the experimental analysis. It is polycarboxylic ether type water reducing admixture commonly used in SCC production.

Mix Proportions

In the present study, SCC mixtures with W/B ratio of 0.35 and binder replacement levels 0%, 5% and 10% were produced. The total binder content was 550 kg for 1 m^3

mixture. Portland cement (PC) and thermally treated kaolins, MK and CK, were utilized in experiments. Control mixtures were produced only with Portland cement. Details of the mixes of SCCs are given in Table 5. The concretes were produced to provide a slump flow diameter of 700±20 mm. These properties were obtained by using HRWRA at different percentages.

When the curing time elongates, above 3 days, the mixing percentages of the same type of MK10 concrete mixture values have better compressive strength performance than MK5 concrete mixture values in all curing periods. CK5 mixtures show better performances for 3 and 7 day curing periods in SCCs. However CK10 mixtures show better strength performances in 28 and 56 day curing periods.

Table 5. Information of the mix proportions of SCCs

Type of Calcined Kaolin	Replacement Level (%)	Mix ID	Cement	Calcined Kaolin	Water	Coarse Aggregate	Sand	HRWRA
None	0	Control	550	0	192.5	790.9	750.6	7.43
MK	5	MK5	522.5	27.5	192.5	787.4	747.2	8.25
	10	MK10	495	55	192.5	783.4	743.5	9.35
CK	5	CK5	522.5	27.5	192.5	787.4	747.2	8.25
	10	CK10	495	55	192.5	783.4	743.5	9.35

EXPERIMENTAL ANALYSIS AND RESULTS

In this study, SCC mixtures with water/binder ratio of 0.35 and binder replacement levels 0%, 5% and 10% were produced. The total binder content was 550 kg for 1 m^3 mixture. The concretes were designed to provide a slump flow diameter of 700±20 mm. This was achieved by using HRWRA at varying amounts.

Compressive Strength

Compressive strength test applied 15x15x15 cm cube specimens according to ASTM C39 / C39M-16b (ASTM, 2016) standard. The test machine has a 3000 kN loading capacity. Cube specimens tested at the ages of 3, 7, 28, and 56 days for determination of compressive strength developments. The age-related compressive strength of the SCCs produced with CK and MK are shown in Table 6 and graphically presented in Fig. 2. It can be clearly observed that the compressive strength values of different mixture types have lower values than the control mix values at the beginning of curing days (3 and 7 days). However, the compressive strength values show an increasing trend after 7 days according to the control mix values. The increase in compressive strength of concrete is due to both microfilling and hydration of mineral admixture with Portlandite (13,14). Control mixtures, SCCs without MK or CK, gain strength by hydration of PC, however MK or CK used SCCs gain strength by both hydration of PC and pozzolanic reactions of MK or CK (14,15).

The highest compressive strength result (83.5 MPa) is achieved with 10% MK after 56 curing days. The second best performance is obtained with 5% MK as 78.4 MPa in 56 curing days.

Table 6. Compressive strength (MPa) of the SCC mixtures

Mixture	Replacement Level (%)	Age (Days)			
		3	7	28	56
Control	0	62.2	65.4	68.6	70.2
MK5	5	60.2	64.1	75.7	78.4
MK10	10	58.7	67.4	78.5	83.5
CK5	5	59.8	65.6	70.6	74.8
CK10	10	53.8	63.9	74.1	77.8

CK incorporating SSCs and control mixtures have lower compressive strength values than MK incorporating SSCs. It is mostly due to the fineness level and reactivity level of MK.

Water Absorption

Water absorption test was applied to SCC specimens according to BS 1881 (Part 122) standard (BS, 1983). The concrete specimens were placed in the drying. After 72 ± 2 hours, specimens were removed from the oven, and then they were allowed to cool at room temperature for

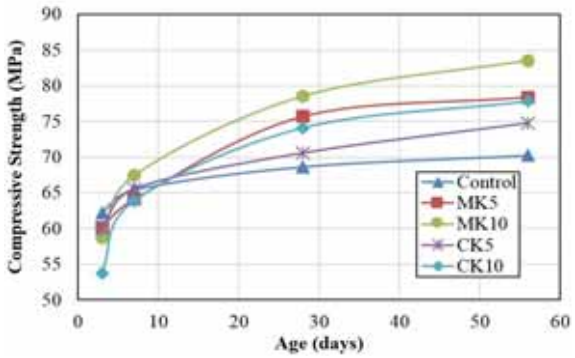

Figure 2. Compressive strength values of SCC mixtures

24 ±0.5 h in the dry airtight vessel. All specimens were weighed and immersed in the water-filled tank for 30 ± 0.5 min. At the end of the specified time, they were removed from the water, dried with a dry towel and weighed again. The results tabulated in Table 7 and visualized in Fig. 3. When the results of all concrete samples are taken into account the 10% MK containing SCCs have the least water absorption values as %2.8 and %1.8 by weight for 28 and 56 days. The water absorption values of MK, CK, and Control SSCs are ranged between 1.8-3.3%, 2-3.5%, and 2.8-3.6%, respectively by weight. 5% CK containing SCC absorbed less water than the control sample with a slight difference for 28 days period; however, it absorbed more water than the control sample for 56 days period. The results of 10% CK, %10MK and %5MK containing SCCs have lower water absorption values in both periods of 28 and 56 days. The lowest values were obtained from the control samples in both curing periods.

Table 7. Water absorption values of SCCs (% by weight)

Mixture	*Replacement Level (%)*	*Age (Days)*	
		28	*56*
Control	*0*	*3.6*	*2.8*
MK5	*5*	*3.3*	*2.5*
MK10	*10*	*2.8*	*1.8*
CK5	*5*	*3.5*	*2.65*
CK10	*10*	*3*	*2*

CONCLUSION

In this experimental study, the effect of high reactivity Czech metakaolin and calcined impure Turkish kaolin on hardened properties of self-compacting concrete is analyzed. The following conclusions might be drawn from the findings.

The compressive strength tests showed that the use of MK and CK increase minimum %5 and maximum %19 of

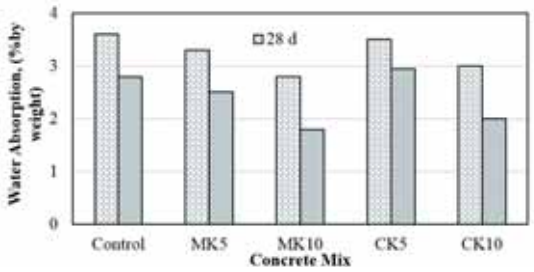

Figure 3. Water absorption values of SCC mixtures

the compressive strength values of SCC. After 3 days curing period the compressive strength values of MK5, MK10, CK5 and CK10 mixes have found lower than the control mixes of SCC. The strength improvements have been observed after 7 days curing period and reached the maximum levels at 56 days. The best strength values for all the SCC mixtures (MK5, MK10, CK5, and CK10) were obtained at the end of the 56 days. %10 MK modified SCCs (MK10) show the highest compressive strength performance as 83.5 MPa (%19 increase). The optimum replacement levels of MK and CK were found as 10% in terms of SCC strength development.

The minimum and maximum water absorption values obtained from %10 MK incorporated concrete as 1.8 % by weight in 56 days curing period. Control SCCs mixes have highest water penetration depths for both 28 and 56 days curing periods. %5 replacement levels of MK and CK in SCC showed lower performance than %10 replacement levels.

ACKNOWLEDGEMENTS

The authors wish to thank Gaziantep University for their constant interest and valuable advice in this project.

REFERENCES

1. Ghezal, A., Khayat, K.H., Optimizing Self–Consolidating Concrete with Limestone Filler by Using Statistical Factorial Design Methods, ACI Materials Journal, (99), 264-272, 2002.
2. Khayat, K.H., Paultre, P., Tremblay, S., Structural Performance and In–Place Properties of SCC Used for Casting Highly Reinforced Columns, ACI Materials Journal (98), 371-378, 2001.
3. Felekoğlu, B., Türkel, S., Baradan, B., Effect of Water/Cement Ratio on the Fresh and Hardened Properties of Self–Compacting Concrete, Build Environment Journal, (42), 1795-1802, 2007.
4. Carro–lópez, D., González–Fonteboa, B., Brito, J., Martínez–Abella, F., González–Taboada, I., Silva, P., Study of the Rheology of Self–Compacting Concrete with Fine Recycled Concrete Aggregates, Construction and Building Materials, (96), 491–501 2015.
5. Kapoor, K., Singh, S.P., Singh, B. Durability of Self–Compacting Concrete Made with Recycled Concrete Aggregates and Mineral Admixtures. Construction and Building Materials, (128), 67–76, 2016.

6. Khayat, K.H., Optimization and Performance of Air–Entrained SCC, ACI Materials Journal, (97), 526–535, 2000.
7. Schutter, G. D., Guidelines for Testing Fresh Self–Compacting Concrete, European Research Project, Growth Contract No. GRD2–2000–30024, 2005.
8. Sab u, M., One , T., Petean, A. I., Hardened Properties of Self–Compacting Concrete, First International Conference for PhD students in Civil Engineering CE–PhD, 4–7 November 2012, Cluj–Napoca, Romania.
9. Barluenga, G., Palomar, I., Puentes, J., Hardened Properties and Microstructure of SCC with Mineral Additions, Construction and Building Materials, (94), 728–736, 2015.
10. Ulubeyli, G.C., Artir, R., Properties of Hardened Concrete Produced by Waste Marble Powder, Procedia, Social and Behavioral Sciences, (195), 2181–2190, 2015.
11. Atmaca, N., Abbas, M.L., Atmaca, A., Effects of nano–silica on the gas permeability, durability and mechanical properties of high–strength lightweight concrete, Construction and Building Materials, (147), 17–26, 2017.
12. Atmaca, N., Atmaca, A., Aljumaili M., Ozcetin A.I., Strength and shrinkage properties of self–compacting concretes incorporating waste PVC dust, The International Journal of Energy & Engineering Sciences (3), 47–57, 2018.
13. Siddique, R., Klaus, J., Influence of Metakaolin on The Properties of Mortar and Concrete: A Review, Applied Clay Science, (43), 392–400, 2009.
14. Mermerdaş, K., Caracterization and Utilization of Calcined Turkish Kaolins for Improving Strength and Durability Aspects of Concrete. Published Ph. D. Thesis, Gaziantep University, Institute of Science and Technology, Gaziantep, 2013.
15. Mallik, A., Barık, A.K., Pal, B., Comparative Studies on Physico–Mechanical Properties of Composite Materials of Low Density Polyethylene and Raw/Calcined Kaolin. Journal of Asian Ceramic Societies, (3), 212–216, 2015.
16. Yuan, Y., Chen, H., Lin, J., Yan, J.Y., Surface Modification of Calcined Kaolin with Toluene Diisocyanate Based on High Energy Ball Milling, Applied Surface Science, (284), 214–221, 2013.

Hittite Journal of Science and Engineering, 2018, 5 (3) 215-218
ISSN NUMBER: 2148-4171
DOI: 10.17350/HJSE19030000097

Characterization of Flocs in Dewatering of Coal Plant Tailings

Can Gungoren[1] Yasin Baktarhan[1], Ilgin Kursun[1], Safak G. Ozkan[1] Orhan Ozdemir[1]
[1] İstanbul University, Department of Minig Engineering, İstanbul, Turkey

ABSTRACT

Flocculation is a widely used method for dewatering fine coal tailings. Flocs must resist to the shear stresses during the following processes such as flotation, cyclone separation, and pumping. Therefore, the strength of the flocs must be considered during flocculation. In this study, the fine coal tailings were dewatered with an anionic flocculant (SNF-923) at various dosages, and the floc size of the coal tailings was characterized using a laser diffraction particle size analyzer with respect to time in order to determine the change in the floc size and hence the floc strength. The results of this study clearly indicated that the determination of the floc size with a laser particle size analyzer could be a simple and good method to observe the flocculation efficiency in terms of the floc strength.

Keywords:
Coal tailings; Flocculation; Floc size; Floc strength; Laser diffraction particle size analyzer

Article History:
Received: 2017/11/07
Accepted: 2018/02/20
Online: 2018/04/06

Correspondence to: Orhan Ozdemir
İstanbul University, Department of Minig Engineering, İstanbul, Turkey
Tel: 0(212) 473 71 80
E-Mail:orhanozdemir@istanbul.edu.tr

INTRODUCTION

Lignite coal, which has a large share in world coal reserves, must be subjected to coal preparation processes in coal washing plants due to its low calorific value and high ash content. After these processes, the huge amount of tailings is produced from the plants, and they must be dewatered before disposal. For this purpose, flocculation is a widely preferred method for solid-liquid separation of fine coal tailings. In this method, long-chain polymers are used to bind particles together to form bigger particles to settle them easier and faster.

Flocculation process is affected by various parameters including solid ratio, pH, temperature, stirring speed and time, molecular weight, chain length, charge and dosage of flocculant. In the flocculation process, flocs with several physical characteristics such as size, structure, and strength are formed depending on these flocculation conditions. Different floc characteristics are preferred for various processes. For example, strong and high-density flocs are favorable in filtration, but not in sedimentation processes. Therefore, it is extremely important to characterize the flocs to optimize the flocculation processes [1-7].

For this reason, there have been various studies on the investigation of floc size, density, structure, and strength [8-13]. Different techniques were used for the floc strength measurements such as image based-techniques [14], computational fluid dynamics (CFD) [15], shear stress [16, 17] sonication/capillary suction time (CST) [18], and light scattering technique [3, 19, 20]. Particularly, floc strength is a very important floc property because flocs are exposed to shear stresses in the flocculation. Therefore, the flocs must resist these stresses in order not to break into smaller pieces [6, 13].

Floc strength is actually dependent upon the strength and number of the inter-particle bonds between the components of the floc. If the stress applied to a floc is larger than the bonding strength within the floc, it will break. Therefore, in this study, SNF-923 was chosen as a typical commercial anionic flocculant to flocculate the coal tailings more effectively. The novelty of the study relies on the fact that this method can be easily used to analyze the floc strength using the anionic collectors such as SNF-923. During the flocculation experiments, the turbidity measurements were also conducted. Furthermore, the size and strength of the flocs were determined with respect to time employing a laser diffraction particle size analyzer.

MATERIAL AND METHODS

The lignite coal tailing samples were taken from a coal processing plant in Soma, Manisa, Turkey. The maximum particle size of the samples was determined as 150 μm with 49.99 μm average size. 70.6% of the sample was under 38 μm.

In the flocculation experiments, the coal tailings were stirred in a glass beaker with 250 mL volume at 200 rpm stirring speed for 10 min using a magnetic stirrer. The experiments were performed at 5% solid-in-pulp ratio and at room temperature (23°C). Then, the suspension was transferred to a graduated cylinder followed by adding flocculant at a specific dosage, and stirred for an additional 1 min at the same speed. The suspension was left for settling, and the settlement distance was recorded at each 1 min for first 10 min and at each 5 min for next 20 min. Meanwhile, the turbidity measurements of the residual solution were performed at the 10th, 20th, and 30th min.

For the floc size and strength measurements, 0.5 g coal tailing in 50 mL distilled water was mixed at 500 rpm with a magnetic stirrer. The flocculant at desired dosage was added into the suspension during the mixing, and the stirring was continued for an extra 2 min. A small amount of the flocs was taken with a wide-diameter pipette (in order not to break the flocs) from the bottom of the beaker to measure the floc size, and added to 1 L water. The suspension was stirred gently again at 800 rpm with an overhead stirrer in order to keep the flocs pending in the suspension during the measurements. An embedded software was used to determine the size distribution of the flocs. In addition, the floc size measurements were carried out at different times for observing the change in the floc size and hence floc strength. The schematic representation of the experimental setup for the floc size measurements is seen in Fig. 1.

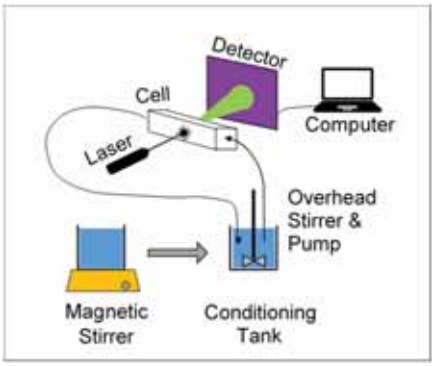

Figure 1. Schematic representation of the experimental setup for the floc size measurements.

RESULTS

In order to investigate the settling behavior of the coal tailings, the flocculation tests were carried out with SNF-923 at different dosages (50, 150, and 300 g/t dosages), and the results are shown in Figure 2. As seen from Fig. 2a, while the change in the height of the sediment bed of the coal tailing showed no change in the absence of flocculant this is because of the electrical repulsion forces between coal particles due to their zeta potentials. With the addition of the flocculant the flocculant molecules begun to form bridges between the coal particles. The results seen in Fig. 2a showed that the coal particles settled more easily and faster in the presence of flocculant. The results presented in Figure 2 also revealed that the particle settling velocity is dependent on the flocculant dosage. For example, the sample treated with the 150 and 300 g/t flocculant dosages achieved a high settling rate compared to that of 50 g/t flocculant dosage. Actually, there was no specific difference between 150 g/t and 300 g/t which indicated that 150 g/t dosage was much enough to settle down of the particles successfully. Even tough the same settling rate was obtained at both dosages, 150 g/t flocculant resulted in clearer water, which indicates that the flocculation mechanism for anionic flocculant incorporates an electrical charge attraction between the flocculant and particles. An excessive flocculant adsorption on the particle surfaces caused repulsion of the particles therefore the turbidity of the suspension increased at 300 g/t.

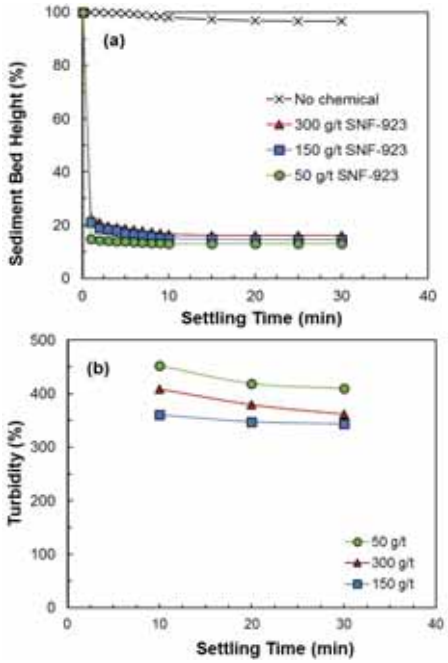

Figure 2. (a) Change in sediment bed height and (b) turbidity of the coal tailings at various flocculant dosages.

As known from literature, flocculation performance depends on floc size distribution and floc structure [21]. For this reason, the size distribution of flocs was determined in the absence and the presence of the flocculant. The size distributions of the flocs produced with 50, 150, and 300 g/t flocculant along with the unflocculated particles are shown in Fig. 3. It is seen from Fig. 3 that the size of the flocs increased with an increase with the flocculant dosage, and the floc size distribution shifted to bigger sizes. It is seen that the size of the flocs formed at 50 g/t flocculant dosage was smaller than the flocs formed at 150 and 300 g/t SNF-923. This is because of the amount of the flocculant molecules

was not enough to bind more coal particles at 50 g/t dosage. However, the change on the size of the flocs formed with 150 and 300 g/t SNF-923 was not much. Therefore, it is understood that the floc sizes could not be increased any more due to some factors such as initial size and surface area of the coal particles, ambient pH, the chemical structure of the flocculant, and the shear stress generated on the flocs during the measurement process even though, the flocculant dosage increased up to 300 g/t. The results along with the previous result clearly indicated that 150 g/t could be chosen as an optimum flocculant dosage for the dewatering of the coal tailings.

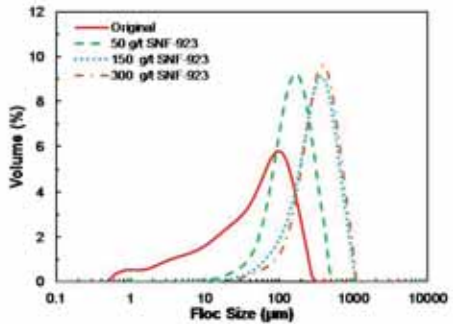

Figure 3. Size distribution of the flocs at various (50, 150, and 300 g/t) SNF-923 dosages at the end of 4 min stirring time.

In general, floc strength increases with floc size [6]. Therefore, it can be said that 150 g/t SNF-923 is the optimum flocculant dosage for the floc stability according to the change in the floc size in time. The size distributions of the flocs as a function of stirring time are shown in Figure 4 which shows the average size (d50), as well as the d90, and d10 size of the flocs produced with the flocculant at different dosages. These results showed that the flocs produced at low flocculant dosage were not enough to produce larger flocs. As seen from Figure 4, as the dosage of flocculant increased, the d90, d50, and d10 of the flocs increased in all cases. The size distributions of the flocs produced with the flocculant show that there was no significant change in floc size at 150 g/t and 300 g/t flocculant dosages due to the static repulsion forces between the coal particles due to the excessive use of flocculant. The increase of the flocculant dosage to 300 g/t did not change the floc strength as well as floc size. Therefore, it can be said that 150 g/t SNF-923 is the optimum flocculant dosage for the floc stability according to the change in the floc size in time.

Fig. 4 also shows that the flocs do not grow continuously as a function of time. On the contrary, they were weak and broken during the measurements Most probably, they reached a steady state size for a specific shear condition. When the shear rate increases above a critical level, flocs will break until a new steady state is reached. Therefore, the aggregation rate is in a balance between the floc formation and floc breakage. Accordingly, the stability of a flocculated

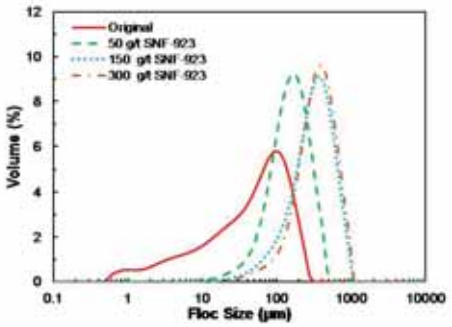

Figure 4. (a) d10 (b) d50 (c) d90 sizes in respect to stirring time at various flocculant dosages.

suspension is dependent upon the breakability of the flocs [22, 23].

CONCLUSION

The results of this study showed that the coal tailings could be flocculated considerably with the use of SNF-923. Although the increase in the flocculant dosage showed considerable effect on the settlement speed, the lowest turbidity values obtained at 150 g/t SNF-923.

As known from literature, flocs can be broken by the shear forces during the dewatering processes. Therefore, the floc strength is crucial for a successful solid-liquid separation. The change in the floc size in time at a given shear stress is an important indicator of the floc strength.

The floc size measurements in respect to time indicated that the floc strength at a constant shear stress depended on the SNF-923 dosage and stirring time. The flocs formed at 50 g/t were finer compared to 150 and 300 g/t SNF-923. According to the stability of the flocs in stirring time 150 g/t SNF-923 seems the optimum flocculant dosage at these conditions.

Overall, the results obtained from this study indicated that it was possible to determine the flocculation efficiency in terms of floc size as well as floc strength. And, this can be considered as a simple and effective method in order to characterize the flocs during the dewatering of the mineral processing tailings.

ACKNOWLEDGEMENTS

This work was supported by Scientific Research Projects Coordination Unit of Istanbul University. Project number 48866.

REFERENCES

1. Johnson, SB, Franks, GV, Scales, PJ, Boger, DV, Healy, TW. Surface chemistry-rheology relationships in concentrated mineral suspensions. International Journal of Mineral Processing, 58 (2000) 267–304.

2. Oner, B. Konya–ilgın komurunun polimerik flokulasyonu.in Mining Engineering Department. 2011. Selcuk University: Konya, Turkey. p. 44.
3. Alam, N, Ozdemir, O, Hampton, MA, Nguyen, AV. Dewatering of coal plant tailings: Flocculation followed by filtration. Fuel, 90 (2011) 26–35.
4. Sabah, E, Erkan, ZE. Interaction mechanism of flocculants with coal waste slurry. Fuel, 85 (2006) 350–359.
5. Parekh, BK. Dewatering of fine coal and refuse slurries–problems and possibilities. Procedia Earth and Planetary Science, 1 (2009) 621–626.
6. Jarvis, P, Jefferson, B, Gregory, J, Parsons, SA. A review of floc strength and breakage. Water Res, 39 (2005) 3121–3137.
7. Gungoren, C, Baktarhan, Y, Kursun, I, Ozkan, SG, Ozdemir, O. Determination of floc size and strength of fine coal tailings using laser diffraction technique, in: (Eds.).International Symposium on Mining and Environment. Paper presented at Bodrum, Turkey, UCTEA, Chamber of Mining Engineers of Turkeypp. 609–616, 2017.
8. Harif, T, Adin, A. Size and structure evolution of kaolin–al(oh)3 flocs in the electroflocculation process: A study using static light scattering. Water Res, 45 (2011) 6195–6206.
9. He, W, Nan, J, Li, H, Li, S. Characteristic analysis on temporal evolution of floc size and structure in low–shear flow. Water Res, 46 (2012) 509–520.
10. Slavik, I, Muller, S, Mokosch, R, Azongbilla, JA, Uhl, W. Impact of shear stress and ph changes on floc size and removal of dissolved organic matter (dom). Water Res, 46 (2012) 6543–6553.
11. Nasser, MS. Characterization of floc size and effective floc density of industrial papermaking suspensions. Separation and Purification Technology, 122 (2014) 495–505.
12. Cao, B, Gao, B, Wang, M, Sun, X, Wang, J. Floc properties of polyaluminum ferric chloride in water treatment: The effect of al/fe molar ratio and basicity. J Colloid Interface Sci, 458 (2015) 247–254.
13. Franks, GV, Yates, PD, Lambert, NWA, Jameson, GJ. Aggregate size and density after shearing, implications for dewatering fine tailings with hydrocyclones. International Journal of Mineral Processing, 77 (2005) 46–52.
14. Wang, B, Shui, Y, He, M, Liu, P. Comparison of flocs characteristics using before and after composite coagulants under different coagulation mechanisms. Biochemical Engineering Journal, 121 (2017) 107–117.
15. Bridgeman, J, Jefferson, B, Parsons, S. Assessing floc strength using cfd to improve organics removal. Chemical Engineering Research and Design, 86 (2008) 941–950.
16. Yuan, Y, Farnood, RR. Strength and breakage of activated sludge flocs. Powder Technology, 199 (2010) 111–119.
17. Hermawan, M, Bushell, GC, Craig, VSJ, Teoh, WY, Amal, R. Floc strength characterization technique. An insight into silica aggregation. Langmuir, 20 (2004) 6450–6457.
18. Hall, T. Sonication for the study of floc strength and reflocculation of activated sludge. Environmental Technology Letters, 2 (1981) 579–588.
19. Sung, S–S, Ju, S–P, Hsu, C, Mujumdar, AS, Lee, D–J. Floc strength evaluation at alternative shearing with presence of natural organic matters. Drying Technology, 26 (2008) 996–1001.
20. Wang, Y, Li, X, Wu, C, Zhao, Y, Gao, BY, Yue, Q. The role of sodium alginate in improving floc size and strength and the subsequent effects on ultrafiltration membrane fouling. Environ Technol, 35 (2014) 10–17.
21. Hogg, R. Flocculation and dewatering. International Journal of Mineral Processing, 58 223–236.
22. Spicer, PT, Pratsinis, SE. Shear–induced flocculation: The evolution of floc structure and the shape of the size distribution at steady state. Water Research, 30 (1996) 1049–1056.
23. Biggs, CA, Lant, PA. Activated sludge flocculation: On–line determination of floc size and the effect of shear. Water Research, 34 (2000) 2542–2550

Hittite Journal of Science and Engineering, 2018, 5 (3) 219-223
ISSN NUMBER: 2148-4171
DOI: 10.17350/HJSE19030000098

Microstructure, Corrosion and Wear Properties of FeCrNiMo Based Coating Produced on AISI 1040 Steel by Using Laser Coating Technique

Serkan Islak **Cihan Ozorak**
Kastamonu University, Department of Metallurgical and Materials Engineering, Kastamonu, TURKEY

ABSTRACT

This study aims to investigate microstructure, hardness, corrosion and wear properties of FeCrNiMo-based coating produced on AISI 1040 steel by using laser welding method. Microstructure properties and phase formation were examined by SEM-EDS and XRD. The hardness measurement was made by using a microhardness device along a line from the upper surface of the coating to the substrate. The wear tests of both the substrate and coating layer were made with a scratch test device. SEM examinations showed that the coating layer had a dendritic microstructure and was uniformly bonded to the substrate. The coating layer was harder than the substrate. According to wear tests, the friction coefficient of the coating layer was lower compared to the substrate. Substrate and coating layer were immersed in an aqueous solution of %3,5 NaCl for potentiodynamic measurements. Corrosion results showed that coating of the AISI 1040 steel with FeCrNiMo increased the corrosion resistance.

Article History:
Received: 2017/11/13
Accepted: 2018/03/29
Online: 2018/04/06

Correspondence to: Serkan Islak
Kastamonu University, Department of Metallurgical and Materials Engineering, Kastamonu, Turkey
Tel: 0(212) 473 71 80
E-Mail:serkan@kastamonu.edu.tr

Keywords:
Laser coating, microstructure, wear, corrosion

INTRODUCTION

The wear and corrosion of machine parts is the leading problem encountered in the industry. Surface coating process is widely used to increase corrosion and wear resistance. Many coating methods are used to improve the properties of the surfaces. Basically, coating methods are classified as welding-based coating methods [1,2], thermal spraying [3] and chemical and physical vapor deposition methods [4,5]. Welding-based surface coating methods generally include plasma-transferred arc, gas tungsten arc, laser beam, submerged, electro-slag and electron beam welding processes [6-8]. Laser coating is a unique process that produces a coating metallurgically bonded to the substrate, which finds an increasing application in surface engineering field. A laser beam having a high energy density is a heat source used to melt the coating material and a limited portion of the substrate. The coating materials are in the form of powder, bar or layer. Compared to other coating techniques, laser coating has many advanced properties. These include a metallurgical bonding between the coating and the substrate, a very fine grained microstructure, a low melt rate and a limited heat-affected zone (HAZ) [9-11]. Due to its high corrosion resistance and high wear resistance, the FeCrNiMo alloy is often used under atmospheric conditions in acidic and tribological environments [12]. In this study, a FeNiCrMo based alloy wire was produced as a coating layer on AISI 1040 steel surface by laser welding. Microstructure, phase formation, corrosion and wear properties of the produced coating were investigated.

EXPERIMENTAL STUDIES

AISI 1040 steel in the dimensions of 20 x 10 x 80 mm was used as the substrate material in the surface coating processes. Prior to the laser coating method, the surface of the steel material was cleaned with acetone. Alloy wires with a 0.6 mm diameter were coated on AISI 1040 steel surface by using an Or-Laser brand laser welding machine with the power of 200 Watts. Table 1 shows the chemical composition of the wire and the substrate used in the coating. Fig. 1 shows the the surface coating process with laser welding. The laser coating process was performed in the form of coating passes.

The samples were taken in the dimensions of 10 mm x 10 mm x 10 mm from the middle zone of the coating material for the microstructure examinations and wear test. Coating materials passed through the

Table 1. Chemical composition of substrate and coating wire (wt.%)

Materials	*Cr*	*Ni*	*Mo*	*Mn*	*Co*	*Si*	*C*	*Fe*
Substrate	-	-	-	*0.85*	-	*0.20*	*0.42*	*Balance*
Coating wire	*18*	*10*	*3*	*2.5*	*1.5*	*1*	*0.1*	*Balance*

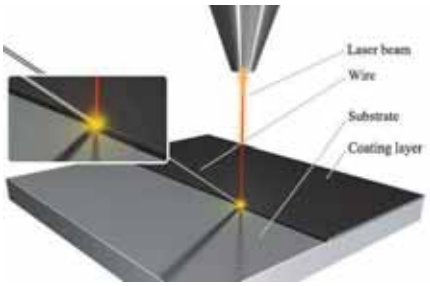

Figure 1. Principle diagram of laser coating process

metallographic processes were etched in 5 ml HNO_3 + 200 ml HCl + 65 g $FeCl_3$ solution for 10 seconds by dipping [13]. SEM-EDS was used for microstructure examinations and XRD was used for phase analysis. The hardness measurement was performed with Future-Tech FM 700 brand micro-hardness device with 200 gr load at 10 sec. waiting period at intervals of 50 μm along a line from the upper surface of the coating to the substrate. Prior to the wear test, the samples were sanded to 1200 mesh sandpaper and their surfaces were polished with a diamond solution and then ultrasonically cleaned. Cleaning was performed with Elma MF3/130KHz device in distilled water for 10 minutes at 35 KHz. Bruker UMT-2-SYS model mechanical test device was used in the wear tests (Fig. 2). The wear was made in the form of micro scratches. A Rockwell indenter was used as the abrasive tip. The scratch size was chosen as 2 mm for all samples. Max 10 N was selected as the load.

Figure 2. Micro scratch wear device

Corrosion measurements were obtained by using a system consisting of a Reference 3000 Potentiostat / Galvanostat / ZRA corrosion system (Fig. 3). Corrosion experiments were carried out after the samples were left waiting for 1 h at room temperature in a 3.5 wt.% NaCl solution (pH 3). A conventional three-electrode cell was used for all the electrochemical measurements. A saturated calomel electrode (SCE) was used as a reference electrode, platinum foil as a counter electrode and coatings as the working electrode. Potentiodynamic sweeping was performed in range of ± 0.25 V and 1 mV/s sweeping rate. The polarization resistance values were calculated by using Stern and Geary equation.

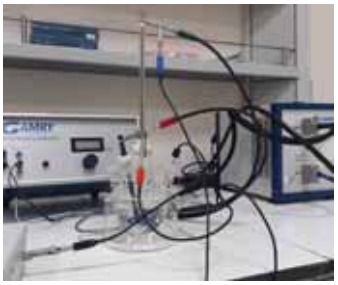

Figure 3. Corrosion system

RESULTS AND DISCUSSION

Fig. 4 shows SEM images of the FeCrNiMo-based coating produced on the AISI 1040 steel surface by the laser welding. The coating thickness was observed to be about 250 μm (Fig. 4a). It is also clearly seen in the same SEM image that the coating layer was composed of overlapped multi-passes. Coating layer formed of cellular structure and dendritic structure. Dendrites occurred in the opposite direction of the heat flow (Fig. 4b). This coating microstructure contained austenite and α-ferrite. Approximate ratio of these structures was determined by means of the Schaeffler diagram in Fig. 4c. These structures formed as solid solutions. No pore or crack formation was found in the coating layer. MAP-EDS analysis was carried out to see how the element distribution in the coating layer is, which is shown in Fig. 5. There was a homogeneous distribution in the coating layer. No oxide formation occurred.

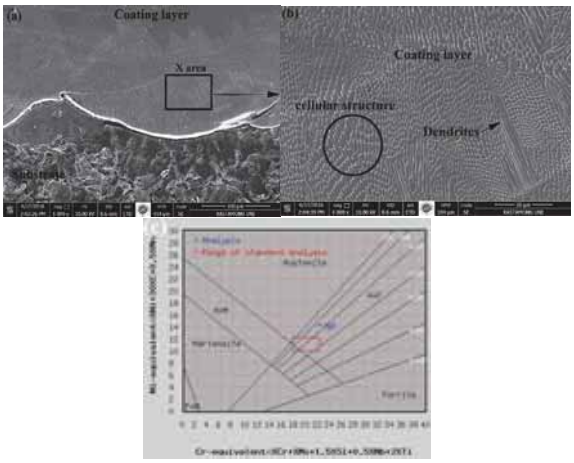

Figure 4. (a) Coating and substrate, (b) coating area (X area) and (c) Schaeffler diagram

Fig. 6 shows the regional EDS analysis of the coating layer. The basic element of the coating layer was iron. The other elements were Cr, Ni, Mo, Mn, and Co. The chemical composition of the coating layer was similar to the chemiv-

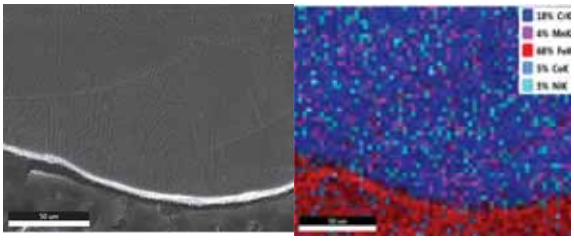

Figure 5. MAP-EDS analysis

cal composition of the selected coating wire. This indicated that the coating process reached its goal. In order to show the elemental difference between the coating layer and substrate, line EDS was performed between the coating and substrate. Fig. 7 shows line EDS. Cr, Ni, and Mn elements increased significantly in the coating layer.

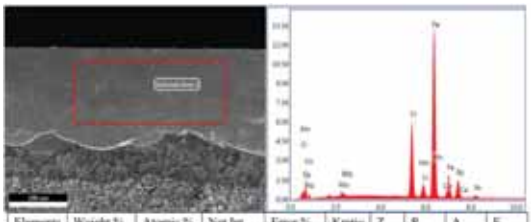

Elements	Weight %	Atomic %	Net Int.	Error %	Kratio	Z	R	A	F
CrK	17.63	19.02	4,112.44	2.65	0.21	1	0.99	0.97	1.22
MnK	2.20	2.25	407.93	5.15	0.02	0.98	0.99	0.98	1.09
FeK	65.88	66.18	10,211.89	1.99	0.63	1	1	0.92	1.04
CoK	1.31	1.25	178.29	11.25	0.01	0.98	1	0.92	1.04
NiK	10.03	9.59	1,128.97	4.27	0.08	1.02	1.01	0.8	1.04
MoK	2.95	1.72	16.42	58.63	0.04	0.87	1.04	0.99	1.45

Figure 6. EDS analysis of the coating layer

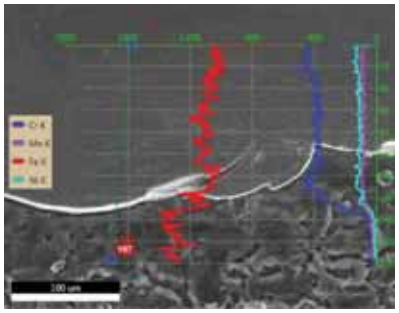

Figure 7. ELine EDS analysis between coating and substrate

Fig. 8 shows the XRD analysis of the coating produced on the AISI 1040 steel surface by the laser welding. The coating layer consisted of α-Fe (ferrite), γ-Fe (austenite) and M23C6 phases. The letter M represents the elements Fe, Cr, and Mo. While austenite peak occurred at the angle of 43.6, 50.6 and 74.7 2θ angles, the ferrite peak occurred at the angles of 64.9 and 81.9 2θ. The intensity of the M23C6 carbide peak was very low compared to the other two phases. The phases occurring in this study are also similar to those in the literature [14]. Since the coating layer had Cr-Ni content, no oxide phase was found. This shows that it is corrosion resistant.

Fig.9 shows the hardness of the coating layer. The microhardness measurement of the coating layer was carried

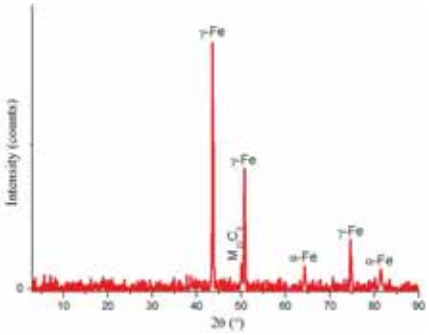

Figure 8. XRD graph of laser coated layer

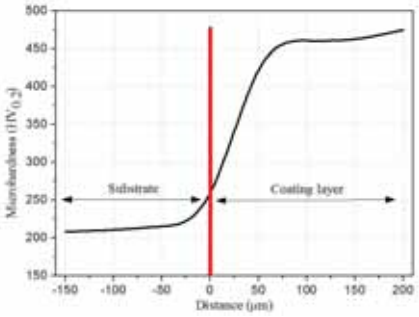

Figure 9. Hardness transition from the coating layer to substrate and the red line transition border

out depending on the distance. There was a significant increase in hardness value of the coating layer compared to the substrate. While the hardness of the substrate was about 210 HV0.2, the hardness of the coating layer was measured as 475 HV0.2. The increase measured was 2 times compared to the substrate. The increase in the hardness of the coating layer was associated with the effect of the mechanism increasing the solid solution strength and the dispersion strengthening of the carbides.

Wear test of the coating layer and the substrate was conducted in the form of micro-scratches. A Rockwell indenter was used as the abrasive indenter. The scratch size was chosen as 2 mm in both samples. Fig. 10 shows wear graphs showing the friction coefficients of the coating layer and substrate. The applied load was measured as 9.55 N, which was maximum. The wear test was completed in 14 seconds. Friction coefficient graphs were also drawn as friction coefficient versus time. When the graph was examined, it was understood that the friction coefficient of the coating layer (~0.17) was lower than the friction coefficient of the substrate (~0.23). This decrease was associated with the solid solution strengthening and the dispersion strengthening of the carbides. Fluctuations were observed in the friction coefficient values of the coating layer. This was related to the fact that the phases were not homogeneously distributed in some regions of the coating. Fig. 11 shows optical images of the wear marks. It was seen that plastic deformation was more intense in the substrate. Flaking was observed in both wear marks. Gong et al [15] presented a study on influence

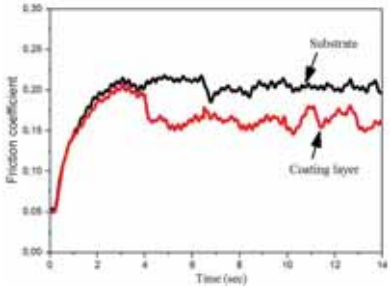

Figure 10. Time-dependent coefficient of friction graph of the samples

of heat treatment on microstructure and mechanical properties of FeCrNi coating produced by laser cladding. The results of the study showed that as the heat treatment temperature increased, the wear resistance decreased although

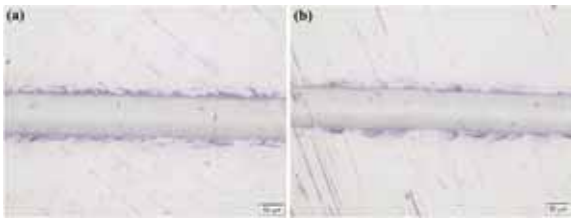

Figure 11. Wear tracks; (a) the substrate and (b) the coating

the maximum tensile strength was obtained.

The potentiodynamic polarization curves of the substrate and coating layer are illustrated in Fig. 12. The corrosion measurement data are summarized in Table 2. Corrosion potential (E_{corr}), anodic and cathodic Tafel slopes (β_a and β_c), corrosion resistance (R_p), corrosion rate and corrosion current (I_{corr}) were found from Tafel curves. Rp was calculated by the Stern and Geary equation [16].

$$Icorr = \frac{\beta_a . \beta_c}{2.303 x R_p \left(\beta_a + \beta_c\right)}$$

where I_{corr} is the corrosion current density in μA cm^{-2}, R_p is the corrosion resistance in kΩ cm^2, and β_a and β_c are the anodic and cathodic Tafel slopes in V or mV, respectively. The corrosion potential (E_{corr}) values of the substrate and coating layer are slightly different. While Ecor of substrate is -435 mV, Ecorr of coating layer is -293 mV. The (R_p of the substrate and coating layer are 20,70 kΩ.cm^2 and 25,57 kΩ.cm^2, respectively. R_p of the coating layer was increased by about 23,4 % compared to that of the substrate. The key element that determines the corrosion resistance of the coating layer is chromium. Cr forms a very thin film on the surface of the material against corrosion attacks. The protective film called passive layer or passive film [17]. The Ni element has a regulatory effect on the ductility and toughness properties of the material. The Mo element provides the continuity of the passive layer formed to protect from corrosion [18, 19]. Qiao et al [20] studied the corrosion behavior of HVOF-sprayed Fe-based alloy coating in various solutions. It has been observed that the coating layer exhibits different corrosion resistances in different solutions. However, it has been reported that the coating layer has higher corrosion resistance than the bottom layer. Our study showed similar results with these results.

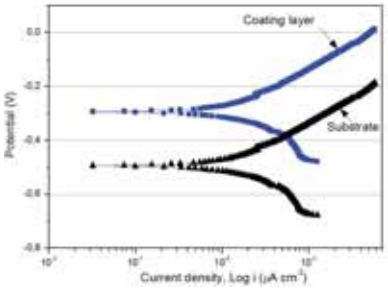

Figure 12. The potentiodynamic polarization curves of substrate and coating layer

Table 2. Electrochemical results of substrate and coating layer

Materials	*E_{cor} (mV)*	*Icor (μAcm⁻²)*	*βa (mV)*	*βc (mV)*	*Corrosion rate (mpy)*	*Rp (kΩ.cm²)*
Substrate	*-435*	*2.35*	*201.8*	*235.2*	*990.2*	*20.70*
Coating wire	*-293*	*2.01*	*235.1*	*238.3*	*945.1*	*25.57*

CONCLUSION

1. In this study, FeCrNiMo based alloy wire was successfully coated on AISI 1040 steel surface with the laser welding technique.
2. It is seen from the SEM images that the coating had dendritic and cell morphology. This shows similarity with the literature. According to the XRD analyses, α-Fe (ferrite), γ-Fe (austenite) and M23C6 phases formed as phases in the structure. It was also found by the Schaeffler diagram that these phases can form. Majority of the structure had an austenite character.
3. The hardness of the coating layer was about two times more than that of the substrate. This increase in the hardness was caused by solid solution and M23C6 carbides formed in the structure.
4. Wear tests of the coating layer and the substrate were made in the form of micro-scratches. A decrease was experienced in the friction coefficient of the coating layer compared to the substrate. This was caused by strength increasing mechanisms.
5. The corrosion potentials of the substrate and coating layer are slightly different. Coating of FeCrNiMo on AISI 1040 steel has increased corrosion resistance by 23,4 %. Cr contributes directly to the corrosion resistance, whereas Mo contributes indirectly.

REFERENCES

1. Deuis RL, Yellup JM, Subramanian C. Metal–matrix composite coatings by PTA surfacing. Composites Science and Technology 58 (1998) 299–309.

2. Gülenç B, Kahraman N. Wear behaviour of bulldozer rollers welded using a submerged arc welding process. Materials & Design 24 (2003) 537–542.
3. Nakajima A, Mawatari T, Yoshida M, Tani K, Nakahira A. Effects of coating thickness and slip ratio on durability of thermally sprayed WC cermet coating in rolling/sliding contact. Wear 241 (2000) 166–173.
4. Knight JC, Page TF. The fine–scale microstructure of thin hard TiN and TiC coatings on steels. Thin Solid Films 193–194 (1990) 431–441.
5. Wolfe DE, Singh J, Narasimhan K. Synthesis of titanium carbide/chromium carbide multilayers by the co–evaporation of multiple ingots by electron beam physical vapor deposition. Surface and Coatings Technology 160 (2002) 206–218.
6. Budinski KG. Hardsurfacing: an overview of the process. Welding Design & Fabrication, July (1986) 51–57.
7. Buytoz S., Orhan A., Gur A.K., Caligulu U. Microstructural Development of Fe-Cr-C and B4C Powder Alloy Coating on Stainless Steel by Plasma–Transferred Arc Weld Surfacing. Arabian Journal for Science and Engineering. 38(8) (2013) 2197–2204.
8. Wu W, Hwu LY, Lin DY, Lee JL. The Relationship between alloying elements and retained austenite in martensitic stainless–steel welds. Scripta Materialia 42 (2000) 1071–1076.
9. Pei YT, Zuo TC. Gradient microstructure in laser clad TiC–reinforced Ni–alloy composite coating. Materials Science and Engineering A 241 (1998) 259–263.
10. Yang S, Liu WJ, Zhong ML, Wang ZJ. TiC reinforced composite coating produced by powder feding laser cladding. Mater. Lett. 58 (2004) 2958–2962.
11. Anandkumar R, Almeida A, Colaço R, Vilar R, Ocelik V, De Hosson JThM. Microstructure and wear studies of laser clad Al–Si/SiC(p) composite coatings. Surface & Coatings Technology 201 (2007) 9497–9505.
12. Ratajski T, Kalemba–Rec I, Dubiel B. Manufacturing, Microstructure and Corrosion Resistance of Electrophoretically Deposited SiO2 and Ni/SiO2 Coatings on X2CrNiMo17-12-2 Steel. Archives of Metallurgy and Materials. 61(2) (2016) 1221-1227.
13. ASTM E407–07. "Standard Practice for Microetching Metals and Alloys." (2015): 1–4.
14. Sun SD, Fabijanic D, Ghaderi A, Leary M, Toton J, Sun S, Brandt M, Easton M. Microstructure and hardness characterization of laser coatings produced with a mixture of AISI 420 stainless steel and Fe–C–Cr–Nb–B–Mo steel alloy powders, Surface and Coatings Technology, 296 (2016) 76–87.
15. Gong, Fu–bao, et al. Influence of heat treatment on microstructure and mechanical properties of FeCrNi coating produced by laser cladding. Transactions of Nonferrous Metals Society of China 26.8 (2016): 2117–2125.
16. Stern M, Geary AL. Electrochemical Polarization I. A Theoretical Analysis of the Shape of Polarization Curves. Journal of The Electrochemical Society 104 (1957) 56.
17. George G, Shaikh H. Introduction to Austenitic Stainless Steels, Corrosion of Austenitic Stainless Steels. Mechanism, Mitigation and Monitoring, edited by: H. S. Khatak, B. Raj, Woodhead Publishing House, Cambridge, UK, (2002).
18. Sedriks AJ, Corrosion of Stainless Steels, Wiley, New York, NY, USA, 2nd edition, (1996).
19. Porcayo–Calderon J, Casales–Diaz M, Salinas–Bravo VM, Martinez–Gomez L. Corrosion Performance of Fe–Cr–Ni Alloys in Artificial Saliva and Mouthwash Solution. Bioinorganic Chemistry and Applications 2015 (2015) 1–14.
20. Qiao L., Wu Y., Hong S., Qin Y., Shi W., Li G. Corrosion Behavior of HVOF–Sprayed Fe–Based Alloy Coating in Various Solutions. Journal of Materials Engineering and Performance, 26(8) (2017) 3813–3820.

Hittite Journal of Science and Engineering, 2018, 5(3) 225-230
ISSN NUMBER: 2148-4171
DOI: 10.17350/HJSE19030000099

Preparation of Molecular Sentinel Based SERS Sensor for Hepatitis C Virus

Adem Zengin
Van Yuzuncu Yil University, Department of Chemical Engineering, Van, TURKEY

ABSTRACT

Construction of a rapid, cost-effective and label free biosensor is important issue for public health. In this study, it has been developed a sensitive, selective and simple biosensor for the detection of hepatitis C virus (HCV) DNA. For this purpose, firstly, superparamagnetic gold nanoparticles were prepared by simple citrate reduction method and used as surface enhanced Raman spectroscopy (SERS) substrate. Then, Raman labelled hairpin DNA (molecular sentinel, MS) was covalently bound on the gold shell by means of gold-sulfur interaction. After addition the complementary DNA (target HCV DNA), the hairpin structure was changed closed state (stem-loop configuration) to open state (hybridization configuration). As a result, the Raman label was located far away from the surface and reduced the SERS intensity. A good relationship was obtained between the decreasing of the SERS intensity and the target DNA concentration (0-50 pM) and the limit of detection was found to be 0.1 pM. The sensing method only consists of a single hybridization and washing procedure after hybridization and centrifuge step can be omitted. It is believed that the prepared biosensor could be a powerful diagnostic tool for HCV detection.

Keywords:
Magnetic gold nanoparticles, Molecular sentinel and surface enhanced Raman spectroscopy.

Article History:
Received: 2017/10/10
Accepted: 2017/12/03
Online: 2017/12/22

Correspondence to: Adem Zengin,
Van Yuzuncu Yil University, Department of Chemical Engineering, Tuşba, Van, Turkey.
Tel: +90 (432) 225-1726
Fax:+90 (432) 225-1730
E-Mail: ademzengin@yyu.edu.tr

INTRODUCTION

Hepatitis C is among the smallest known viruses and it can lead to severe consequences that can go as far as carcinoma and liver cancer [1]. Hepatitis C virus (HCV) is usually transmitted to human through blood and sexual intercourse. Hepatitis C can develop in two ways: acutely or chronically. Acute Hepatitis C is a short-term illness that lasts about 6 months after infection. However, in the majority of patients (75-85%) acute hepatitis C infection becomes chronic which is a life-long disease and can lead to serious health problems (cirrhosis, liver cancer) and even death [2]. Hepatitis C usually does not have symptoms and can therefore be fatal. So, it is very important to detect HCV in early stage of infection to prevent serious health problems. Nowadays, enzyme-linked immunosorbent assay (ELISA) is frequently used for HCV detection [3]. Despite highly selective and specific measurements are carried out with this method, there are serious disadvantages such as not being able to determine in the early stages of the disease and not getting the accurate results in human immunodeficiency (HIV) infected patients. Moreover, several conventional analytical methods were developed for detection of HCV such as electrochemical [4], chemiluminescence [5], piezoelectric sensor [6], etc. Most of the aforementioned methods are often time consuming, require large amount of solvent, complicated operation and expensive equipment although HCV can be detected at low concentrations by those methods.

Surface enhanced Raman spectroscopy (SERS) is a type of Raman spectroscopy which generates enhanced Raman scattering from an analyte molecule that was adsorbed on metal surfaces. The scattering intensity increases depending on the analyte type, analyte position on metal surface, distance between analyte and metal surface and metal type [7]. Thanks to the careful selection of metal and analyte molecules, the SERS mechanism allows the determination of the analyte molecule at considerably lower concentrations as compared with other spectroscopic methods. In the SERS studies, gold is the most studied metal as a SERS

active substrate due to the high motion ability of the outer shell electrons which interact with SERS laser to induce an additional electromagnetic field called surface plasmon that is the main responsible for the enhanced Raman scattering [8-10]. Therefore, taking into consideration advantages of the SERS, it is a good candidate for highly sensitive, selective, and less time consuming detection method for any interested analyte such as DNA, RNA, protein, etc.

Molecular sentinel (MS) is a technique that uses a SERS active substrate and stem loop structure DNA or RNA. In this method, DNA structure is consisting of a thiol group at one end and a Raman label at the other end. DNA is immobilized on the metal surface via thiol-sulfur interaction and the Raman label molecules was located at proximity of the metal surface after immobilization. The stem loop configuration is disturbed by the complementary DNA/RNA and the Raman label is moved from the metal surface which induce the decreasing of the Raman scattering [11,12]. Thus, it is possible to correlate the concentration of the target DNA/RNA and the decreasing of the SERS intensity.

In the present study, a novel MS based SERS sensor was designed for detection of HCV DNA. For this purpose, magnetic gold nanoparticles were synthesized and then, functionalized with stem loop structure HCV DNA. After hybridization, the decreasing of Raman intensity was monitored by SERS. For all the detection steps, only one hybridization process was done and centrifugal separation and post-hybridization washing steps were omitted due to simple magnetic separation of the particles by an external magnet and monitoring only Raman label molecule, respectively. It is believed that the prepared sensor offers sensitive, selective, fast and reliable detection of HCV DNA.

MATERIALS and METHODS

All chemicals used this study were supplied from Sigma-Aldrich (Germany) and used as received unless otherwise stated. Stem-loop hairpin (MS), complementary (target) and non-complementary DNAs were purchased from Daejeon, Korea. The sequences were listed in Table 1. The underlined sequences shows the complementary arms of the stem-loop DNA, and the bold sequences indicates the complementary DNA to the loop region of the MS hairpin. Ultrapure deionized water was used in all experimental studies.

Synthesis of magnetic gold nanoparticles (Fe_3O_4@Au)

Fe_3O_4 nanoparticles were synthesized by co-precipitation method as reported previously [13]. The prepared magnetic nanoparticles were dispersed in 0.1% wt of sodium citrate solution to prevent agglomeration of the magnetic nanoparticles. 500 µL of the magnetic suspension was added to the 100 mL of deionized water and the nanoparticles were well dispersed by an ultrasonic bath at room temperature. The black suspension was heated to 80 °C and stirred with mechanical stirrer at 900 rpm for 1 hour and then, 50 µL 10 mM of $HAuCl_4$ was added to the suspension. The hot plate was removed after the color of the suspension turned to red. After cooling to room temperature, nanoparticles was collected by an external magnet and washed with deionized water for several times and re-dispersed in deionized water. The red suspension was stored at +4 °C until needed.

Preparation of MS probe (Fe_3O_4@Au@MS)

10 mg of the Fe_3O_4@Au nanoparticles were dispersed in 4 mL of 0.01 M phosphate buffer saline containing 200 µM $MgCl_2$ (PBS, pH 7.4) (for the optimization of the salt concentration, please see Supplementary Material) by ultrasonication for 10 min at room temperature and 1 mL of 1.0 µM thiolated stem-loop DNA (MS) solution (0.01M PBS, pH 7.4) was added to the particle dispersion and left to react on a shaker for 2 hours. Then, the nanoparticles was collected by a magnet and washed three times with PBS to remove physically adsorbed MS on magnetic gold nanoparticles and redispersed in 5.0 mL of PBS buffer. The unoccupied gold surface by MS probe was passivated with 2-mercaptoethanol (ME) to reduce non-specific binding of HCV DNA on the gold surface. For this purpose, 1.0 mL of 1 mM ethanolic solution of ME was added to the PBS buffer containing MS probe and left to react on a shaker for overnight. The passivated MS probe was collected by an external magnet and washed again with PBS buffer for three times and lastly redispersed in 5.0 mL of PBS buffer.

Hybridization with target HCV DNA

50 µL of the MS probe and 20 µL of the target HCV DNA sample with a concentration range 0-50 pM in 0.01 M PBS containing 200 µM $MgCl_2$ were mixed and maintained on a shaker at 37 °C. After 15 min. incubation

Table 1. DNA sequences used in the present study.

Name	*Sequence*
Stem-loop DNA (MS, capture probe)	*5´-SH-AAAAACACAUCTGCCGCGGA TATTAGGATGTGTG-R6G-3´*
Complementary DNA (target DNA or HCV DNA)	*3´-ACG GCG CCT ATA ATC CTA -5´*
Non-complementary DNA	*5´-TAGAGGAACGAGGTACCAGCGACG-3´*

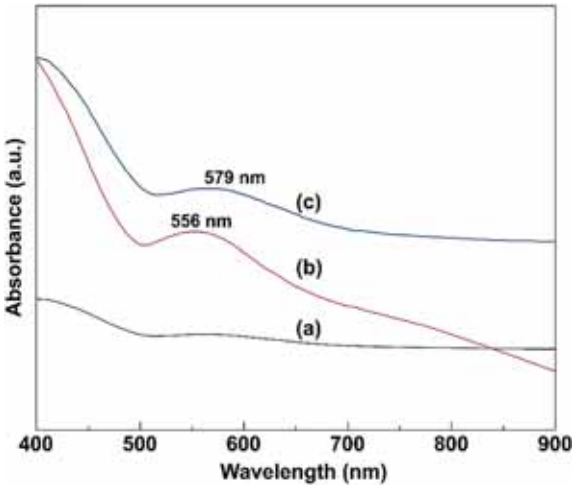

Figure 1. UV-vis spectra of (a) Fe_3O_4, (b) Fe_3O_4@Au, (c) Fe_3O_4@Au@MS

time, the magnetic nanoparticles were collected and redispersed in PBS buffer. Then, 25 µL of the dispersion was dropped on the freshly cleaned silicon surface for SERS measurements. The same protocol was applied for non-complementary DNA.

Optical properties of the prepared nanoparticles were examined by UV-vis spectrophotometer (Shimadzu UV-2550) at room temperature. The morphology and diameter of the nanoparticles were determined by transmission electron microscopy (TEM, JEOL 1400). The mean diameter of the nanoparticles was calculated by using ImageJ software. X-ray photoelectron spectroscopy (XPS) analysis was examined by a SPECS XPS spectrometer using Al Kα as a X-ray source. Magnetic properties of the nanoparticles were characterized by vibrating sample magnetometer (VSM) from Cryogenic Limited PPMS system. DeltaNu Examiner Raman microscope (DeltaNu Inc., Laramie, WY) with a 785-nm laser source was used for SERS analysis. All spectra were collected with 140-mW laser power, for 5-s acquisition time. Baseline correction was done for all spectra.

RESULTS and DISCUSSION

Characterization of Fe_3O_4@Au and Fe_3O_4@Au@MS

The optical properties of the prepared nanoparticles were investigated by UV-vis absorption spectroscopy. After coating of gold shell on the Fe_3O_4 nanoparticles, a new absorption peak at about 556 nm was obtained (Fig. 1b) that is the characteristic absorbance peak of the gold nanoparticle. After immobilization of the MS probe on gold shell, a 21 nm a red shift of the absorption wavelength from 556 nm to 579 nm as a result of the changing of the refractive index of the nanoparticle by surrounding media (Fig. 1c). Moreover, the absorption peaks for both Fe_3O_4@Au and Fe_3O_4@Au@MS were relatively narrow indicating the nanoparticles did not agglomerate in the solution [14].

The mean diameter and morphology of the nanoparticles were determined by TEM analysis and TEM images were presented in Fig. 2. The Fe_3O_4 nanoparticles (Fig. 2a) have an irregular structures with a mean diameter approximately 6.1 ± 1.8 nm (accounted on 185 nanoparticles). After the formation of gold shell on the Fe_3O_4 nanoparticles, mean diameter of the nanoparticle increased to 14.4 ± 3.1 nm (accounted on 228 nanoparticles) indicating the formation of nearly 4.0 nm gold shell on the Fe_3O_4 nanoparticles. After the formation of gold shell, the MS probe was attached on the Fe_3O_4@Au nanoparticles and the diameter of the nanoparticles increased to 20.5 ± 3.8 nm (accounted on 169 nanoparticles). The nearly 6 nm difference between Fe_3O_4@Au and Fe_3O_4@Au@MS nanoparticles was due to the presence of the 33-base DNA on the magnetic gold nanoparticles. As seen from Fig. 2, all nanoparticles were agglomerated after drying on the TEM grids. This was probably due to high magnetization properties of the nanoparticles in solid state [13].

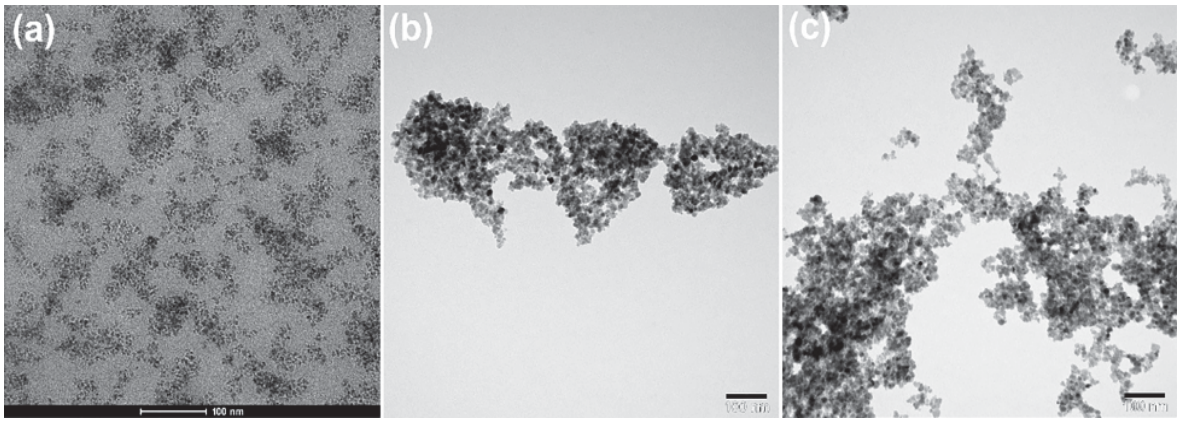

Figure 2. TEM images of (a) Fe_3O_4, (b) Fe_3O_4@Au, (c) Fe_3O_4@Au@MS.

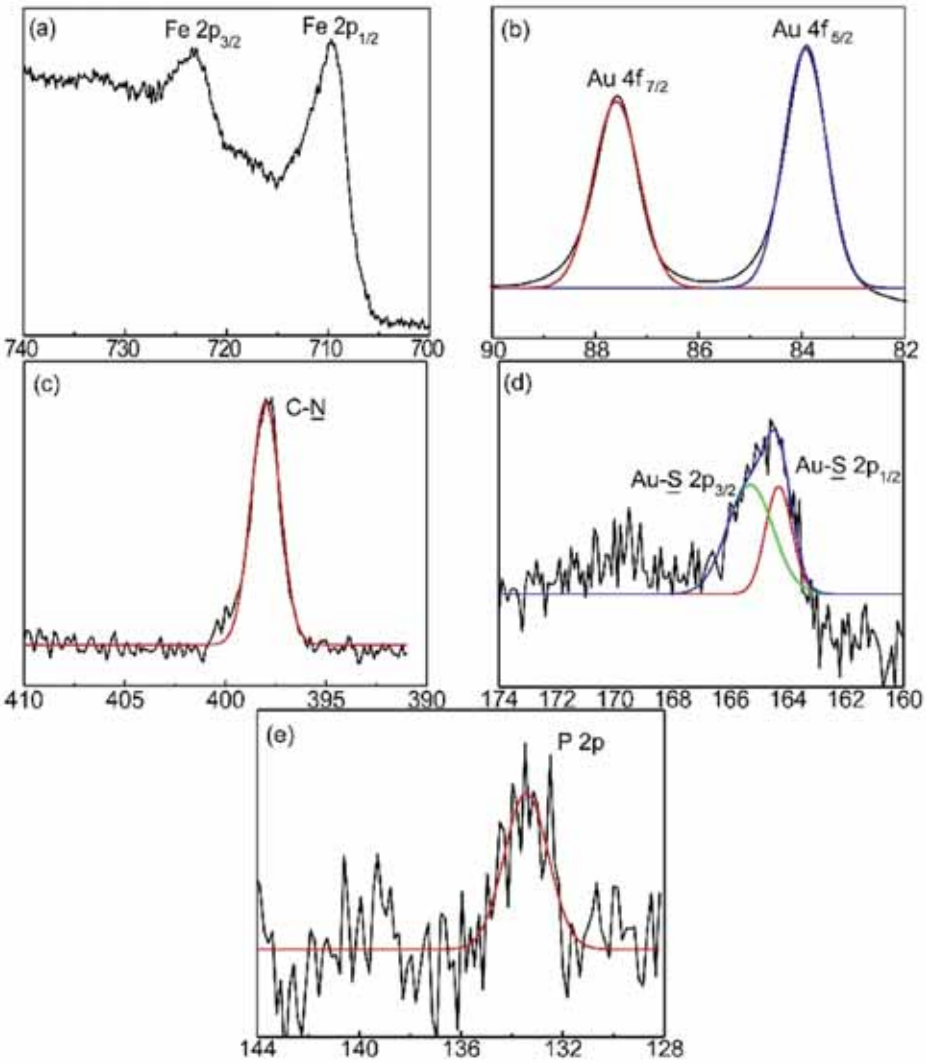

Figure 3. Core-level XPS spectra of (a) Fe2p, (b) Au4f, (c) N1s, (d) S2p, (e) P2p for Fe_3O_4@Au@MS.

Immobilization of the MS probe on the magnetic gold nanoparticles was confirmed with XPS. Core-level XPS spectra of the Fe_3O_4@Au@MS were shown in Figure 3. The core-level XPS spectrum of Fe2p was fitted to two component at about 723.1 eV and 709.5 eV belonging to $Fe2p_{3/2}$ and $Fe2p_{1/2}$, respectively (Fig. 3a). The core level XPS spectra of Au4f was fitted to two different peaks at about 87.4 eV and 83.7 eV corresponding to $Au4f_{7/2}$ and $Au4f_{5/2}$, respectively (Fig. 3b). Moreover, the core-level XPS spectra of N1s, S2p and P2p was fitted to the components with binding energies at about 398.9 eV (C-N) for N 1s (Fig. 3c), 165.0 eV (Au-S$2p_{3/2}$) and 164.2 eV (Au-S$2p_{1/2}$) for S2p (Fig. 3d) and 133.2 eV for P2p (Fig. 3e). The presence of N, P and S elements in the core-level spectra of Fe_3O_4@Au@MS strongly indicated that the covalent attachment of MS probe on the Fe_3O_4@Au nanoparticle were successful.

The saturation magnetization (M_s) values of the all nanoparticles were determined with VSM at room temperature. The magnetic hysteresis curves of the nanoparticles were presented in Figure 4. The M_s value of the Fe_3O_4 nanoparticles was found to be 62.8 emu/g (Fig. 4a). After the M_s of the Fe_3O_4 nanoparticles drastically decreased to 36.8 emu/g due to the formation of Au shell on the Fe_3O_4 nanoparticles (Fig. 4b). The covalent attachment of the MS probe on the Fe_3O_4@Au nanoparticles, the M_s value of the magnetic nanoparticles slightly decreased to 29.5 emu/g (Fig. 4c) that is the sufficient M_s value for using magnetic nanoparticles in biological applications [15,16]. Moreover, in all cases, the magnetic hysteresis curves also showed no remanence or coercivity indicating that all the prepared magnetic nanoparticles had superparamagnetic behavior at room temperature.

SERS detection of the target DNA

SERS detection of the target DNA step was shown in Fig. 5. After immobilization of the MS probe DNA on the Fe_3O_4@Au nanoparticles, the rhodamine 6G (R6G)

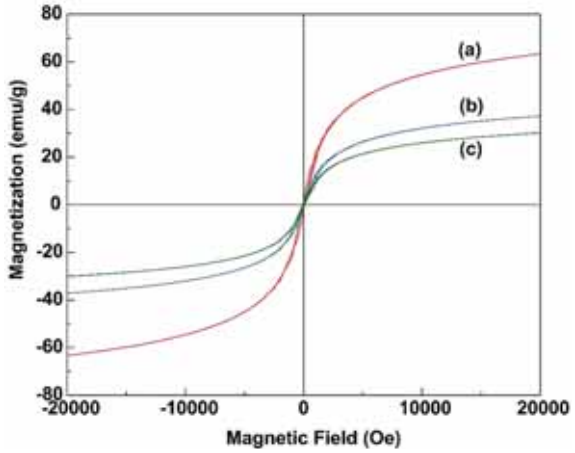

Figure 4. Magnetic hysteresis curves of (a) Fe_3O_4, (b) Fe_3O_4@Au, (c) Fe_3O_4@Au@MS nanoparticles at room temperature.

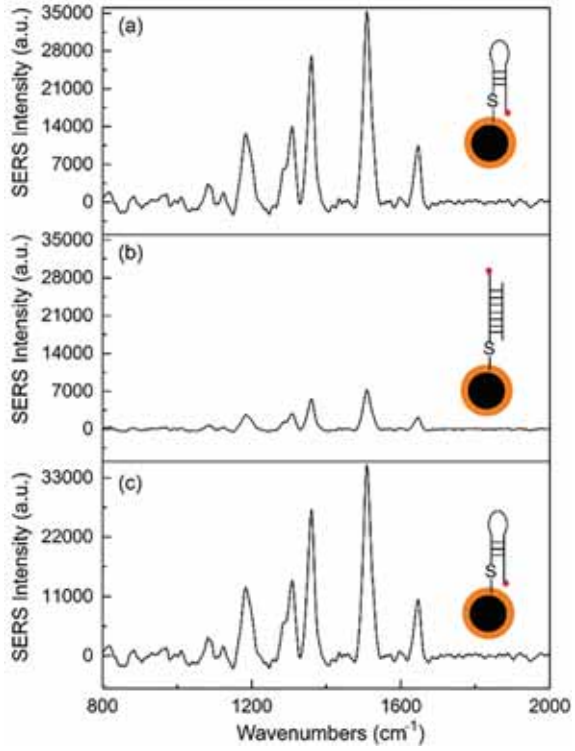

Figure 5. SERS spectrum of (a) Fe_3O_4@Au@MS (blank), (b) Fe_3O_4@Au@MS in the presence of target HCV DNA (concentration: 40 pM), (c) Fe_3O_4@Au@MS in the presence of non-complementary HCV DNA.

label on the 3´-end of the MS probe was located to the Au shell and resulted a strong SERS signal (Fig. 5a). When the complementary DNA was added to the Fe_3O_4@Au@MS nanoparticles, the hybridization took place and the stem-loop structure was opened and R6G was located far away from the Au shell and induced a decreasing SERS intensity (Fig. 5b). Moreover, in the presence of the non-complementary DNA, there was no change in the SERS intensity indicating no hybridization took place and the R6G was still remained close to the Au shell (Fig. 5c). This result also showed the selectivity of the prepared MS based SERS sensor.

It was further investigated to verify the usability of the Fe_3O_4@Au@MS nanoparticles for quantitative DNA detection for the HCV. For this purpose, the Fe_3O_4@Au@MS nanoparticles were incubated with different HCV target DNA with concentration between 0-50 pM and four different measurements were taken for per sample and averaged in a single spectrum. Fig. 6a illustrated the SERS spectra of the MS probe with different amount of target HCV DNA. The SERS intensity decreased when the target DNA concentration increased. This results also suggested that there could be a linear relationship between the decreasing of the SERS intensity and the target DNA concentration. To determine the limit of detection (LOD), the most intensive Raman peak of R6G located at 1506 cm^{-1} was selected. As shown in Fig. 6b, a linear relationship with a correlation coefficient (R^2) of 0.9986 was obtained and the LOD was found to be 0.1 pM from $3S_{blank}/m$ where S_{blank} is the standard deviation of the blank (i.e.in the absence of target HCV DNA) and m is the slope of the calibration curve. Compared with the other HCV DNA detection methods, the developed MS based SERS sensor could provide a higher sensitivity [4, 17-19]. In addition, the lower LOD shows that the prepared sensor can be a powerful diagnostic tool for the detection of HCV in the early stage of infection.

CONCLUSION

In summary, it has been demonstrated a novel SERS biosensor design for the detection of HCV. The MS based sensor is relatively easy to prepare, low-cost and could detect the complementary DNA with high selectivity. The prepared sensor has magnetic property which allows the separation of the nanoparticles easily by an external magnet without any centrifuge step. In addition, the sensor does not need labelling the target DNA, and post-hybridization washing steps. The prepared sensor

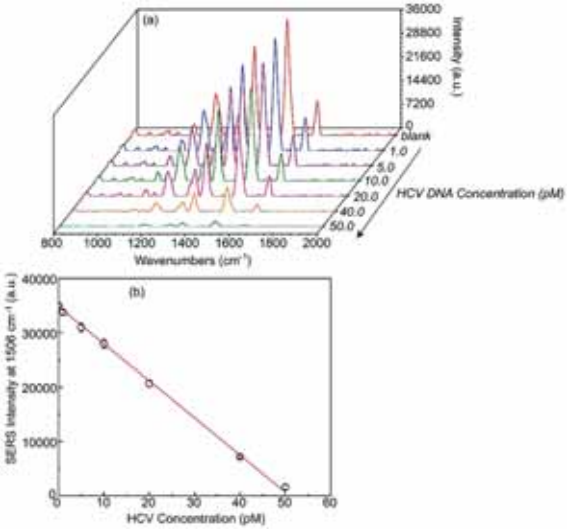

Figure 6. (a) SERS spectra of Fe_3O_4@Au@MS after hybridization with different amount of HCV DNA, (b) SERS intensity changing as a function of HCV DNA concentration.

can be extended to point-of-care disease with the help of commercially available portable, hand-held Raman spectroscopy.

ACKNOWLEDGEMENTS

The author thanks to Prof. Dr. Zekiye Suludere for TEM analysis and also thanks to Prof. Dr. Uğur Tamer for his valuable contributions for SERS measurements.

REFERENCES

1. Guillou–Guillemette HL and Lunel–Fabiani F, Detection and quantification of serum or plasma HCV RNA: Mini review of commercially available assays, in hepatitis C: Methods and protocols. ed. H. Tang, Humana Press, Totowa, NJ, 2nd edn 150 (2009) 3-14.
2. Zobair MY, Hepatitis C infection: A systemic disease, Clinics in Liver Disease 21 (2017) 449–453.
3. Thomas JR and Hergenrother PJ, targeting RNA with small molecules. Chemical Reviews 108 (2008) 1171–1224.
4. Li W, Wu P, Zhang H and Cai C, Catalytic signal amplification of gold nanoparticles combining with conformation–switched hairpin DNA probe for hepatitis C virus quantification. Chemical Communications 48 (2008) 7877-7879.
5. Liu L, Wang X, Ma Q, Lin Z, Chen S, Li Y, Lu L, Qu H and Su X, Multiplex electrochemiluminescence DNA sensor for determination of hepatitis B virus and hepatitis C virus based on multicolor quantum dots and Au nanoparticles. Analytica Chimica Acta 916 (2016) 92–101.
6. Skladal P, Riccardi CS, Yamanaka H and Costa PI, Piezoelectric biosensors for real–time monitoring of hybridization and detection of hepatitis C virus. Journal of Virological Methods 117 (2004) 145–151.
7. Wenbing L, Xinchu Z, Zhifeng Y, Glushenkov AM, and Kong L, Plasmonic substrates for surface enhanced Raman scattering. Analytica Chimica Acta 984 (2017) 19–41.
8. Cho I–H, Das M, Bhandari P, and Irudayaraj J, High performance immunochromatographic assay combined with surface enhanced Raman spectroscopy. Sensors and Actuators B: Chemical, 213 (2015) 209–214.
9. Herrera G, Padilla A, and Rivera SH, Surface enhanced Raman scattering (SERS) studies of gold and silver nanoparticles prepared by laser ablation. Nanomaterials 3 (2013) 158–172.
10. Stockman MI, Nanoplasmonics: past, present, and glimpse into future. Optics Express 19 (2011) 22029–22106.
11. Pang Y, Wang J, Xiao R, Wang S, SERS molecular sentinel for the RNA genetic marker of PB1–F2 protein in highly pathogenic avian influenza (HPAI) virus. Biosensors and Bioelectronics 61 (2014) 460–465.
12. Wang H–N, Fales AM, Zaas AK, Woods CW, Burke T, Ginsburg GS, Vo–Dinh T, Surface–enhanced Raman scattering molecular sentinel nanoprobes for viral infection diagnostics. Analytica Chimica Acta 786 (2013) 153–158.
13. Tumturk H, Sahin F and Turan E, Magnetic nanoparticles coated with different shells for bio recognition high specific binding capacity. Analyst 139 (2014) 1093-1100.
14. Haiss W, Thanh NTK, Aveyard J, and Fernig DG, Determination of size and concentration of gold nanoparticles from UV÷Vis spectra. Analytical Chemistry 79 (2007) 4215-4221.
15. Qin W, Song Z, Fan C, Zhang W, Cai Y, Zhang Y, and Qian X, Trypsin immobilization on hairy polymer chains hybrid magnetic nanoparticles for ultrafast, highly efficient proteome digestion, facile ^{18}O labeling and absolute protein quantification. Analytical Chemistry 84 (2012) 3138-3144.
16. Kouassi GK, and Irudayaraj J, Magnetic and gold–coated magnetic nanoparticles as a DNA sensor. Analytical Chemistry 78 (2006) 3234-3241.
17. Griffin J, Singh AK, Senapati, Lee E, Gaylor K, Jones–Boone J. and Ray PC, Sequence–specific HCV RNA quantification using the size–dependent nonlinear optical properties of gold nanoparticles. Small 5 (2009) 5, 839.
18. Liu S, Hu Y, Jin J, Zhang H and Cai CX, Electrochemical detection of hepatitis C virus based on site–specific DNA cleavage of BamHI endonuclease. Chemical Communications 2009, 1635–1637.
19. Liu S, Wang Q, Chen D, Jin J, Hu Y, Wu P, Zhang H and Cai CX, Electrochemical approach for the specific detection of hepatitis C virus based on site–specific DNA cleavage of BamHI endonuclease. Analytical Methods 2 (2010) 135–142.

Hittite Journal of Science and Engineering, 2018, 5 (3) 231-237
ISSN NUMBER: 2148-4171
DOI: 10.17350/HJSE19030000100

Mechanical Properties of Trip Aided Bainitic Ferrite (TBF) Steels in Production and Service Conditions

Eren BİLLUR[1,2], Semih KARABULUT[3], İmren ÖZTÜRK YILMAZ[4], Samet ERZİNCANOĞLU[3], Hafize ÇELİK[3], Evren ALTINOK[3], Tanya BAŞER[3]

[1]Atılım University, Metal Forming Center of Excellence, 06830, Ankara, TURKEY
[2]Billur Metal Form Ltd., 16120, Bursa, TURKEY
[3]TOFAŞ Türk Otomobil Fabrikası A.Ş., 16110, Bursa, TURKEY
[4]Beyçelik Gestamp A.Ş., 16110, Bursa, TURKEY

Article History:
Received: 2017/11/14
Accepted: 2018/03/13
Online: 2018/09/30

Correspondence to: Eren Billur, Atılım University, Metal Forming Center of Excellence, 06830, Ankara, TURKEY
E-Mail: eren@billur.com.tr
Phone: +90 224 442 85 00

ABSTRACT

In the automotive industry, one of the most common methods to reduce the weight of the body components is to downgage the sheets using higher strength steels. In the design phase, engineers typically use the material properties of the incoming material, such as the yield strength and the elongation. For forming analyses, however, more detailed characterization is required (flow curves, anisotropy, forming limit curves, etc.). Once the components are formed in the press shop, the yield strength increases due to work (strain) hardening. The parts are then welded in the body shop, and the body-in-white goes to the paint shop where it is baked to cure the paint. Most steels' yield strength changes during this paint bake cycle, which determines its final properties in service. Bake hardening (and in some cases, bake softening) is measured by Bake Hardening Index (BHI) as defined by EN 10325-2006. The standard dictates relatively low pre-strain (2%) and baking temperature (170°C). In real production conditions however, higher strains are achieved and baking temperatures may exceed 170°C to shorten the baking time. In this study, a new generation Advanced High Strength Steel (AHSS) grade TBF 1050 was characterized for metal forming purposes and its bake hardening response was studied both as the standard suggests and as the real production cycle dictates.

Keywords:
Advanced High Strength Steels; Material Characterization; Metal Forming; Elastic/Plastic Properties; Bake Hardening

INTRODUCTION

Automotive industry is under the pressure of complying government regulations of improved crash safety and low exhaust emissions [1]. To improve crash performance, additional reinforcements may be required, adding more weight to the car body [2]. Additional weight, in return, would increase the fuel consumption and thus increase exhaust emissions. To build safe and lightweight vehicles, materials with high strength to weight ratio are required [3].

High strength steels have been long used in the automotive industry and have replaced mild steels in most of the crash relevant components in the last decades. With "conventional" high strength steels (HSS), as the strength was increased the formability was reduced drastically, as seen in Fig. 1. The conventional HSS class involves various steel families including: (1) Bake Hardenable (BH), (2) Carbon-Manganese alloyed steels (CMn), and (3) High Strength Low Alloy (HSLA) grades [4]. These steels are single phase (ferritic) and have been dominating the crash components of cars until 1990's [5].

"Advanced" high strength steels (AHSS) consist of more than one phase and have been developed as early as 1970's [6]. It was mid 1990's, when cold rolled dual-phase (DP) steels were commercially available for the automotive industry [7]. These steels have ductile ferritic matrix with islands of hard martensite. The strength is increased by adjusting the alloying elements (mostly carbon) and/or the percentage of martensite [8].

Transformation Induced Plasticity (TRIP) steels were first defined in 1967 [9]. These steels have up to 15% retained austenite, which would transform to

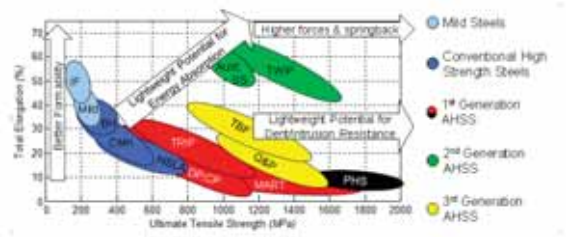

Figure 1. Steel banana curve, showing several different grades and classes.

martensite when plastically deformed. This so-called TRIP effect increases elongation [10]. Martensitic steels for cold (MART) and hot forming (Press hardened steel, PHS) are also classified as 1st generation AHSS. Currently PHS is the strongest steel family used in the automotive industry (up to 1300 MPa yield and 1800 MPa tensile strength), but requires a special hot forming line [4].

In 1998, Grässel and Frommeyer have developed Twinning Induced Plasticity (TWIP) steels [11]. These grades are classified as 2nd generation AHSS [5] and have very high elongation and strength. Over 60% total elongation was reported on a commercially available TWIP Steel with 500 MPa Yield and 980 MPa tensile strength [12]. Although seemed very promising, 2nd generation AHSS did not find many industrial applications, due to high material costs and poor weldability [13].

Since the beginning of the decade, automotive industry has been demanding high strength steels that have higher formability compared to 1st generation AHSS and less alloying elements compared to the 2nd generation [14]. Currently, Quenching & Partitioning (Q&P) steels and TRIP aided Bainitic Ferrite steels are commercially available and can be considered as 3rd generation AHSS [13].

This paper studies a TBF steel's mechanical properties in detail and also discusses the `in-service` properties after work and bake hardening effects.

BACKGROUND

When a steel sheet is formed in the press shop, the straining would increase the yield strength and hardness; and reduces the ductility. This is called strain hardening (also known as work hardening) [15]. Work hardening of a material can be easily measured by a simple tensile test. In TRIP steels and TRIP-aided steels, very high strain hardening is observed until the uniform elongation [16]. This can be explained by the localized high strain hardening rate, caused by formation of mobile dislocations and the transformation of retained austenite to martensite [17, 18].

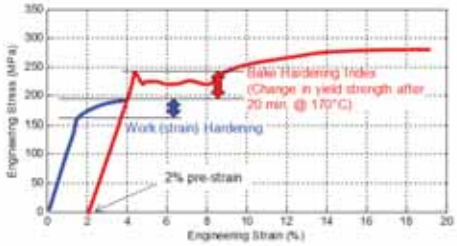

Figure 2. Work and bake hardening as explained in the standard (recreated after [20]).

In press shops, when a steel is deformed its thickness is reduced, but its yield strength is increased by work hardening. Typically, in computer-aided-engineering (CAE) calculations, both of these effects are included. For example, NVH and crash simulations include both thinning and hardening effects. However, bake hardening effect was mostly discarded [19].

Bake hardening is the increase of yield stress after deformation, followed by a baking cycle. Bake hardenability of a steel is typically measured by tensile test [3], according to EN 10325-2006 standard [20]. Fig. 2 summarizes how the "Bake Hardening Index" is measured. According to the standard, the deformation is limited to 2% pre-strain (engineering) and baking cycle is at 170°C for 20 minutes.

Since there is a class of "Bake Hardenable" steels, one may think that other high strength steels do not harden during bake cycle. In reality, most AHSS grades also harden after baking. In most steel datasheets, bake hardening index is given as a material property. For a given dual phase steel (cold rolled DP590, CR330Y590T-DP) for example, most steel makers claim a minimum 30 MPa bake hardening index (BHI as shown in Fig. 2, sometimes abbreviated as BH_2) [21, 22, 23].

However, former studies have shown that even at 2% pre-strain, much higher BHI was achieved. A study by Volvo for example, showed that the yield strength of DP1000 was increased from 760 to 1020 MPa after work and bake hardening. Similarly, the yield strength of DP1200 was increased from 950 to 1220 MPa [24].

In another study by Salzgitter, tensile specimens cut from real automotive components were tested. Results are tabulated in Table 1. Since the pre-strain was not kept constant, but changed with the part complexity, work hardening numbers were not constant [25].

Since the new generation AHSS have higher formability compared to steels with similar yield strength; the part complexity and thus the pre-strain could be even higher. Effect of pre-strain was known and studied as early as 1990's

Table 1. Summary of work and bake hardening, samples were cut from press formed automotive components, made of DP590 (CR330Y590T-DP) [25].

Part and thickness	*Work hardening (MPa)*	*Bake hardening (MPa)*
Seat cross member, 1.0 mm	*179-189*	*52-59*
A-pillar lower 2.0 mm	*66-67*	*131-137*
D-pillar reinforcement 1.0 mm	*206-210*	*52-79*

[26]. However, most of the early works had limited pre-strain. A summary of several studies on pre-strain is given in Fig. 3 [26, 27, 28, 29].

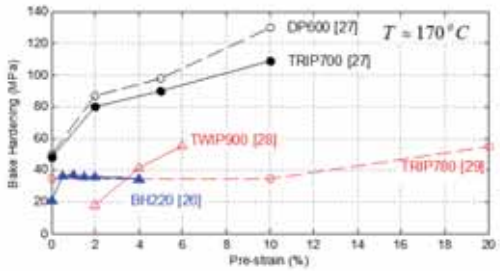

Figure 3. Bake hardening responses of several HSS and AHSS with varying pre-strain [26-29].

Lastly, the standard dictates that the bake hardening studies should be done at 170°C. However, in manufacturing conditions, temperature in the paint bake tunnel may increase over 200°C. Typically if the furnace temperature exceeds 170°C, the baking time could be reduced, as long as the time-temperature profile is within the acceptable region, as shown in Fig. 4 [30]. This is of extreme importance, as the paint shops are typically the bottleneck of a car maker. The capacity of the total production is generally limited by the paint shop. If the cycle time here could be reduced, the overall productivity could be boosted [31].

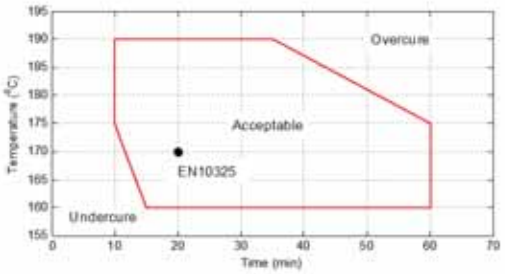

Figure 4. An example e-coat curing bake chart [30].

A special condition in bake hardening of TBF steels is the fact that, they contain ferrite, bainite, martensite and retained austenite. It is reported that from these phases bainite contributes most to BH response. It is also possible that some fraction retained austenite may transform due to holding at high temperature for several minutes, or the martensite may be tempered [16, 27]. According to [32], the amount of retained austenite does not change with temperatures up to 170°C for a TRIP 700 steel. Only after 700 minutes holding at 220°C, the retained austenite fraction started to decrease in the aforementioned steel.

Several studies in the literature has also shown that with increased baking temperature, higher bake hardening response could be determined [26, 28]. In this study, (1) TBF steels are studied, and (2) the baking time was reduced with increased baking temperature.

EXPERIMENTAL STUDIES

In this study, commercially available, cold rolled TBF 1050 steels are studied at two different thickness levels: 1.0 and 1.6 mm. These steels were characterized using:

1)Tensile tests with extensometers to determine, yield strength and Lankford parameters in three directions (r_0, r_{45}, r_{90});

2)Elemental analysis to determine chemical composition;

3)Elastic modulus determination by Resonance Frequency and Damping Analysis (RFDA);

4)Disk compression test to determine biaxial yield stress (σ_b) and anisotropy coefficient (r_b);

5)Bake hardening experiments at 0%, 2%, 5% and 10% pre-strain; at various "industry emulating" temperatures and durations.

Tensile Tests

Tensile specimens were manufactured using wire EDM method to minimize the damage at the edges. Tests were conducted at two crosshead speeds: 30 mm/min and 150 mm/min. Although there was no strain rate control, these crosshead speeds gave relative constant true strain rate levels of: (3.75±0.10)x10^{-3} and (18.3±0.2)x10-3s^{-1}. As illustrated in Fig. 5, the yield strength was found to be sensitive to the strain rate; whereas the ultimate tensile strength was predominantly affected by the thickness.

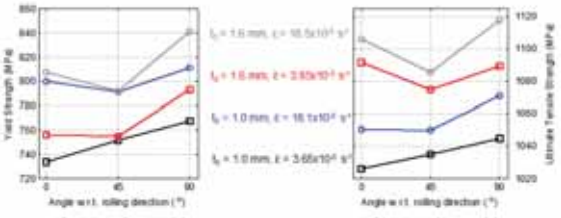

Figure 5. Yield and ultimate tensile strength of TBF 1050 steels.

Table 2. Summary of tensile tests, compared with the literature [33, 34].

	Experiments		Literature	
	751^{+17}_{-17}	800^{+10}_{-10}	Datasheet [29]	t_o = 1.2 mm [30]
Yield Strength (MPa)[1]	1035^{+10}_{-10}	1057^{+14}_{-7}	700-820	775
UTS (MPa)[1]	$17^{+0.7}_{-0.7}$	$13.5^{+1.2}_{-0.9}$	1050-1180	1235
Elongation (%)[1]	179-189	Seat cross member, 1.0 mm	≥14	10
r_o	0.778	0.786	-	0.795
r_{45}	0.905	0.958	-	0.930
r_{90}	0.995	0.911	-	0.983

[1]Values determined from slow strain rate experiments.

Material properties found in this study are tabulated and compared with the literature in Table 2.

Elemental analysis

Elemental analysis was performed on 1.0 mm thick steels, using Bruker Q4 optical emission spectrometer. Samples were measured 10 times, at different locations. The results were compared with the literature in Table 3.

Table 3. Chemical composition (wt.%) of TBF 1050, compared with literature [33, 34].

wt. %	C	Mn	Si	P	Al
This study	$0.203^{+0.034}_{-0.021}$	$2.253^{+0.194}_{-0.197}$	$1.027^{+0.194}_{-0.096}$	$0.015^{+0.004}_{-0.004}$	$0.045^{+0.009}_{-0.007}$
Datasheet [34]	<0.23	<2.3	<2	-	-
Literature [35]	0.207	2.178	1.452	0.011	0.037

Elastic modulus measurement using RFDA

Elastic modulus measurement was done using impulse excitation and resonant frequency and damping analyser (RFDA) system. In this method, a rectangular specimen is placed on two supporting wires. An impulse excitation is given by the system, and a microphone records the vibrations. Through signal processing, elastic properties of a specimen could be determined. Details of the methodology and the system used in this study can be studied in detail from reference [35]. In this study, 55x10 mm specimens were prepared using wire EDM. 4 test specimens were produced for each thickness. Results are tabulated in Table 4.

Table 4. Elastic modulus measurements.

Elastic Modulus (GPa)	Thickness	
	1.0 mm	1.6 mm
Test 1	192.77	189.08
Test 2	192.68	189.14
Test 3	192.50	188.21
Test 4	192.43	189.17
Average	$192.60^{+0.17}_{-0.17}$	$188.90^{+0.27}_{-0.69}$

Disk compression tests

For metal forming simulations, yield locus is one of the most important input data. To build some of the modern yield loci (such as Yld2000 or Banabic 2005), biaxial anisotropy coefficient (r_b) and biaxial yield strength (σ_b) are required [36, 37]. A method to determine these coefficients is disk compression test [38].

10 mm diameter disks were cut using wire EDM technique. These are then compressed in a universal tensile machine. The final disks became elliptical, and the ratio

$$r_b = \frac{\varepsilon_{22}}{\varepsilon_{11}}, \qquad \varepsilon = \ln\left(\frac{D_f}{D_i}\right)$$

Figure 6. Calculation of biaxial anisotropy coefficient (after [37]).

between the strains gives the biaxial anisotropy coefficient, as summarized in Fig. 6. Calculated values are given in Tab-

Table 5. Biaxial anisotropy coefficients.

Applied Force	Thickness	
	1.0 mm	1.6 mm
150 kN	D_{f1} = 10.99mm D_{f2} = 10.91mm r_b = 0.922	D_{f1} = 10.71mm D_{f2} = 10.61mm r_b = 0.863
200 kN	D_{f1} = 11.70mm D_{f2} = 11.50mm r_b = 0.890	D_{f1} = 11.25mm D_{f2} = 11.18mm r_b = 0.947
Average r_b	192.50	188.21

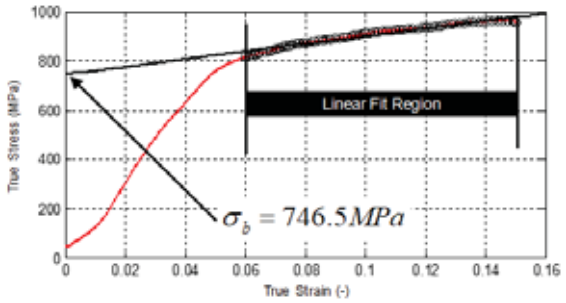

Figure 7. Calculation of biaxial yield strength (after [37]).

le 5. The biaxial yield strength is calculated using a linear fit [37], as shown in Fig. 7.

Bake hardening studies

As discussed in earlier sections, in this study: (1) higher pre-strains and (2) realistic furnace conditions were studied. Since the tensile tests have shown that the parts can be deformed 12.6-17.7% total elongation (see Table 2), the maximum pre-strain was selected to be 10%. The tensile specimens were pre-strained to 2, 5 and 10% using a universal tensile test machine. Specimens were then placed in the furnace which is already pre-heated to the temperatures listed in Table 6. Furnace temperature and

Table 6. BDetails of the bake hardening conditions.

Conditions	*Furnace Temp. (°C)*	*Dwell time (min.)*	*Reference*
1	*170*	*20*	*EN10325 [20]*
2	*195*	*15*	*Tofaş*
3	*205*	*15*	*Tofaş*

dwell time data are received from Tofaş. To compare the results, conditions of EN10325 were also studied. Once the specimens stay in the furnace for the given time, they were taken out. The specimens were air cooled to room temperature and tensile tests were performed until fracture. Results of one test conditions can be seen in Fig. 8.

As seen in Fig. 8, when the tensile curves are shifted with pre-strain, the difference between the "as-received" curve and the tested material's curve gives the bake hardening. To calculate the work hardening, it is possible to use the stress level on the "as-received" curve and subtract the yield strength of the corresponding material (i.e., 1.0 mm or 1.6 mm thick). Work hardening values were quite repeatable. This can be seen in Fig. 9a-b.

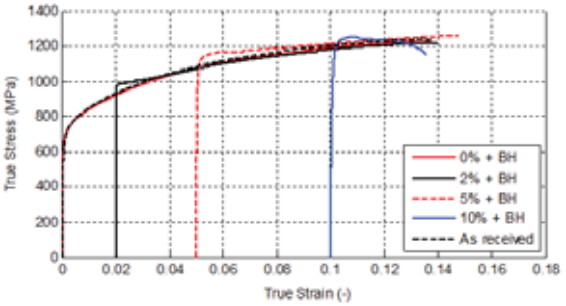

Figure 8. Tensile test results after pre-strain and bake hardening (1.0 mm thick blanks, 170°C furnace temperature, 20 minutes dwell time).

With only two exceptions, as pre-strain and as temperature is increased, the bake hardening was found to be increasing. In addition, the bake hardening response of TBF steels was found to exceed 200 MPa, when 10% pre-strain is applied. Even at 5% pre-strain, 1200 MPa yield strength could be achieved after bake hardening.

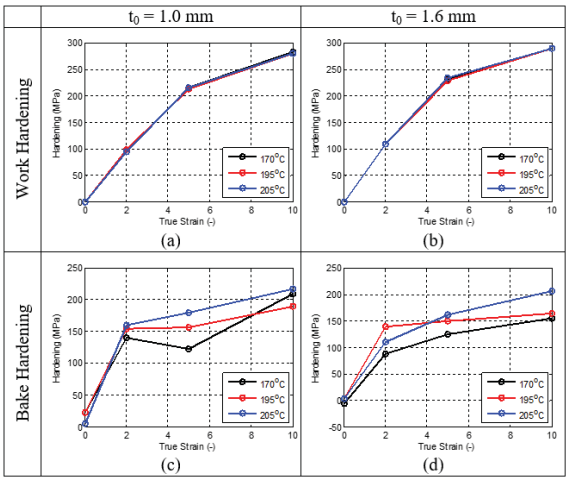

Figure 9. Summary of work and bake hardening at different conditions.

CONCLUSION

In this study, a commercially available 3rd generation AHSS grade had been selected and its elastic/plastic properties were characterized, including its bake hardening response. It has to be noted that these values are only from one batch of one producer.

Elemental analyses have proved that 3rd generation AHSS had relatively low alloying elements, especially compared to 2nd generation AHSS. As the blank has low carbon equivalency, its welding parameters are expected to be compatible with current body shops. A further study on weldability is currently ongoing.

Further analysis on the phase fractions (especially retained austenite) is required to understand how the changes in phase fractions may have effect on the hardening, anisotropy and bake hardening responses.

Elastic modulus of these steels was found to be on the lower side of steels. This information may be useful for further studies about springback of these grades.

Biaxial material properties as required by some yield criterion were measured by disk compression test. Currently there is no literature data to compare these results. In future, these values could be used to build YLD2000-2D or BBC2005 yield criteria; and by using finite element simulations, the material model could be validated.

One of the main purposes of using cold formable advanced high strength steels is to reduce press hardened steels (PHS). It was clearly found that after press forming and bake hardening, this grade may have a yield strength over 1200 MPa. This is comparable to PHS, which would require a special hot forming line and expensive process.

ACKNOWLEDGEMENT

This study has been supported by Turkish Science Foundation (TÜBİTAK), Project number: 3150934. Authors would like to thank Mr. Emin Tamer and Asst. Prof. Dr.-Ing. Kemal Davut of Atılım Univeristy Metal Forming Center of Excellence for their help in experimental work.

References

1. Taub AI, Luo AA, Advanced lightweight materials and manufacturing processes for automotive applications. MRS Bulletin 40/12 (2015) 1045-1054.
2. Robert H and Scherre JM, New Peugeot 3008. Proceedings of EuroCarBody 2016, (2016), Bad Nauheim, Germany.
3. Senuma T, Physical Metallurgy of Modern High Strength Steel Sheets, ISIJ International 41/6 (2001) 520-532.
4. Billur E, Altan T, Three generations of advanced high-strength steels for automotive applications, Part I. Stamping Journal, Nov.-Dec., (2013) 16-17.
5. Pichler A, Hebesberger T, Krizan D, Winkelhofer F, Fruber M, Walch C, 3rd Generation of AHSS Grades: A New Family of Steel Grades with a Significantly Improved Balance between Strength and Formability. Proceedings of Materials in Car Body Engineering 2014, (2014), Bad Nauheim, Germany.
6. Araki K, Takada Y, Nakaoka K, Work hardening of continuously annealed dual phase steels. Trans. Iron Steel Inst. Jpn. 17/12 (1977) 710-717.
7. ThyssenKrupp Stahl AG, Höherfester Stahl für den Automobil-Leichtbau. ThyssenKrupp Stahl, No: 2045, (1999), Duisburg.
8. Ramazani A, Bruehl S, Gerber T, Bleck W, Prahl U, Quantification of bake hardening effect in DP600 and TRIP700 steels. Materials & Design 57/C (2014) 479-486.
9. Zackay VF, Parker ER, Fahr D, Busch R, The enhancement of ductility in high-strength steels. ASM Trans Quart 60/2 (1967) 252-259.
10. Samek L, Krizan D, Steel--material of choice for automotive lightweight applications. Metal Review (2012) 1-6.
11. Grässel O, Frommeyer, G, Effect of martensitic phase transformation and deformation twinning on mechanical properties of Fe-Mn-Si-Al steels. Materials Science and Technology 14/12 (1998) 1213-1217.
12. Billur E, Çetin B, Uğuz RO, Davut K, Arslan E, Advanced Material Characterization of TWIP Steels. Proceedings of New Developments in Sheet Metal Forming (2016) 303-318.
13. Davenport M, Third-generation advanced high strength steel emerges, Stamping Journal, Sept.-Oct., (2017) 22-28.
14. Branagan D, Overview of a New Category of 3rd Generation AHSS. Presented at Great Designs in Steel 2013, May 1, Livonia, MI, USA 2013.
15. Altan T, Tekkaya AE. Sheet metal forming: processes and applications, ASM International, 2012, ISBN:978-1615038442.
16. Fonstein N. Advanced High Strength Sheet Steels, Springer, 2015.
17. Sugimoto K, Mukherjee M, Chapter 8 - TRIP aided and complex phase steels, in: Automotive Steels, Rana R, Singh, SB (eds.) Woodhead Publishing, pp. 217-257, 2017.
18. Li SH, Dan WJ, Zhang WG, Lin ZQ, A model for strain-induced martensitic transformation of TRIP steel with pre-strain, Computational Materials Science 40/2 (2007) 292-299.
19. Stillger M, Brenne T, Feasibility-Simulation and Systematic Process Improvement of Hot Forming Parts as well as Mapping of Results to Vehicle Simulation, in: Proceedings of New Developments in Sheet Metal Forming 2016 (NEBU 2016), pp. 213-230, 2016.
20. European Committee for Standardization, EN 10325:2006: Steel - Determination of yield strength increase by the effect of heat treatment [Bake-Hardening-Index], 2006.
21. ArcelorMittal, Dual Phase Steels,, Product Brochure, 2017.
22. SSAB, Docol 590DP,, Product Brochure, 2017.
23. Voesatlpine Steel Division, Dual-Phase Steels,, Product Brochure, 2017.
24. Jonason, P, Aluminium intensive door - Mixmetal door structure, Presented at Doors and Closures in Car Body Engineering 2010, Bad Nauheim, Germany, 2010.
25. Flaxa V, Schulz T, Schulz S, Mohrbacher H, Entwicklung eines modularen Legierungskonzeptes für HDG DP-Stähle nach VDA239, 2013.
26. Pradhan, R, Dent-Resistant Brake-Hardening Steels for Automotive Outer-Body Applications, in SAE Technical Paper, SAE:910290, 1991.
27. Pereloma E, Timokhina I, Chapter 9 - Bake hardening of automotive steels, in Automotive Steels, in: Automotive Steels, Rana R, Singh, SB (eds.) Woodhead Publishing, pp. 259-288, 2017.
28. Kilic S, Ozturk F, Sigirtmac T, Tekin G, Effects of Pre-strain and Temperature on Bake Hardening of TWIP900CR Steel, Journal of Iron and Steel Research 22/4 (2015) 361-365.
29. Robertson LT, Hilditch TB, Hodgson PD, The effect of prestrain and bake hardening on the low-cycle fatigue properties of TRIP steel, International Journal of Fatigue 30/4 (2008) 587-594.
30. Dickie RA, Bauer DR, Ward SM, Wagner DA, Modeling paint and adhesive cure in automotive applications, Progress in Organic Coatings 31/3 (1997) 209-216.
31. Weenink W, Car Plants Order New Paint Shops, Automotive News Europe, 23 June 1997.
32. Bleck W, Bruhl S, Bake hardening effects in advanced high strength steels. In New Development on Metallurgy and Applications of High Strength Steels, 2008.
33. ArcelorMittal, Steels for cold stamping -Fortiform®,, Product Brochure, 2014.
34. Galdos L, de Argandoña ES, Mendiguren J, Gil I, Ulibarri U, Mugarra, E, Numerical simulation of U-Drawing test of Fortiform 1050 steel using different material models, Procedia Engineering 207 (2017) 137-142.
35. Bollen B, The Impulse Excitation technique,, in AMAP Colloquium, Aachen, Germany, 2017.
36. Banabic D, Sester M, The Influence of the Constitutive Equations on the Accuracy of Sheet Metal Forming Processes Simulation, in Die and Mold, Ankara, Turkey, 2011.

37. Xu L, Barlat F, Disk compression testing and constitutive modeling of TWIP sheet sample. In: Proceedings of ICTP (2008) 2312-2317.
38. Barlat F, Brem JC, Yoon JW, Chung K, Dick RE, Lege DJ, Pourboghrat F, Choi S-H, Chu E, Plane stress yield function for aluminum alloy sheets—Part 1: Theory, International Journal of Plasticity 19/9 (2003) 1297-1319.

Hittite Journal of Science and Engineering, 2018, 5 (3) 239-247
ISSN NUMBER: 2148-4171
DOI: 10.17350/HJSE19030000103

Drilling of Horizontal Wells in Carbonate Reservoirs of Middle East for Petroleum Production – Investigation of Hydraulics for the Effect of Tool Joints

Tuna Eren[1]
[1]Izmir Katip Celebi University, Petroleum and Natural Gas Engineering Department, İzmir, TURKEY

ABSTRACT

Drilling of a horizontal well to produce petroleum is a task which needs careful planning. The foremost advantage of an openhole horizontal well completion is having the pay zone with the least drilling damage. The first task whether a well can be completed in open hole is by knowing if the formation once drilled is competent enough so that it can remain intact or not. Once the formation is declared and/or proofed to be competent and drilling of the horizontal well is approved there should be enough time to ensure that all equipment and services are going to be available. This study synopsises a brief literature review regarding effects of tool joints during drilling. A diligently planned horizontal well design for Middle East formations is given in this study. The effects of tool joints on the drillpipes are taken into consideration for the calculation of frictional pressure losses in annulus and equivalent circulating density itself. The operational steps while drilling the horizontal well are synopsised in this manuscript, which can be a useful guide for future applications in various petroleum and gas fields. The study also includes frictional pressure calculations for non-newtonian fluids used in drilling operations. The results indicate whether while drilling a horizontal well the fracture gradient of the petroleum reservoir formation is exceeded or not. The study can be improved further by means of considering the effects of temperature on the behaviour of the drilling fluids.

Article History:
Received: 2018/01/22
Accepted: 2018/03/21
Online: 2018/04/06

Correspondence to: Izmir Katip Celebi University, Petroleum and Natural Gas Engineering Department, Cigli Ana Yerleskesi, Merkezi Ofisler 1 Binasi, 35620, Cigli, Izmir, Turkey,
E-mail: tuna.eren@ikc.edu.tr,
Phone: +905325437217,
Fax: +90(232) 386 08 88

Keywords:
Open hole; Horizontal well; Completion; Limestone reservoir; Pressure depletion; Drilling; Tool joint; Equivalent circulating density

INTRODUCTION

It is known that Middle East oil fields are dominated by carbonate reservoirs inside which the big majority of the oil and gas reserves are located. It is to the knowledge of reservoir engineers that carbonate reservoirs can have significantly varying rock properties such as porosity, permeability. This property of carbonates makes them a challenging reservoir type to exploit hydrocarbons. One solution to penetrate through the best quality reservoir sections is to drill horizontal wells, and even completing the wells in open hole. Horizontal wells in unknown oil/gas fields would require drilling of a pilot hole. Pilot hole is a wellbore trajectory that is drilled and abandoned once the landing point formation details have been acquired. In some mature oil fields located in southern Iraq; recently introduced High Angle Wells allowed drilling horizontally into a seam and under infrastructure with substantially improved results.

Not only for horizontal wells with relatively long drainages, the margin between pore and fracture gradients are getting critical also for the ultra deep and deep-water applications. One factor that influences the ECD (Equivalent Circulating Density) which is effected by the drilling fluid's hydrostatic column and the frictional pressure losses along the flow circuit. The frictional pressure losses are the term that depends on the flow geometry, fluid rheological properties and last but not the least the flow rates. What industry approaches have considered so far, are based on the fact that the effects of the tool joints of the drillpipes are not necessarily taken into the consideration when the frictional pressure losses are calculated. An experienced drilling engineer in the field should always bear in mind that a single segment of a tool joint may not result in excessive frictional pressure loss individually. However knowing that there are hundreds of tool joints in a wellbore at a depth of

3000 m, the sum of the frictional pressure losses for all of the tool joint segments could result in additional substantial frictional pressure loss. It is that additional substantial frictional pressure loss which would increase the ECD and could be the very main reason for well to encounter drilling troubles.

LITERATURE REVIEW

Plenty of researches worked on horizontal drilling planning and openhole completions respectively. One of the most significant findings of the previous researchers is importance of paying attention to the to the details regarding geology, hydraulics and strength of materials when dealing with high angle wells and particularly horizontal wells Aguilera et. al. [1]. Horizontal drilling is only successful if everyone understands the objectives of different operations. It is known and as stated in API RP 13D [2] that in case of deviated wells there is no simple method that exists to calculate the contribution of the cuttings over the ECD (Equivalent Circulating Density). Hole inclinations between 30 degrees to 60 degrees are the most difficult holes to clean. This fact is due to the existence of unstable solid beds on the low side of the wellbore. The problem is the risk of having these unstable solids bed avalanching towards the bottom of the hole. However, downhole annular pressure measurements can be monitored to estimate the contribution of the cuttings over the static drilling fluid density.

Azar and Samuel [3], stated that a number of mathematical models have been derived from a combination of experimental flow-loops to model hole cleaning. It is important to keep in consideration that the derived empirical equations are valid for the size configuration that their respective data has been acquired from. Scaling up the correlations to different hole geometries may introduce significant errors.

Viloria [4] conducted a research study on the analysis of drilling fluid rheology and tool joint effect to reduce the errors in hydraulics calculations. It has been indicated that the current API recommended drilling hydraulics calculation techniques do not include tool joint parameters. Thus the API calculations can be deemed as inaccurate. Their study revealed that the frictional pressure losses being affected by the tool joints of the drill pipes can be corrected by means of implementing appropriate practical methods.

Even though the equations in use of the industry does not account for the effect of the tool joints in hydraulic pressure loss calculations, it is known that effects of the tool joints are significantly important when it comes to observe the annular frictional pressure losses. Enfis et. al. [5] performed extensive experiments to study the effects of the tool joints of drill pipes on frictional pressure losses in annulus. They concluded that the presence of tool-joints in a wellbore substantially increases the annular pressure losses (up to 30 %).

Simoes et. al. [6] performed Computational Fluid Dynamics analysis to investigate the effects of tool joints on the annular frictional pressure losses. Their findings revealed that the presence of tool joints significantly increased the pressure gradient.

Jeong and Shah [7] analysed the tool joint effects for accurate frictional pressure loss calculations. Their research study composed of gathering experimental data conducted with three different fluids. They concluded that presence of tool joints on the annular frictional pressure losses is significant and an accurate prediction method has been proposed.

Previous research studies indicate that a sound planning is the key to success and the effects of tool joints is a requirement that has got to be considered to ensure a trouble free drilling activity for horizontal wells.

HORIZONTAL WELL DRILLING PRACTICES

Horizontal well drilling planning is a joint task. The planning is based on following trajectory definition and determination of drilling engineering related decisions. The subsurface team and drilling team is required to work in collaboration. A work flow for a horizontal well planning is given in Fig. 1. The initial proposal originates from sub surface team as to where to drill the well. The directional plan is worked out jointly by the drilling team with the fine tuning until the formation tops are acceptable by the sub surface team. The casing points, drill string, hydraulics program and eventually the time estimate is prepared by the drilling team. The key to success in drilling operations is to keep things as simple as possible.

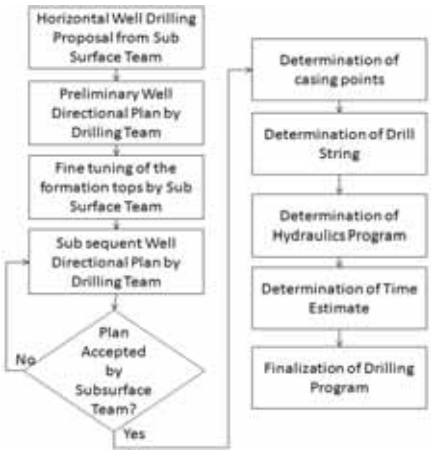

Figure 1. Horizontal well planning work flow

Most of the subsurface formations in Middle East Geomarket are relatively flat for a considerable subsurface extend. This results in having similar drilling cases in significant number of wells. Fig. 2 gives the Stratigraphic column for Rumaila and Zubair Oilfields, Al-Ameri et al. [8]. The critical drilling planning requirement depends on knowing the specifications of the formations to be encountered. Widespread assumption in the Middle East Geomarket especially for vertical wells is that they could be drilled without many troubles. However this assumption is recommended to be addressed carefully not only for vertical wells, but especially for highly deviated and horizontal wells. The critical aspects for a selected list of formations which are deemed important are as listed as follows:

Dammam Formation (Dominating lithology Limestone): Dammam formation is fragile for this reason tripping best practices are required to be implemented. Generally the surface casing string is set to the top of this formation. Running speed of the casing is required to be calculated not to exceed surge pressures to prevent the breakage of the formation which can induce downhole losses.

Tayarat Formation (Dominating lithology Limestone): Tayarat is known to be containing sulphurous water if kicks into the wellbore are going to result in a well control event. Within the Middle East formations the Tayarat Formation is required to be drilled with a drilling fluid having a density of approximately 8.68 ppg.

Tanuma Formation (Dominating lithology Shale): Tanuma Formation is one of the most challenging formations especially if drilling at inclinations in excess of 60 degrees. Tanuma formation is highly unstable and is required to be drilled as fast as practically possible. The drilling fluid properties are required to be kept with the necessary ranges outlined in the program. If KCl (Potassium Chloride) drilling fluid is being used, the KCl concentration is to be monitored and accordingly kept as necessary. Back reaming and

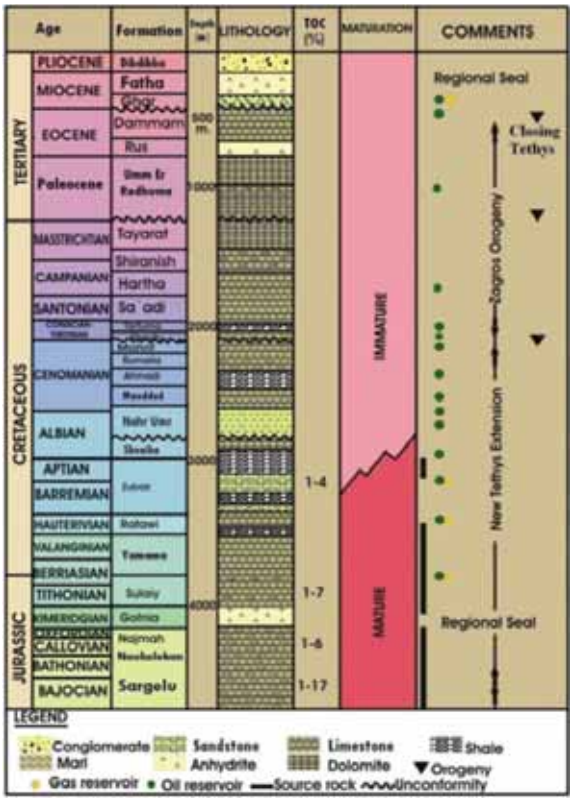

Figure 2. Stratigraphic column of South Iraq, Basrah region (Rumaila and Zubair oil fields), Al-Ameri et al., [8]

elongated circulations with BHA is to be prevented while in Tanuma.

An example geological prognosis including formation depths is as given in Table 1. When planning a horizontal well to Mishrif Formation (Middle Cretaceous) porous formation, the overlying formations should be studied very carefully. In given formation top depths the thickness of Tanuma formation is 40 m. However since the penetration of the trajectory across this zone is going to be at a specific angle the course of penetration is going to be more than 40 m.

Table 1. Geological prognosis of Rumaila field, after Arshad et. al., [9].

Formation Name	*Depth, m*	*Thickness, m*	*Age*	*Lithology Description*
Dibdiba	*Surface*	*997*	*Late Mio-Plio*	*Thicj sand and pebbles*
Lower Fars	*997.12*	*558*	*Early Middle Miocene*	*Interbedded argillaceos limestone, qnhydrite, claystone and gypsum*
Ghar	*1554.72*	*351*	*Early Middle Miocene*	*Thick sand and pebbles*
Dammam	*1905.68*	*813*	*Middle - Late Eocene*	*Thin limestone overlying thick karstic dolomite/limestone*
Rus	*2719.12*	*485*	*Paleocene-Early Eocene*	*Thich anhydrite interbedded with dolomite*
Umm Er-Radhuma	*3204.56*	*1492*	*Paleocene-Early Eocene*	*Dolomite with thin anhydrite interbeds*
Tayarat	*4696.96*	*712*	*Late Cretaceous*	*Bituminous shale overlying dolomite*
Shiranish	*5408.72*	*499*	*Late Cretaceous*	*Thick argillaceous marly limestone*
Hartha	*5907.28*	*731*	*Late Cretaceous*	*Dolomite and argillaceous limestone*
Sadi	*6638.72*	*689*	*Late Cretaceous*	*Thick interval of chalky, argilaceous limestone*
Tanuma	*7327.52*	*131*	*Late Cretaceous*	*Shale with localised limestone stringers*
Khasib	*7458.72*	*148*	*Late Cretaceous*	*Limestone with thin shale interbeds*
Mishrif	*7606.32*	*594*	*Middle Cretaceous*	*Limestone: white, brown, detrital, rudist, porous*
Rumaila	*8200*	*-*	*Middle Cretaceous*	*Thick sequence of marly and argillaceous limestone*

Directional Drilling Planning

The planning of a horizontal well necessitates a very careful study. The casing points are required to be appropriately selected, so that the casing shoes are placed into impermeable layers at the exit of which a competent seal is going to be achieved. Also it is very important that the exit of the casing shoe points for highly deviated and especially horizontal wells is strong enough. Under normal circumstances and especially in an unknown oil or gas field the casing points are required to be chosen by mean of kick tolerance calculations. Devereux [10] study indicated that the casing points should be selected so that the selected depths are going to allow kick tolerances to be maintained. The casing exit is required to be strong so that no problems such as washed formation are not going to be formed along the immediate exit of the casing shoe.

Planning of a horizontal well in 2-dimension is carried out by means of ensuring that build sections are planned in the manner that the downhole tools to be used are going to be able to perform the drilling activity. Fig. 3 gives the sketch of a 2-dimensional horizontal well.

The geometrical equations for the planning are mainly based on build up radius (R) as given in Equation 1;

$$R = 180 / (B \times \pi) \quad (1)$$

where B is the build up rate. The length of the hole is calculated by L, which is given in Equation 2;

$$L_{hole} = 100 \times (\beta_{ii} - \beta_i) / B \quad (2)$$

where β_{ii} and β_i are the final and initial wellbore inclinations respectively. The vertical section of the wellbore is calculated by means of Equation 3:

$$V = R \times (\mathrm{Sin}(\beta_{ii}) - \mathrm{Sin}(\beta_i)) \quad (3)$$

The wellbore displacements are calculated using Equation 4:

$$D = R \times (\mathrm{Cos}(\beta_i) - \mathrm{Cos}(\beta_{ii})) \quad (4)$$

The segment length of the build curve section is calculated using Equation 5:

$$\text{Build Curve} = (\beta_{ii} - \beta_i)/B \quad (5)$$

The tangent section length of the wellbore where the inclination is not changing is calculated by using Equation 6:

$$MD_{(\text{Tangent Length})} = D/ \mathrm{Sin}(\beta_i) \quad (6)$$

The Kick off, is the depth from which the wellbore deviates from vertical is calculated by means of Equation 7:

$$KOP = TVD - (H_3 + H_2 + H_1) \quad (7)$$

where H_2 can be calculated using Equation 8:

$$H_2 = MD_2/ \mathrm{Cos}(\beta_i) \quad (8)$$

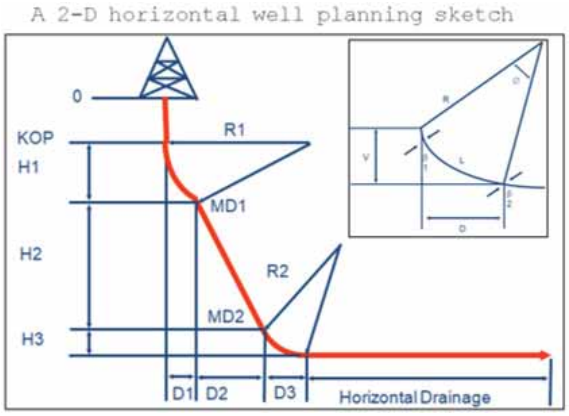

Figure 3. A 2-D horizontal well planning sketch.

A 2-D directional plan to drill the horizontal well in the carbonate formations is as given in Table 2. The depths are referenced to the formation tops given in Table 1. The planning of a directional well is required to respect the casing depths. The kick off point in order to deviate the well is selected to be at 6120 ft within Hartha Formation; a depth at which no more downhole losses are expected. The hole section that the well is kicked off is 12 1/4". The kick off for a directional well is strongly suggested to be selected at a depth after which circulation losses are not expected. The wellbore is planned to be drilled with a build of 4 deg /100 ft until the wellbore penetrates Sadi Formation at 6639 ft TVD. The 9 5/8" casing depth is planned to be 50 ft beneath the Sadi Formation. One of the most critical sections of the wellbore is the section to be built in 8 1/2" hole section. The field practices show that the Tanuma formation is suggested to be penetrated with a maximum inclination of 55 degrees. For this reason starting from the 9 5/8" casing shoe the trajectory is planned to be built to 55 degrees with a rate of 4.38 deg/100 ft in 8 1/2" hole section. For this reason once the wellbore inclination is 55 degrees, the wellbore is drilled tangent down to the top of the Mishrif formation. The wellbore is deepened to accommodate the 7" liner at a depth that is 50 ft below the top of Mishrif formation. Once the 7" liner is safely set in place, the last wellbore section is 6". The planned build rate is 5 deg/100 ft so that the inclination can be brought up to almost 90 degrees. Once the horizontal section commenced to be drilled the section is planned to be drilled almost 2300 ft, so that the well drilling operations can be finalized.

Table 2. 2D directional plan for horizontal well.

No	Command	Limit	Depth, ftMD	Depth, ftTVD	Horizontal Displacement, ft	Inclination, degree
1	0	0	0	0	0	0
2	Hold 0 degrees	Drill to Measured Depth 6120 ft	6120	6120	0	0
3	Build with 4 deg/100 ft	Drill to Vertical Depth 6639 ft	6651	6639	98	21.6
4	Hold at 21.6 degrees	Drill only 50 ft of additional hole	6701	6685	118	21.6
5	Build with 4.38 deg/100 ft	Drill to Vertical Depth 7265 ft	7452	7265	574	55
6	Hold at 55 degrees	Drill to Vertical Depth 7606 ft	8046	7606	1063	55
7	Hold at 55 degrees	Drill only 50 ft of additional hole	8095	7636	1102	55
8	Build with 5 deg/100 ft	Drill to 89.5 degrees	8774	7839	1738	89.5
9	Hold at 89.5 degrees	Drill only 2296 ft of additional hole	11070	7859	4034	89.5

The well sketch f the planned 2D directional trajectory is depicted in Fig. 4. The drawing gives the casing depths, formations, and well trajectory.

Calculation of Frictional Pressure Loss in Annulus

The frictional pressure loss equations presented by Adams and Charrier [11] are summarized in Fig. 5. The given equations are observed to give reasonable results when compared with actual pressure readings. Eren et. al., [12] performed a comparison of actual and theoretical pressures in wellbores, and concluded that the frictional pressure losses along wellbores could be predicted at an accuracy of ±25%. The details of the equations are as explained in the following section.

The velocity across the annulus is calculated using the below Equation 9:

$$V_{annulus} = q/(2.448 \times (d_2^2 - d_1^2)) \quad (9)$$

where q is the flow rate of the fluid. Plastic viscosity (μp) is the difference in between 600 rpm and 300 rpm readings of variable speed rheometer as presented in Equation 10;

$$\mu_p = \theta_{600} - \theta_{300} \quad (10)$$

The yield point (τ_y) is calculated using the relation given in Equation 11;

$$\tau_y = \theta_{300} - \mu_p \quad (11)$$

For each wellbore section a critical velocity (v_c) is required to be calculated using Equation 12;

$$v_c = [1.08\mu_p + 1.08 (\mu_p^2 + 9.26(d_2 - d_1)2(\mu_p)\rho)^{0.5}]/ [\rho(d_2 - d_1)] \quad (12)$$

where ρ is the density of the drilling fluid.

The pressure loss in the annulus is calculated by means of comparing the critical velocity with the actual velocity of the drilling fluid in the annulus.

If vannulus < vc the pressure loss is calculated for the frictional losses attributed to laminar flow as given in Equation 13;

$$\Delta P_{annulus\text{-}Laminar\ flow} = (\mu_p v_{annulus} L)/(1000(d_2 - d_1)^2) + (\tau_y L)/(200(d_2 - d_1)) \quad (13)$$

where L is the interval length.

If $v_{annulus} > v_c$ the pressure loss is calculated for the frictional losses attributed to turbulent flow as given in Equation 14;

$$\Delta P_{annulus\text{-}Turbulent\ flow} = [\rho^{0.75} v_{annulus}^{1.75} \mu_p^2 L] /[4901(d_2 - d_1)^{1.25}] \quad (14)$$

where $v_{annulus}$ is with a "ft/s" in terms of unit of measure.

In the scope of this study the drilling fluid behaviour is assumed to be Bingham Plastic. In order to calculate the frictional pressure losses in the annular sections of a wellbore the first equation to be solved is the annular velocity. The flow behavior parameters; plastic viscosity and yield point parameters are also required to be calculated using the rheometer readings. The successive step is the calculation of critical velocity. The critical velocity is going to be compared in reference to the annular velocity, and depending on either being greater or less, the flow regime type is going to dictate which frictional pressure loss equation to be used. Having a critical velocity greater than the annular velocity would mean that the flow regime is turbulent and therefore the respective annular frictional pressure loss equation given for turbulent regimes is required to be used. The same logic is valid for critical velocities less than the annular velocities in the case of which laminar flow pressure loss equations are to be used.

In this study the last two wellbore sections of the planned horizontal well namely 8 1/2" and 6" sections are studied for the frictional pressure loss calculations. In today's information technology machinery it is possible to conduct complex calculations very quickly. Even though quick calcu-

lations are easy to be performed, not all frictional pressure calculation studies take into account the tool joint (TJ) sections of the drill pipes in use. A generalized drillpipe drawing is given in Fig. 6. The drawing of a drillpipe depicts the tool joint sections at the top and bottom parts of a drillpipe. The tool joint segments of a drillpipe are larger in diameter. API Specification 7 [13] gives the details of tool joint dimensions for drill pipe grades. In a single drillpipe joint, a total of 17 inches is the sum of pin and box tong space sections. The length of the geometrically enlarged tool joint sections contributes to the generation of additional frictional pressure loss along the annulus.

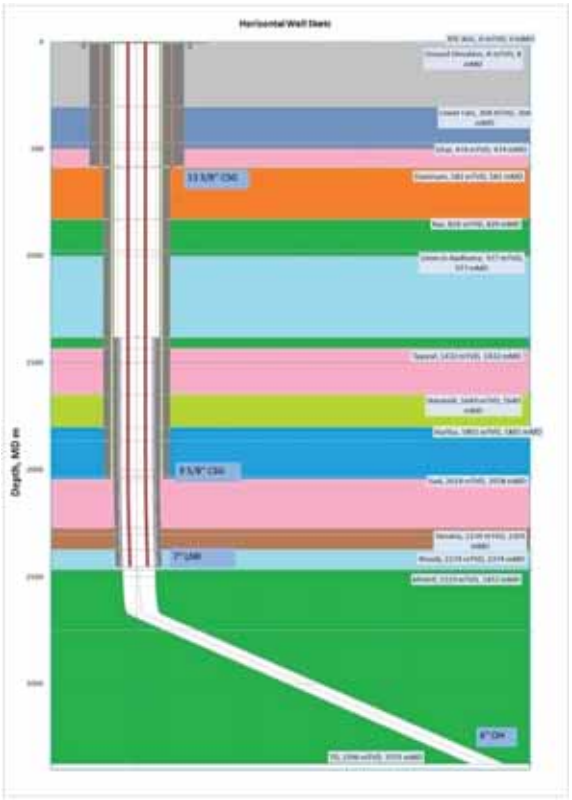

Figure 4. Planned horizontal well sketch.

While circulating in a wellbore which includes joints of drill pipes, the drilling fluid initially after having gone through the Bottom Hole Assembly; flows through the tool Joint of the pin end, then flows through the body section of the drillpipe, and flows through the tool joint of the box end for each and every drillpipe in the drillstring. For a geometry combination in an 8 1/2" wellbore, 5" nominal OD drillpipe, and 6 5/8" OD tool joint, the scaled drawing is as given in Fig. 7.

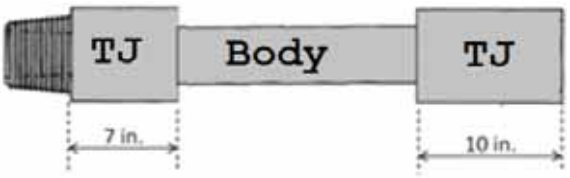

Figure 6. Schematics of a drillpipe joint.

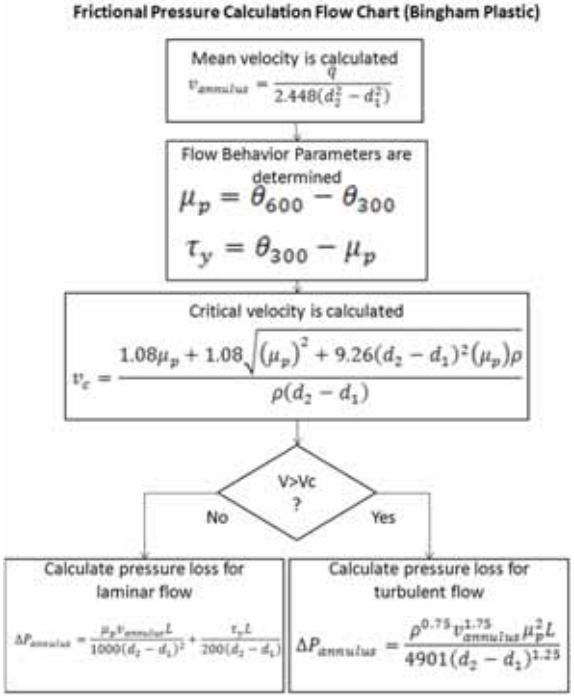

Figure 5. Frictional pressure calculation chart for annular flow by Adams and Charrier (1985).

The flow area gets restricted to the brown color shaded area, when the fluid element passes across the tool joints. Under normal circumstances the frictional pressure loss calculations mostly assumed that the flow area across the drillpipe elements is the area between the 5" nominal OD of the pipe and wellbore diameter itself. Fig. 8 depicts the ideal versus actual drillstring in a wellbore. The BHA (Bottom Hole Assembly) is composed of the following subsurface items: 8 1/2" PDC bit, 7" mud motor, float sub, 6 3/4" float sub, 8 1/8" Integral blade Stabilizer, 6 3/4" NMDC, 6 3/4" NM Hang-off sub. The rest of the workstring is composed of 5" HWDP and 5" DP to surface. The plain workstring drawing (given as the top drawing of Fig. 8) depicts

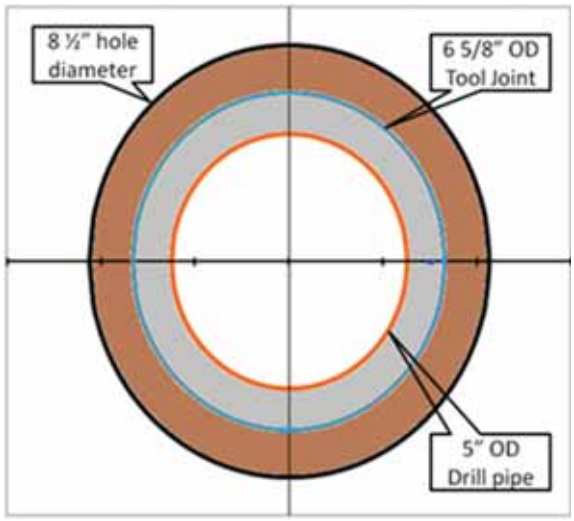

Figure 7. Scaled drawing of a tool joint section view in a wellbore.

the workstring with no tool joint upsets along the well bore. Whereas the workstring on which the tooljoint upsets are depicted (given as the lower drawing of Fig. 8) indicates the actual case of the string in the wellbore. The scaled drawing for a 3280 ft long drillstring clearly gives how the tool joints appear in a wellbore.

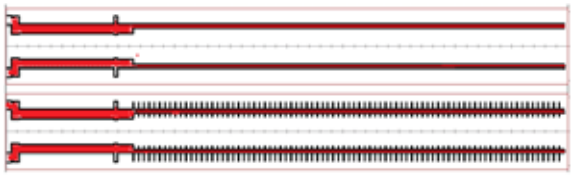

Figure 8. Ideal versus actual drill string in a wellbore.

Representation of the Calculated Frictional Pressure Losses

The frictional pressure loss and the respective Equivalent Circulating Density (ECD) are calculated for three different combinations of flow behaviors and flow rates. The flow rates taken into account are 340, 382.5, 425 and eventually 500 gpm (gal/min). The scaled drawing of the drillstring for which the calculations are made is as depicted in Fig. 9. The hydraulics analysis is conducted for the interval covering the previous (or otherwise the existing) casing shoe and targeted TD for the 8 1/2" wellbore section.

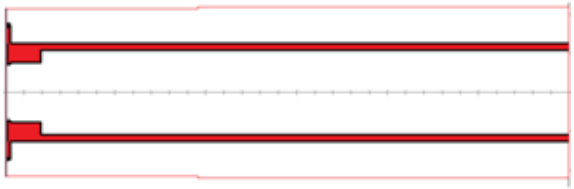

Figure 9. Scaled drawing of the 8 1/2" drillstring.

The first flow behavior group is PV=10 cp, and YP= 20 lbf/100ft^2. The results of the first flow analysis, which can be considered as mild from the rheological properties perspective is as presented in Fig. 10 and Fig. 11 respectively for annular pressure drop and ECD. It is observed that for each of the four different flow rates, the influence of the tool joints is observed to have increased the frictional pressure loss in the annulus. Consequently the ECD for the case of tool joints is showing elevated magnitudes. Assuming a depleted pore gradient of 7.51 ppg as indicated in the PPFG (Pore Pressure Fracture Gradient) of South of Iraq in the study presented by Eren et. al., (2013), it can be concluded that the loss of circulation is imminent.

The second group analysed is with the mild flow behaviors of a PV= 15 cp and YP= 25 lbf/100ft^2. Fig. 12 and Fig. 13 respectively present annular pressure drop and ECD. The results indicate that both the frictional pressure loss in the annulus and ECD magnitudes are further increased.

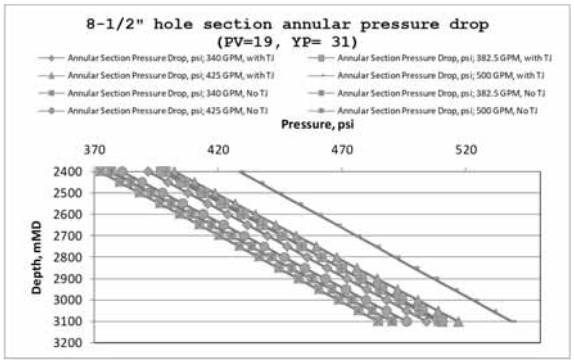

Figure 10. Annular pressure drop with PV=10 cp, and YP= 20 lbf/100ft^2.

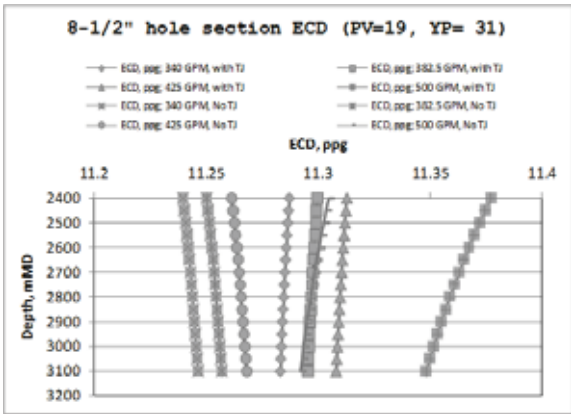

Figure 11. ECD with PV=10 cp, and YP= 20 lbf/100ft^2.

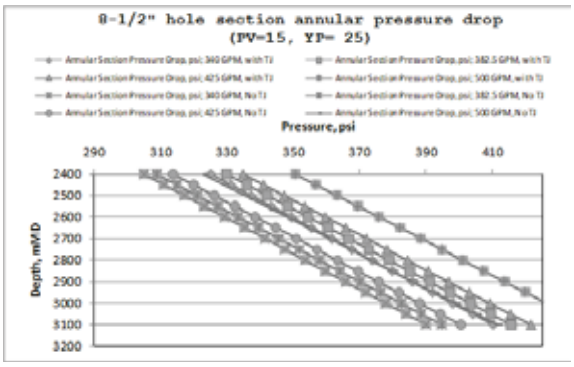

Figure 12. Annular pressure drop with PV=15 cp, and YP= 25 lbf/100ft^2.

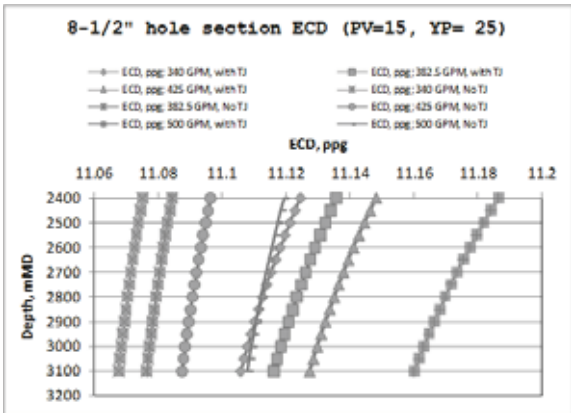

Figure 13. ECD with PV=15 cp, and YP= 25 lbf/100ft^2.

The third group analysed is with the high flow behaviors of a PV= 19 cp and YP= 31 lbf/100ft^2. Fig. 14 and Fig. 15 respectively present annular pressure drop and ECD. It is observed that the frictional pressure loss, and ECD magnitudes especially for a flow rate of 500 gpm can be extremely high approaching to Leak Off values (11.6 ppg), reported in the study of Eren et. al., (2007).

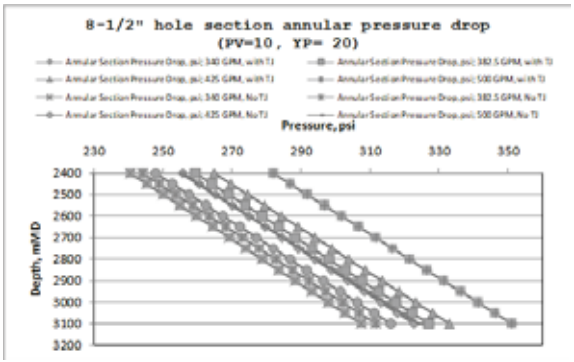

Figure 14. Annular pressure drop with PV=19 cp, and YP= 31 lbf/100ft^2.

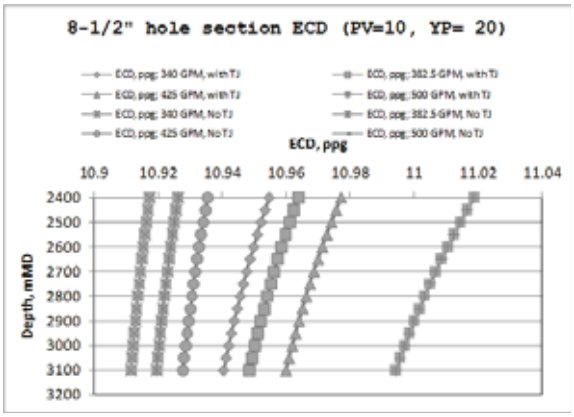

Figure 15. ECD with PV=19 cp, and YP= 31 lbf/100ft^2.

CONCLUSION

The planning of horizontal wells requires a very delicate study. In this research study the investigated aspects of horizontal well planning is presented. The geological prognosis of a well located in Iraq's Rumaila oil field is used for the planning of a horizontal well. Directional planning of the well is built on the formation details of the field. The selected build rates are based on practically applicable build rates for the similar oilfields.

The annular frictional pressure losses in the annulus are calculated using Non-Newtonian drilling fluid theoretical pressure loss equations. The tool joint sections of the drillpipes are also used as inputs in the calculations. The additional frictional pressure that is being generated is due to the restriction at each and every tool joint segment of a drillpipe. Calculation methodology is a novelty performed in the scope of this research study. It is can be observed that the ECD magnitudes being observed can be greater than the fracture gradients of the horizontal wells. The findings reveal that the annular frictional pressure losses, and ECD magnitudes especially for a flow rate of 500 gpm can be extremely high approaching to Leak Off values reported in the literature.

RECOMMENDATIONS

Here in this study the frictional pressure losses and ECD magnitudes are studied. What is recommended is to simulate a real case dataset and compare with the results. Effects of temperature as well as the effects of tool joints if incorporated are going to improve the accuracy of the hydraulics calculations. The contraction and expansion of the flow across the tool joint sections can also be incorporated for a further accurate study.

NOMENCLATURE

B = Build-Up Rate, deg/100 ft
d_1 = casing or open hole diameter, inches
d_2 = outer diameter of the drillstring member, inches
D_1, D_2, D_3 = Displacements of respective wellbore sections 1,2 and 3, ft
H_1, H_2, H_3 = Vertical lengths of respective wellbore sections 1,2 and 3, ft
L_{hole} = Length of hole, ft
L = pipe length, ft
q = flow rate, gpm
R = Build-Up Radius, ft
V = Vertical Height, ft
$v_{critical}$ = critical velocity, ft/s
$v_{annulus}$ = velocity of drilling fluid in annulus, ft/s
$\Delta P_{annulus}$ = pressure loss, psi
μ_p = (PV) plastic viscosity, cp
ρ = drilling fluid density, ppg
τ_y = (YP) yield point, blf/100ft^2
β_1 = Initial Inclination, deg
β_2 = Final Inclination, deg

References

1. Aguilera. R., Cordell. G.M., Nicholl. G.W. Contributions in Petroleum Geology and Engineering Volume 9: Horizontal Wells, Gulf Publishing Company, Calgary, Alberta, 1991.
2. API Recommended Practice 13D. Recommended Practice on Rheology and Hydraulics of Oil–well Fluids, 6th edition, Washington, 2010.
3. Azar, J.J. and Samuel, G.R. Drilling Engineering, PennWell Books, Tulsa, OK, 2007.
4. Viloria O.M. Analysis of drilling fluid rheology and tool joint effect to reduce errors in hydraulics calculations. PhD diss., Texas A&M University, 2006.
5. Enfis, M.S., Ahmed, R.M. and Saasen, A. The hydraulic effect of tool–joint on annular pressure loss. Paper presented at the SPE Production and Operations Symposium, Oklahoma City, Oklahoma, USA, 27–29 March. Society of Petroleum Engineers, Richardson, TX, pp. 1–11, 2011.
6. Simoes, S. Q., Miska, S. Z., Takach, N. E., & Yu, M. The Effect of Tool Joints on ECD While Drilling. Paper presented at the Production and Operations Symposium, Oklahoma City, Oklahoma, USA, 31 March–3 April. Society of Petroleum Engineers, Richardson, TX, pp. 1–8, 2007.
7. Jeong, Y.T., & Shah, S. N. Analysis of Tool Joint Effects for Accurate Friction Pressure Loss Calculations. Paper presented at the IADC/SPE Drilling Conference, Dallas, Texas, USA, 2–4 March. Society of Petroleum Engineers, Richardson, TX, pp. 1–8, 2004.
8. Al–Ameri, T.K., Jafar M.S.A., Pitman J. Hydrocarbon Generation Modeling of the Basrah Oil Fields, Southern Iraq. http://www.searchanddiscovery.com/documents /2011/20116alameri/ndx_alameri.pdf. Search and Discovery Article No 20116. Retrieved on 2016–03–30. 2011.
9. Arshad, U., Jain, B., Ramzan, M., Alward, W., Diaz, L., Hasan, I., Ali, A., Riji, C. Engineered Solution to Reduce the Impact of Lost Circulation During Drilling and Cementing in Rumaila Field, Iraq. Presented at the International Petroleum Technology Conference, Qatar, 6–9 December. Society of Petroleum Engineers, Richardson, TX, pp. 1–17, 2015.
10. Devereux, S. Practical well planning and drilling manual. PennWell Books, Tulsa, OK, 1998.
11. Adams, N. and Charrier, T. Drilling engineering: a complete well planning approach. Pennwell Corp., Tulsa, OK, 1985.
12. Eren T., Ozkale A., Ozer C., Kirbiyik S. A Case Study: Comparison of the Theoretical and Actual Drilling Hydraulic Pressures for Wells in Turkey. Presented at the 17th International Petroleum and Natural Gas Congress and Exhibition, Ankara, Turkey, 29 May, pp. 1–6, 2007.
13. API Specification 7. Specification for Rotary Dril Stem Elements, 40th edition, Washington, 2002.